Chapter 4

3–1 Spheroid Surface Pressure Measurements

4.1 Introduction

Chapters 4 and 5 present surface pressure measurements on the 3–1 spheroid and the 4.2–2–1 ellipsoid respectively. Measurements for the 3–1 spheroid were performed for incidences between $-0.2°$ and $-10.2°$ with increments of $2°$. Only the results for the spheroid at $-0.2°$, $-6.2°$, and $-10.2°$ are presented in detail. Measurements on the ellipsoid were limited to incidences of $-0.2°$, $-6.2°$, and $-10.2°$. These measurements were repeated with approximately 0.5×10^6 increments for Re_l between 0.6×10^6 and 4.0×10^6. The high density of water allows measurements of high precision to be performed. Examining groupings of curves with different Reynolds numbers but at the same incidence and azimuth allow variations due to the change in Reynolds number to be identified. The pressure measurements presented by Meier and Kreplin [55] and Ahn [26] were for a single Reynolds number, so identification of changes with Reynolds number was not possible.

4.2 Experimental Setup

The spheroid has twenty one tappings of $1.1\,mm$ diameter in a row running from front to rear of the model. The model may be manually rotated about its longitudinal axis in $15°$ increments between $-180°$ and $180°$, thus altering the azimuthal position (φ) of the surface pressure measurements. The model is truncated at the base where the sting enters the model ($x_{bc} = 161\,mm$; the subscript bc denotes body coordinates). An additional measurement of

the pressure inside the model is taken to determine the base pressure. The base pressure is a measure of the average pressure at the annular tap formed by the gap between the model and sting. The axial locations of the tappings are listed in Table 4.1. All the tappings from the model, plus three additional tappings from the tunnel, were connected to ports on a Scanivalve.

The Scanivalve switched each of the tappings to a Validyne DP15 differential pressure transducer, where, after a delay to allow the reading to settle, the pressure at each port was measured. A sample time of ten seconds and sample rate of 256 Hz was used. The Validyne DP15 was fitted with a "-42" diaphragm that provides a range of $\pm 140\,kPa$. The signal conditioner that controls the Validyne DP15 transducer allows the range to be selected to optimise the full scale output of the transducer. One tapping in the test section supplies the reference pressure for the differential pressure transducer and two other tappings allow the pressure differential across the tunnel contraction to be measured. The tap for the reference pressure is located on the floor of the test section $300\,mm$ in the streamwise direction from the test section entrance.

The reference pressure is applied to the negative input of the differential pressure transducer and the output of the Scanivalve to the positive input of the transducer. The Scanivalve steps through 25 ports for each set of readings. The pressure measured at each port, $P_i - P_{ref}$, is given by

$$P_i - P_{ref} = k_{Validyne} \times V_{P_i - P_{ref}} \tag{4.1}$$

where $V_{P_i - P_{ref}}$ is the output of the transducer when the Scanivalve is connected to Port i and $k_{Validyne}$ is the calibration constant for the Validyne transducer. Port #0 of the Scanivalve is connected to the reference pressure so the first measurement of each data set provides a new zero for the Validyne transducer, as both sides of the transducer are subject to the same pressure. Thus the zero corrected pressure, P_{i_ref} is given by

$$P_{i\_ref} = k_{Validyne} \times \left(V_{P_i - P_{ref}} - V_{P_0 - P_{ref}}\right) \tag{4.2}$$

Two Rosemount Model 3051C differential pressure transducers (one low range and one high range) monitor the pressure difference between the tappings upstream and downstream of the contraction. This set of transducers is sampled at the same time and sample rate as the Validyne transducer to allow temporal corrections to be performed on each measurement from the Validyne transducer. The temporal corrections allow for minor fluctuations in the tunnel velocity and thus the test section dynamic pressure. The test section dynamic pressure determined from the Rosemount transducers when the Scanivalve is on Port i, $P_{i_{dynamic}}$, is given by

$$P_{i_{dynamic}} = k_{cont} \times k_{Rose} \left(V_{P_{i_{Rose}}} - V_{P_{Rose\_zero}}\right) \tag{4.3}$$

Port No.	Tap No.	$x_{bc}\,(mm)$	x_{bc}/l	Note
0				Reference tap
1				Post-Contraction tap
2				Pre-Contraction tap
3	1	−165.0	−0.500	Nose tap
4	2	−155.0	−0.470	
5	3	−145.0	−0.439	
6	4	−135.0	−0.409	
7	5	−125.0	−0.379	
8	6	−115.0	−0.348	
9	7	−95.0	−0.288	
10	8	−75.0	−0.227	
11	9	−55.0	−0.167	
12	10	−35.0	−0.106	
13	11	−15.0	−0.045	
14	12	15.0	0.045	
15	13	35.0	0.106	
16	14	55.0	0.167	
17	15	75.0	0.227	
18	16	95.0	0.288	
19	17	115.0	0.348	
20	18	125.0	0.379	
21	19	135.0	0.409	
22	20	145.0	0.439	
23	21	155.0	0.470	
24	22	161.0	0.488	Base tap

Table 4.1: Axial location of surface pressure tappings and Scanivalve connection scheme.

where $V_{P_{i_{Rose}}}$ is the output of the Rosemount transducer when the Scanivalve is connected to Port No. i; $V_{P_{Rose\_zero}}$ is the zero for the Rosemount transducer obtained before the start of each run when the water in the tunnel is stationary; k_{Rose} is the calibration constant for the Rosemount transducer; and k_{cont} is a function weakly dependent on Reynolds number that relates the pressure difference between the tapping upstream and downstream of the contraction to the test section dynamic pressure. The temporal and zero corrected pressure measurement from the Validyne transducer is

$$P_{i\_ref\_corrected} = P_{i\_ref} \times \frac{P_{0_{dynamic}}}{P_{i_{dynamic}}}. \tag{4.4}$$

The use of $P_{0_{dynamic}}$ in the above equation results in Eq. 4.4 being corrected to the dynamic pressure when Port #0 was being measured. Any other Port could have been selected, as this value cancels out when the non-dimensional pressure is calculated. Two points to note are:

- The Port the Scanivalve is on has no influence on the output of the Rosemount transducer, the subscript i simply indicates that this measurement was taken at the same time that the Validyne transducer was measuring $P_i - P_{ref}$, and is thus the applicable measurement for applying the temporal correction.
- Port #1 and Port #2 of the Scanivalve are connected to the tappings after and before the tunnel contraction respectively. The pressure difference across the contraction, and thus the test section dynamic pressure, may also be calculated from the Validyne transducer using $P_{2\_ref\_corrected} - P_{1\_ref\_corrected}$.

The corrected pressure from the Validyne transducer may be reduced to a dimensionless pressure coefficient C_{P_i} by dividing through by the test section dynamic pressure determined from the measurements at Port #1 and Port #2:

$$C_{P_i} = \frac{P_{i\_ref\_corrected}}{k_{cont}\left(P_{2\_ref\_corrected} - P_{1\_ref\_corrected}\right)} \tag{4.5}$$

Substituting Eq. 4.4, Eq. 4.3 and Eq. 4.2 into Eq. 4.5 gives

$$C_{P_i} = \frac{C_{V_{i\_ref}}}{k_{cont}\left(C_{V_{2\_ref}} - C_{V_{1\_ref}}\right)} \tag{4.6}$$

where

$$C_{V_{i\_ref}} = \frac{V_{P_i - P_{ref}} - V_{P_0 - P_{ref}}}{V_{P_{i_{Rose}}} - V_{P_{Rose\_zero}}} \tag{4.7}$$

$C_{V_{i\_ref}}$ is a dimensionless pressure coefficient that has been zero corrected for drift in the Validyne pressure transducer and temporally corrected for fluctuations in the test section dynamic

pressure. Eqs. 4.6 and 4.7 allow the non-dimensional pressure to be calculated without using calibration factors for the differential pressure transducers.

The elimination of these calibration constants should improve the accuracy of the measurements. This does not eliminate measurement errors due to non-linearity, hysteresis and repeatability of these pressure transducers. Errors due to non-linearity will be smaller for measurements at lower Reynolds numbers where the measured pressure differential is a smaller proportion of the full range. The only calibration factor required is for the tunnel contraction: k_{cont} is the calibration factor that allows the dimensional value of the test section dynamic pressure to be determined from the pressure differential between the taps at the start and end of the contraction. k_{cont} was determined by prior calibration using a pitot-static tube in the test section connected to the Validyne transducer via the Scanivalve, and evaluated from

$$\begin{aligned} k_{cont} &= \frac{P_{4\_ref\_corrected} - P_{3\_ref\_corrected}}{P_{2\_ref\_corrected} - P_{1\_ref\_corrected}} \\ &= \frac{C_{V_{4\_ref}} - C_{V_{3\_ref}}}{C_{V_{2\_ref}} - C_{V_{1\_ref}}} \end{aligned} \tag{4.8}$$

when Port #4 and Port #3 of the Scanivalve are connected to the central and static taps of the pitot-static tube respectively. The contraction factor varies slowly with Reynolds number, from 1.006 to 1.016 between the minimum and maximum Reynolds number respectively. The slight bias of C_p value at the nose tap above unity seen in Fig. 4.1 is believed to be due to inaccuracy in the measurement of this value.

The trip strip, when used, was placed at 20% of the model's axial length and was designed to trip the boundary layer for $Re_l \geqslant 1.3 \times 10^6$. The trip strip is detailed in Subsection 4.4.4.

4.3 Uncertainty Estimates for Surface Pressure Measurements

The main source of uncertainty is the sensitive nature of the flow at transitional Reynolds numbers to imperceptible changes on the surface. The model was polished after each change of azimuth to minimize any effect of surface contamination due to handling. On occasion the polishing and measurement were repeated when transition occurred earlier than expected. A more formal calculation of the inaccuracy of Eq. 4.6 is presented in Appendix B: however, the following discussion is believed to provide a superior account of the uncertainties in the calculation of C_p.

Ideally the pressure measured at the nose tap and the base tap should be consistent for all

azimuth angles, as the position of these taps is invariant when the body is rotated about its major axis. An estimate of the accuracy of the surface pressure measurements can be obtained by examining the results for the nose tap when the model was at $-0.2°$ incidence, when the expected C_p should be equal to unity (for all practical purposes, classical potential solution calculates at $x_{bc}/l = -0.5$ a C_p of 0.99996). Fig 4.1 shows that variation in C_p is less than 0.02 for $Re_l = 0.6 \times 10^6$, less than 0.01 for $Re_l = 1.0 \times 10^6$, and less than 0.005 for the larger Reynolds numbers.

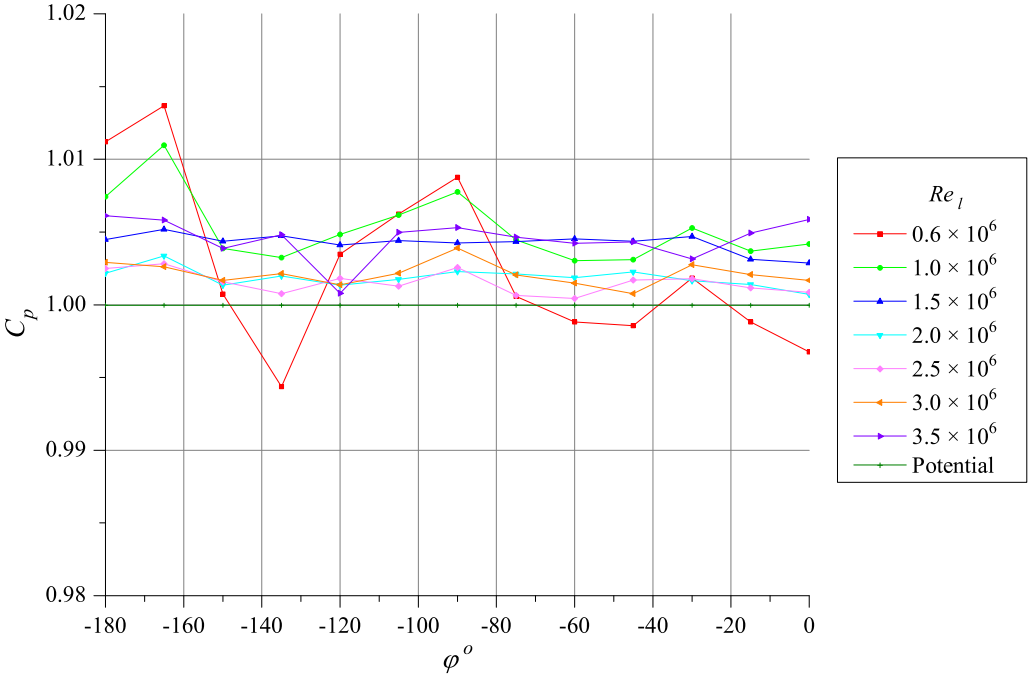

Figure 4.1: Comparison of nose pressure measurements at different body azimuths for $\alpha = -0.2°$ and a range of Reynolds numbers. Ideally the pressure at the nose tap is invariant with change in azimuth angle and Reynolds number (except at exceedingly small Re_l) and for all practical purposes equals unity at this angle of incidence.

A comparison between the base pressure measured for the spheroid with untripped and tripped flow is provided in Fig. 4.2. The greater variation in base pressure for the model when it is subject to unforced transition displays the sensitivity of the boundary layer, and consequently the base pressure, to the minor inconsistency caused by rotating the body. When boundary layer transition is forced by the trip strip for $Re_l \geqslant 1.5 \times 10^6$ the variation in base pressure coefficient is less than 0.01.

The relatively high density of water, with the resulting large pressure differentials, allow for precise measurement of the time-averaged surface pressure coefficient, $\bar{C}_{P_i}$, providing an appropriate sample time and rate are used. The slow variation of k_{cont} with Reynolds number results in a negligible contribution to the imprecision of the measurements. The precision of

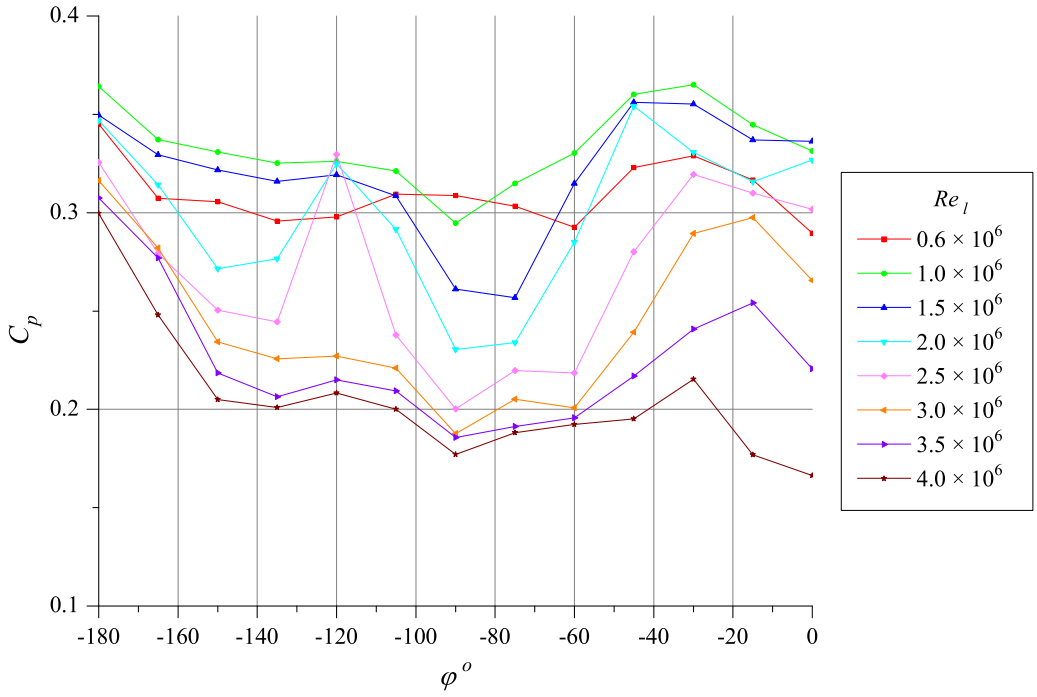

(a) Untripped transition

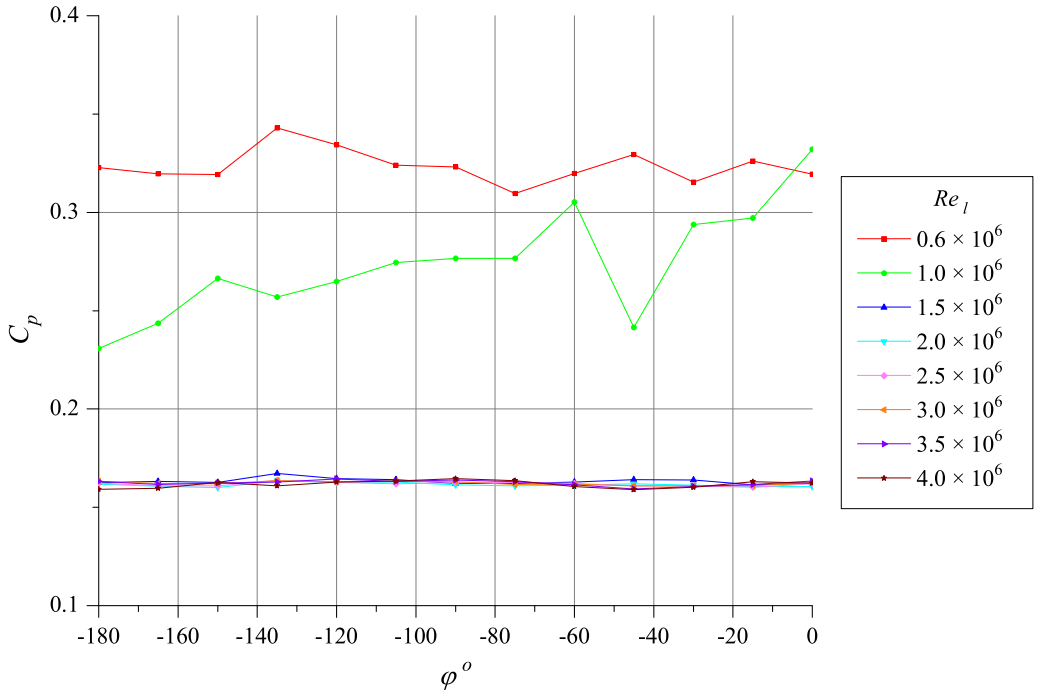

(b) Tripped at $x_{bc}/l = -0.3$ for $Re_l \geqslant 1.5 \times 10^6$

Figure 4.2: Comparison of base pressure with untripped and tripped boundary layers at $\alpha = -10.2°$ measured at the annular tap formed by the gap between the model and sting. This figure highlights the sensitivity of the base pressure to the location of boundary layer transition.

the mean (standard error) may be estimated using

$$\sigma_{\bar{C}_{P_i}} = \frac{\sigma_{C_{P_i}}}{\sqrt{N}} \tag{4.9}$$

where N is the number of samples and the standard deviation of C_{P_i}, $\sigma_{C_{P_i}}$, is determined using the error propagation equation [56]. Appendix B includes the calculation for $\sigma_{\bar{C}_{P_i}}$. In the other sections of this text (except Appendix B) the measured time averaged surface pressure coefficient, $\bar{C}_{P_i}$, is simply referred to as C_p, as is the surface pressure calculated from numerical methods.

The high precision that has been achieved in these measurements is of great importance when examining the influence of Reynolds number on the surface pressure distribution. High precision allows small variations in the pressure to be interpreted as having significance regarding flow over the model and not resulting from a random deviation. The standard deviation of the measurements may be calculated using Eq. 4.9 and the error bars representing $3\sigma_{\bar{C}_{P_i}}$ are indicated on the pressure distributions presented in staggered format in Fig. 4.3.

The ability of these pressure measurements to identify variations in the boundary layer is demonstrated by comparison of pressure distributions on the spheroid with untripped and tripped transition in Fig. 4.4. With a tripped boundary layer ($Re_l \geqslant 1.5 \times 10^6$) the measured C_p distributions are almost identical; with unforced transition the C_p distribution behaves differently with each Reynolds number in this range.

4.4 Spheroid Surface Pressure Results

Measurements of surface pressure on the spheroid were taken between Re_l of 0.6×10^6 and 4.0×10^6 when water temperatures allowed. When water temperatures were below $20°C$ the maximum Re_l selected was 3.5×10^6; when water temperatures were above $25°C$ the minimum Re_l was increased to 0.65×10^6. In general measurements were limited to $-180° \leqslant \varphi \leqslant 0°$, as the model has symmetry through the plane $y_{bc} = 0$. During the initial setup of the model one set of readings were taken for $\varphi = -90°$, $0°$, $-90°$ and $-180°$ to confirm that the body was correctly aligned. The results are displayed in Fig. 4.5.

On many of the plots the surface pressure calculated using classical potential theory for a spheroid of the same dimensions as the experimental model are included. These calculations do not allow for viscous effects, circulation, the presence of the sting and support foil or blockage, but provide a useful reference for discussion of the results. As the body's angle of incidence increases and the lift and drag of the body increase, the estimated surface pressure from potential theory will become less accurate. The potential calculations are detailed in Appendix A.

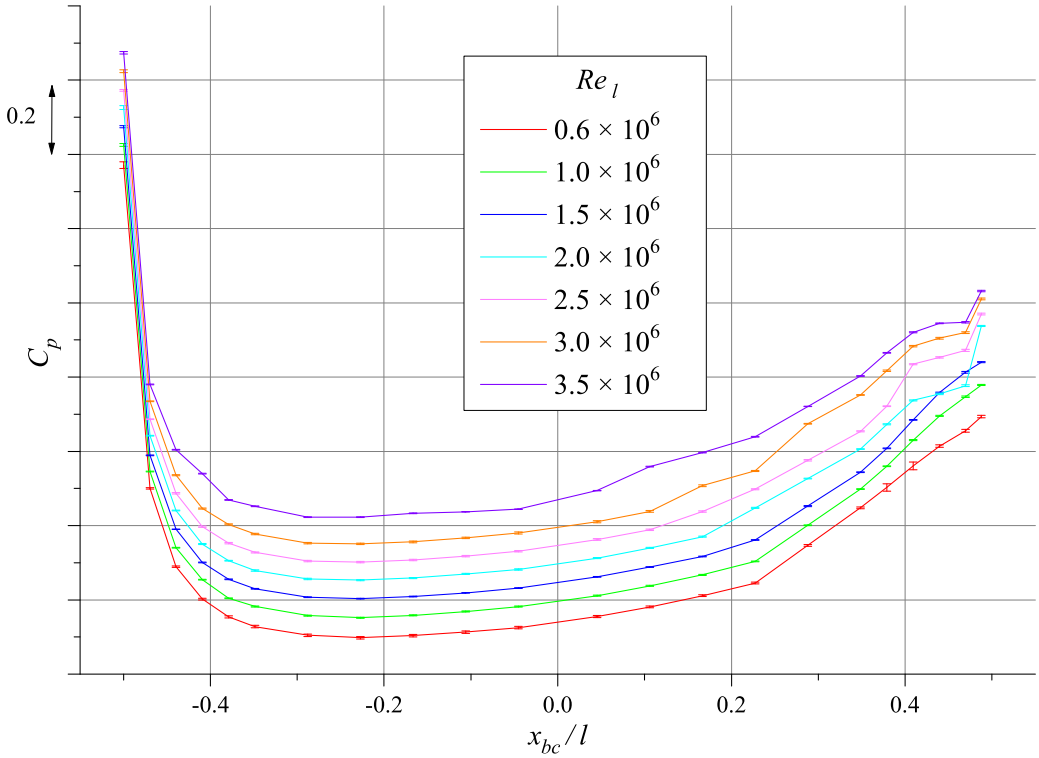

Figure 4.3: Surface pressure measurements for the spheroid, $\alpha = -6.2°$, with $3\sigma_{\bar{C}_{P_i}}$ error bars demonstrating the precision of the measurements. High precision allows small variations in the pressure distribution to be interpreted as having significance allowing salient features of the pressure distribution and their variation with Reynolds number to be observed.

The graphs of C_p vs x_{bc}/l for φ at 15° intervals are presented in Appendix C for $\alpha = -0.2°$, $-6.2°$ and -10.2°. Measurements were also taken at $\alpha = -2.2°$, $-4.2°$ and -8.2°.

4.4.1 Spheroid at $\alpha = -0.2°$

The pressure distributions for the 3–1 spheroid at $\alpha = -0.2°$ show similar structure for all measured azimuths, as would be expected given the low angle of incidence. The potential calculations suggest that the C_p values at the middle of the body, $x_{bc} = 0$, for $\varphi = 0°$ and $\varphi = -180°$ should be the same. From Fig. 4.6 it is apparent that there is a small decrease in C_p as φ decreases from 0° to $-180°$. The suspected cause of this is the support foil. The leading edge of the support foil is placed 120.5 mm behind the truncated end of the spheroid when the spheroid is at $\alpha = -0.2°$. The presence of this foil will cause a non-axisymmetric blockage. The curves for the surface pressure calculated using potential theory at $\varphi = 0°$ and $\varphi = -180°$ (Fig. 4.6) supply evidence that the minor incidence is not the major source of difference in surface pressure at these azimuth angles. The surface pressure distributions at a number of azimuth

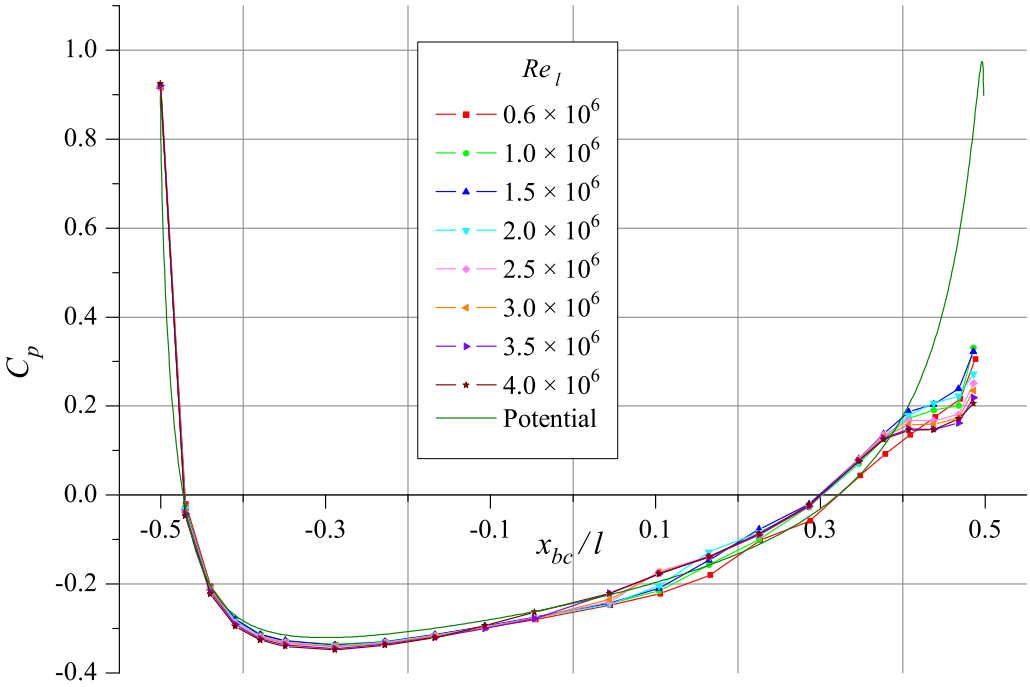

(a) Untripped

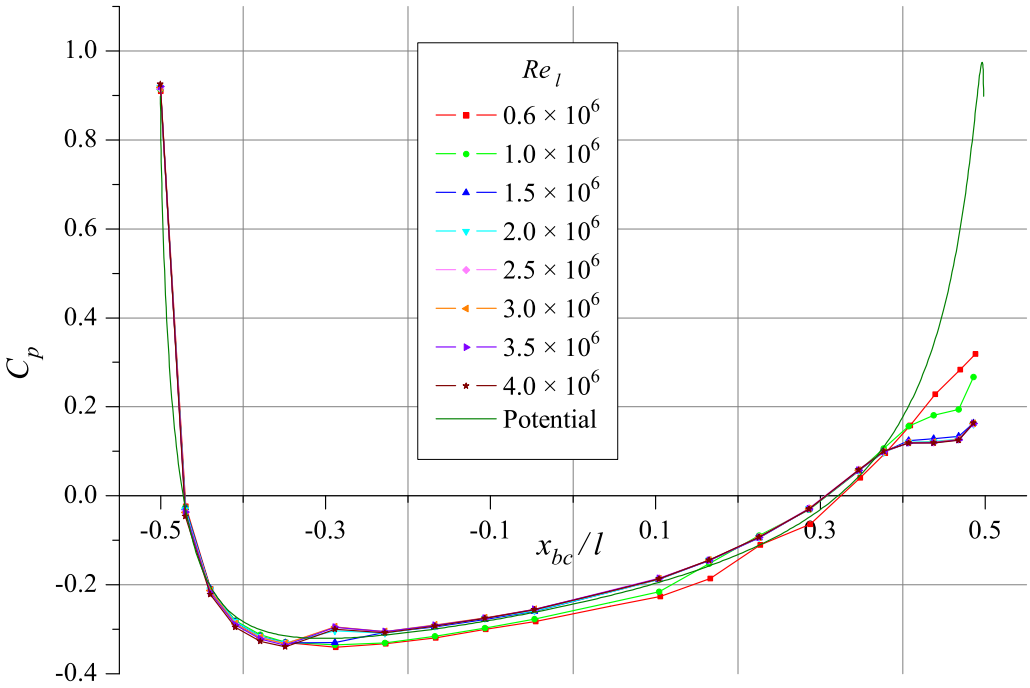

(b) Tripped at $x_{bc}/l = -0.3$

Figure 4.4: Comparison of surface pressure distributions for the tripped and untripped 3–1 spheroid, $\alpha = -10.2°$, $\varphi = -150°$. The surface pressure distributions and their variation with Reynolds number may be used to identify boundary layer transition and separation.

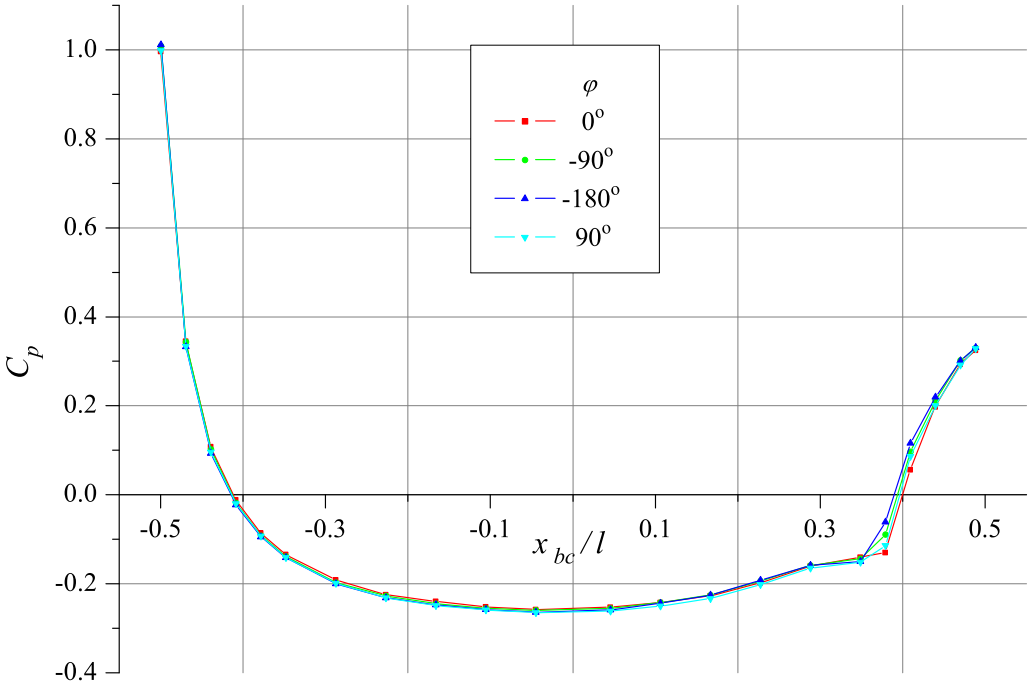

(a) $Re_l = 0.5 \times 10^6$

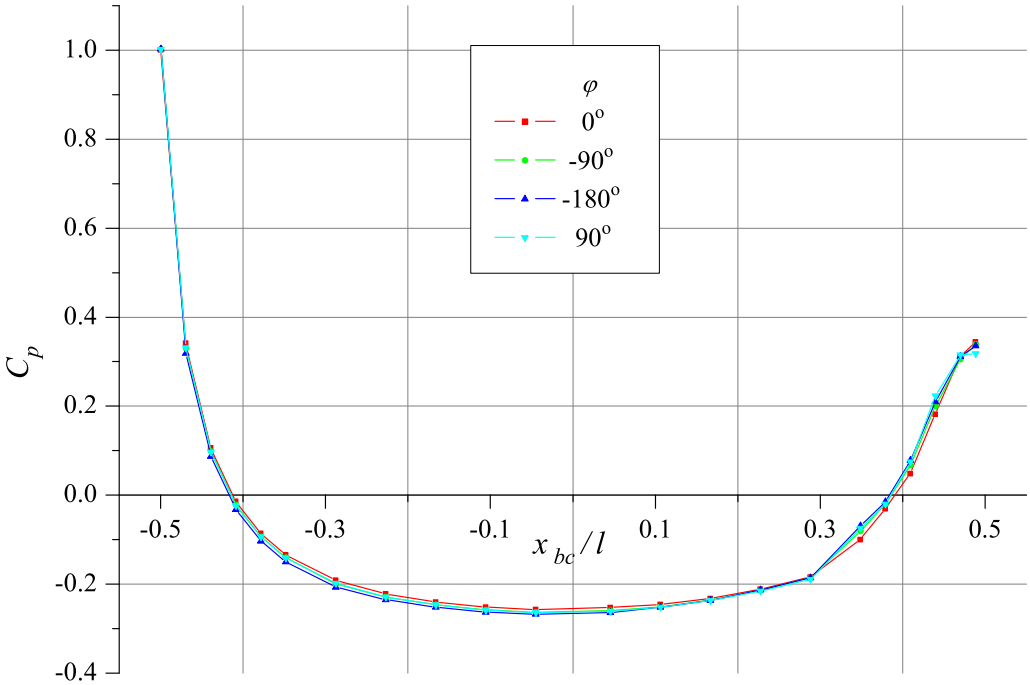

(b) $Re_l = 2.0 \times 10^6$

Figure 4.5: Comparison of surface pressure of spheroid used to confirm alignment at $\alpha = -0.2°$. The difference between φ at 0° and −180° is believed to be primarily due to blockage caused by the support foil. The results at $\varphi = \pm 90°$ show the alignment and repeatability of the measurements.

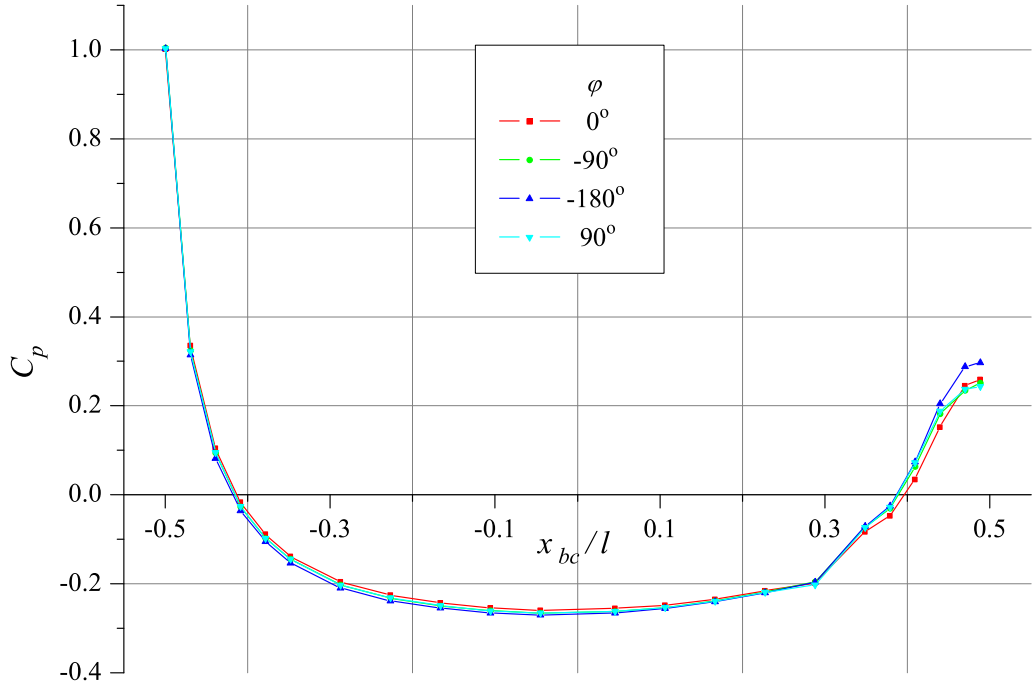

(c) $Re_l = 3.0 \times 10^6$

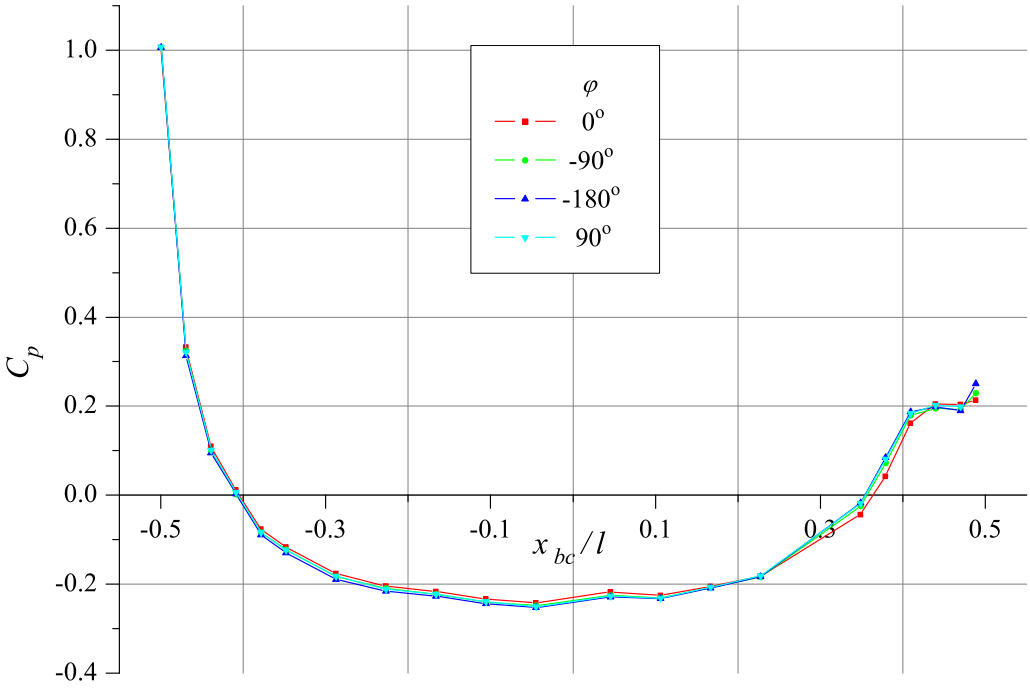

(d) $Re_l = 3.5 \times 10^6$

Figure 4.5: Comparison of surface pressure of spheroid used to confirm alignment at $\alpha = -0.2°$. The difference between φ at 0° and −180° is believed to be primarily due to blockage caused by the support foil. The results at $\varphi = \pm 90°$ show the alignment and repeatability of the measurements (cont.)

angles for $Re_l = 2.0 \times 10^6$ is shown in Fig. 4.6 and for a range of Reynolds numbers at $\varphi = -45°$ in Fig. 4.7.

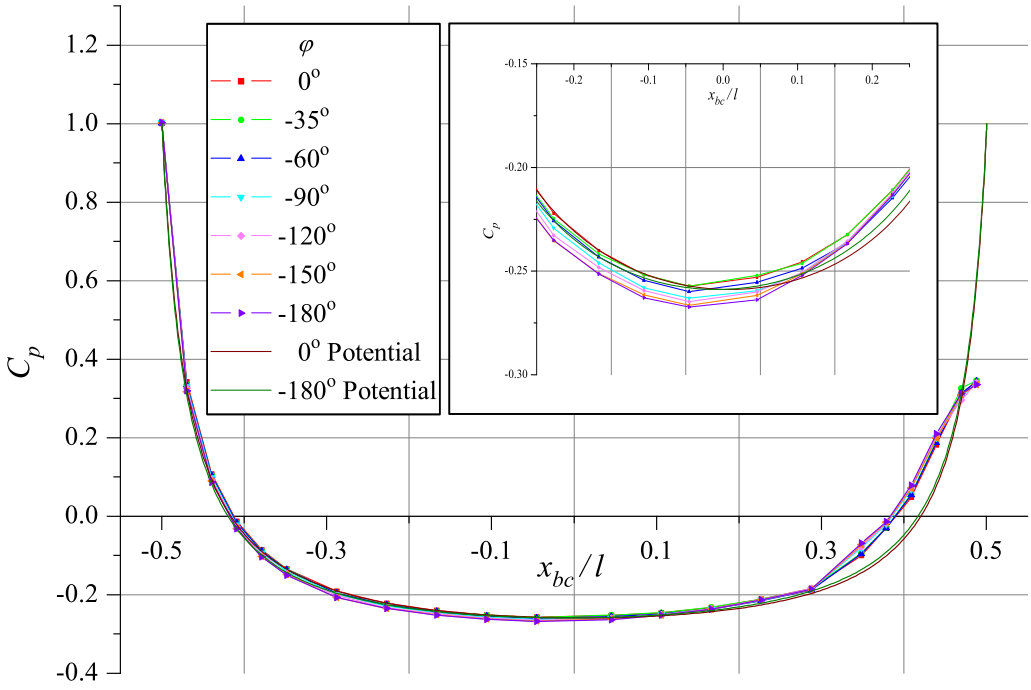

Figure 4.6: Comparison of surface pressure measurements for Re_l 2.0×10^6, $\alpha = -0.2°$. The trend for decreasing minimum pressure as φ decreases from 0° to −180° is believed to be predominantly due to the blockage caused by the support foil.

Reynolds Numbers 0.6×10^6 **to** 3.0×10^6

Over the front half of the body the measured surface pressure closely matches the surface pressure predicted by the potential calculations, with the values measured at lower Reynolds numbers being slightly smaller than the values measured at higher Reynolds numbers. Over the rear half of the body the surface pressure measured at the lowest Reynolds numbers increases compared to the potential curve soon after the middle of the body and a laminar separation bubble occurs around $x_{bc}/l = 0.34$. As Re_l increases towards 3.0×10^6 the measured surface pressure stays closer to the calculated potential curve. It is reasonable to suggest that the deviation from the potential curve is due to boundary layer growth, the thicker boundary layer at lower Reynolds numbers being associated with the greater deviation from the potential curve. The laminar separation bubble reduces in size as Reynolds number increases and is no longer discernible for $Re_l > 1.5 \times 10^6$. The surface pressure values for the rear-most tap and the base pressure are clustered together for $Re_l \leqslant 2.5 \times 10^6$, the corresponding results at 3.0×10^6 sit between the values for the lower Reynolds numbers and the results for 3.5×10^6. The curves

for all Reynolds numbers flatten out when the flow separates as it approaches the sting.

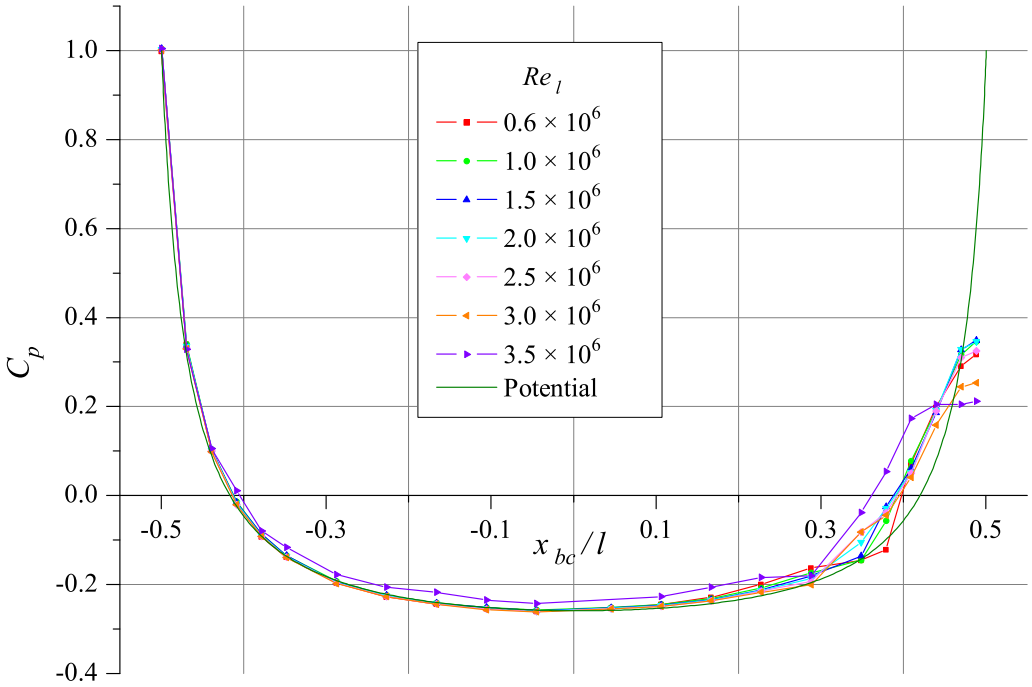

Figure 4.7: Comparison of surface pressure measurements, $\alpha = -0.2°$, $\varphi = -45°$. A laminar separation bubble is apparent for $Re_l \leqslant 1.5 \times 10^6$. For $Re_l = 3.5 \times 10^6$ boundary layer transition has occurred near the nose resulting in a thicker boundary layer with earlier turbulent boundary layer separation and a reduced base pressure. The early transition for the largest Reynolds number is believed to be due to the disturbance caused by a tapping.

Reynolds Numbers 3.5×10^6

The surface pressure coefficient shifts from values for lower Reynolds numbers at a position early on the body ($x_{bc}/l = -0.4$) and sits approximately 0.025 above those results until around $x_{bc}/l = 0.3$ where the pressure increases rapidly, noticeable before the increase in pressure at the lower Reynolds numbers Fig. 4.7. The surface pressure continues to rise rapidly until around $x_{bc}/l = 0.4$ and then flattens out, indicating a separation of the turbulent boundary layer. The separation at this Reynolds number occurs upstream of those at lower Reynolds number for this incidence. Examination of the surface oil flow photographs confirms an overall shift upstream in the separation line at this Reynolds number (Figs. 7.14 and 7.15). This earlier separation may be explained by the significant increase in the streamwise length of turbulent boundary layer leading to a corresponding increase in boundary layer thickness. The thicker boundary layer transfers less energy to the flow near the surface and thus leads to an earlier separation. Flow visualisation at the higher Reynolds numbers (Fig. 7.15) shows some vortical structures

existing in the separated region, but these structures do not create any observable disturbance in the measured surface pressure coefficient. This may be explained by the low energy of flow in the separation zone relative to the freestream.

When the boundary layer undergoes transition from a laminar to turbulent state a discontinuity in the surface pressure curve is expected, as the local perturbation in displacement thickness produces corresponding changes in the local freestream curvature. The overall increase in measured surface pressure seen in these measurements at the front of the model is believed to be associated with the transition of the boundary layer state from laminar to turbulent. Further evidence of this will be provided in Subsection 4.4.2.

Meier and Kreplin's [55] surface pressure measurements on a 6–1 spheroid at $Re_l = 7.2 \times 10^6$ display a similar feature for $\alpha = 0°$ and 5°. For $\alpha = 0°$ the increase in pressure occurs near $x_{bc}/l = -0.4$. In a later study, using a similar model fitted with surface hot film sensors, at $\alpha = 0°$ Kreplin et. al. [17] observed transition to occur close to the centre of the bodies under similar conditions. This discrepancy between the location of the shift in surface pressure and the later measured position of transition determined using hot films may well be explained by the disturbance caused by the tapping holes [57]. The possible disturbance caused by the tappings must also be considered in these measurements.

As the water had warmed up during testing, the opportunity to perform an additional reading for $\varphi = 180°$ at $Re_l = 3.8 \times 10^6$ was taken. The results for this condition lay on top of the values taken at $Re_l = 3.5 \times 10^6$.

4.4.2 Spheroid at $\alpha = -6.2°$

The maximum Re_l obtained during the testing at this angle was 3.5×10^6. This value was not great enough to cause the transition to move to the front of the body for $0° \geqslant \varphi \geqslant -150°$ as was seen for $\alpha = -0.2°$. A considerable variation in the length of unfavourable pressure gradient occurs over this range of φ. The results discussed in this Subsection are displayed in Fig. 4.8 (and also Fig. 4.9, $\alpha = -4.2°$ and $-10.2°$).

Reynolds Numbers 0.6×10^6 to 3.0×10^6

The measured surface pressure curves on the front half of the spheroid lie close to each other. In some regions a spread in the surface pressure values was observed, with the surface pressure for the lower Reynolds numbers a fraction larger than those at higher Reynolds numbers. This observation is apparent in Fig. 4.8(a) and further discussed in Subsection 4.4.3, as it is better defined at a higher angle of incidence.

An exception to the previous observation occurs on the suction side of the model. For $\varphi \leqslant -135°$ the curve for the lowest Re_l sits below, rather than above, that of the other curves on the back half of the model; this is carried forward to the front of the model where it can be seen to cut across other curves between $x_{bc}/l = -0.4$ and -0.1 as shown in Fig. 4.8(b). (This effect becomes more obvious as $\varphi \to -180°$.) A similar occurrence is seen in the results for $\alpha = -4.2°$, $-8.2°$ and $-10.2°$. At $\alpha = -10.2°$ it is apparent only for $\varphi \leqslant -165°$. This variation at the lowest Reynolds number coincides with a large separation bubble on the pressure side as shown in Fig. 4.8(c) and (d).

The measured curves are still close to the curve calculated using classical potential theory on the front half of the body. As adverse pressure gradients begin near the rear half of the body the departure from the grouped curves appears to take one of two forms:

- The surface pressure measurements for the lower Reynolds numbers increase in value compared to the other curves as the thickness of the laminar boundary layer increases. This departure from the other curves is gradual and is apparent over a number of streamwise points. At the lowest Reynolds number these curves often display a laminar separation bubble towards the end of the body. The gradual increase in pressure, when compared to the curves at greater Reynolds numbers with laminar boundary layers, may be explained by the force required to modify the flow direction to accommodate the change in surface curvature associated with the increased boundary layer thickness (or separation). These curves are most obvious on the pressure side of the body when a long favourable pressure gradient allows the development of the laminar boundary layer. The curves in Figs. 4.8(c), (d) and 4.9(a) shows examples of this for the lowest two Reynolds numbers.

- The surface pressure measurements at the highest Reynolds number leave the grouped curves over one or two streamwise points. This sudden increase in the measured surface pressure is associated with the transition from laminar to turbulent boundary layer. These curves are most evident on the suction side where the surface pressure curves of progressively lower Reynolds numbers leave the grouped curves associated with the laminar boundary layer and unite to form a shifted grouping of curves for the higher Reynolds numbers. An increase in surface pressure measurements are believed to reflect, at least in part, an increased boundary layer thickness due to the turbulent boundary layer as discussed in Subsection 4.4.1. This regrouping is shown in Fig. 4.9(b) where it occurs for all but the smallest Reynolds numbers. The deviation in surface pressure due to transition becomes difficult to observe when a rapid change in surface pressure exists due to body surface curvature effects.

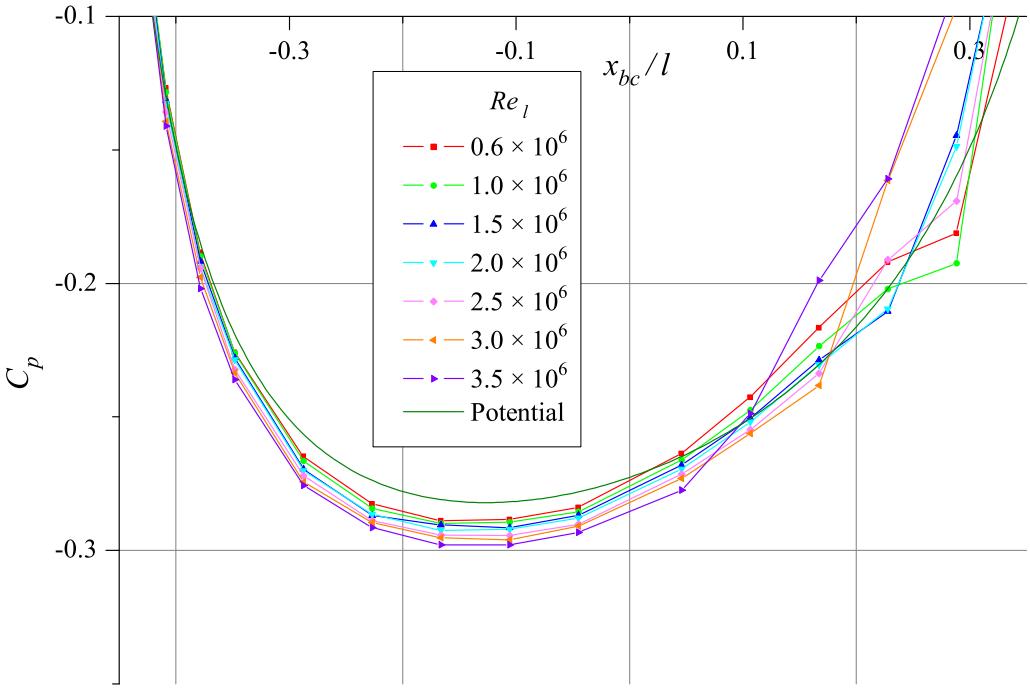

(a) Typical spread of curves with Reynolds number seen in regions with laminar flow and large azimuthal pressure gradient, $\varphi = -120°$.

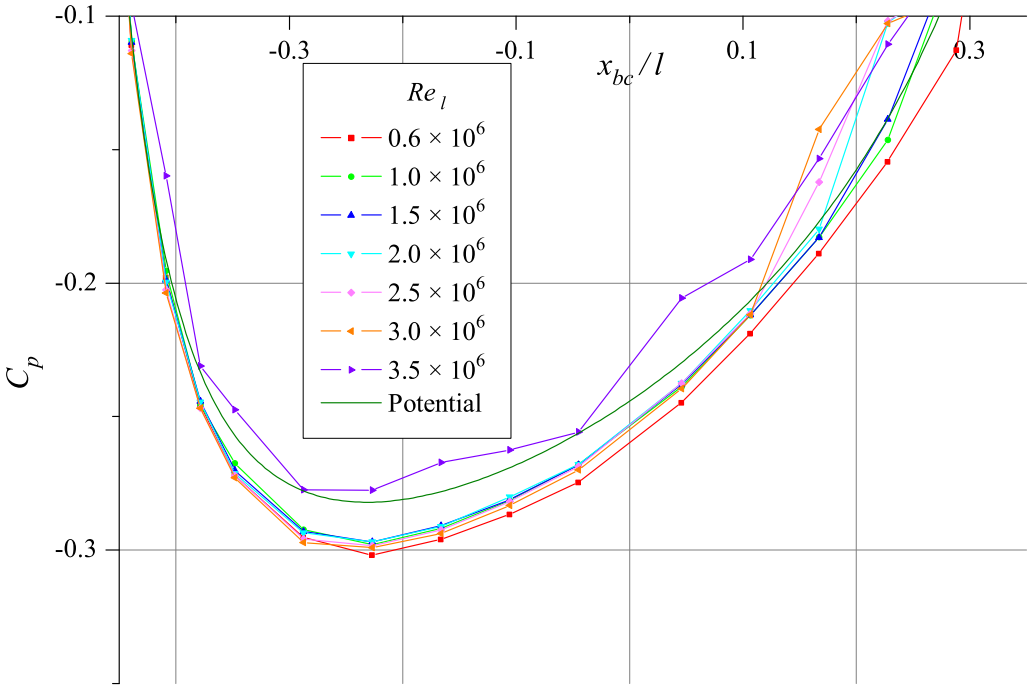

(b) Minimal spread of curves for $1.0 \times 10^6 \leqslant Re_l \leqslant 3.0 \times 10^6$ in region of negligible azimuthal pressure gradient. Boundary layer transition apparent from the rapid departure of the curve for the highest Reynolds number from the grouping of the lower Reynolds numbers, $\varphi = -180°$.

Figure 4.8: Variation of surface pressure distribution at $\alpha = -6.2°$.

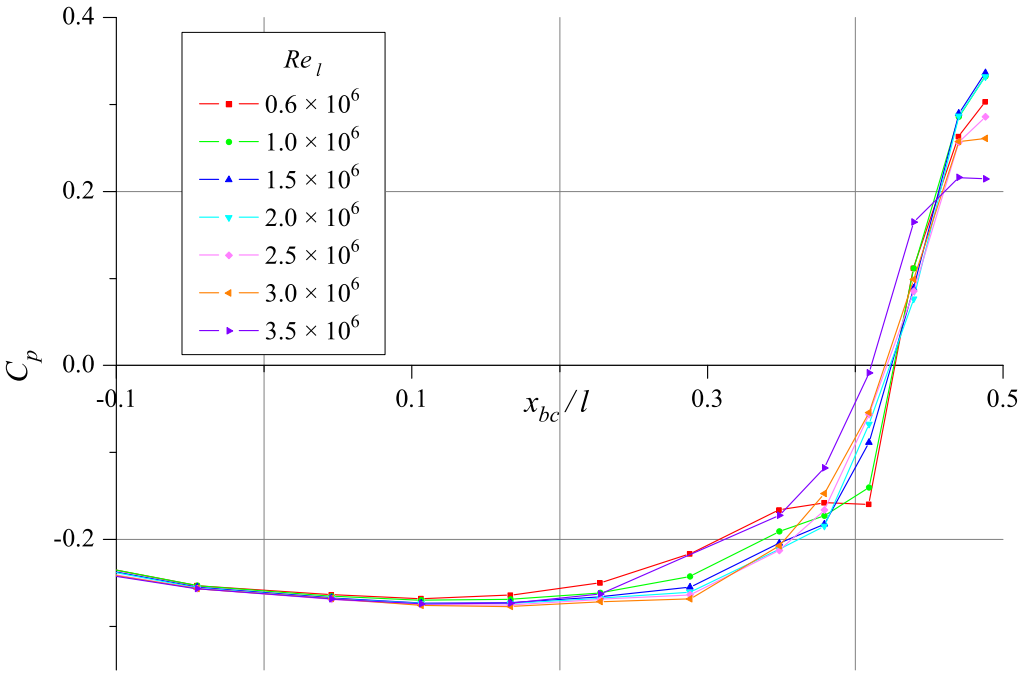

(c) Large separation bubble at lowest Re_l, $\varphi = -45°$. This separation is believed responsible for the surface pressure distributions at $Re_l = 0.6 \times 10^6$ departing from the trend displayed by those at the greater Reynolds number. The steady increase in surface pressure for the lowest three Re_l between $x_{bc}/l = 0.1$ and 0.35 results from the increased boundary layer thickness at lower Reynolds numbers.

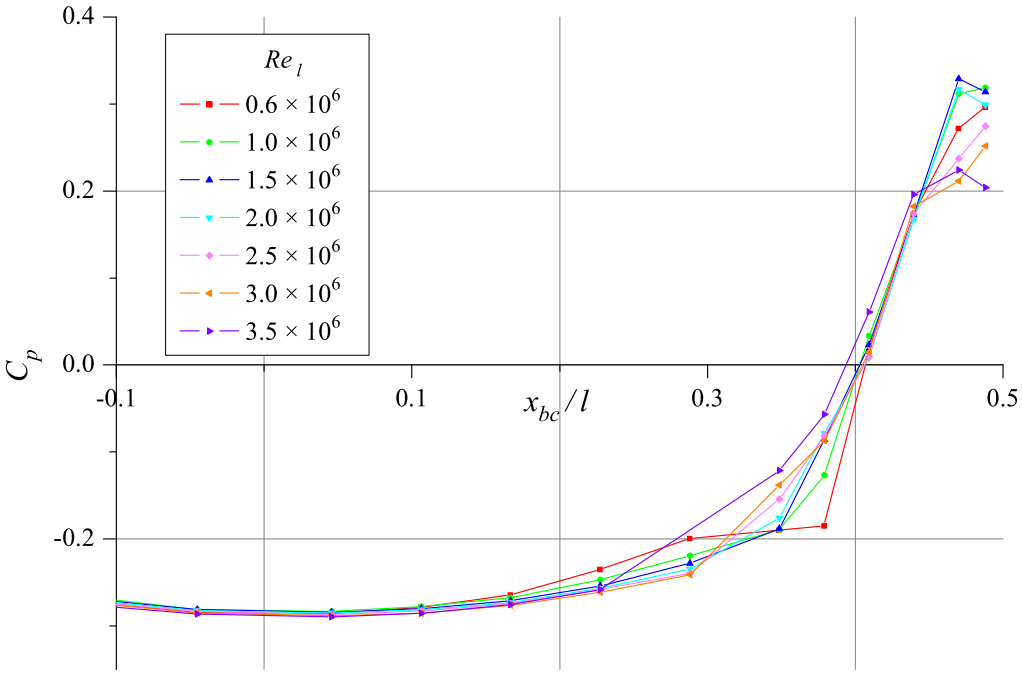

(d) Large separation bubble at lowest Re_l extends across the pressure side of the model, $\varphi = -75°$.

Figure 4.8: Surface pressure distribution at $\alpha = -6.2°$ (cont).

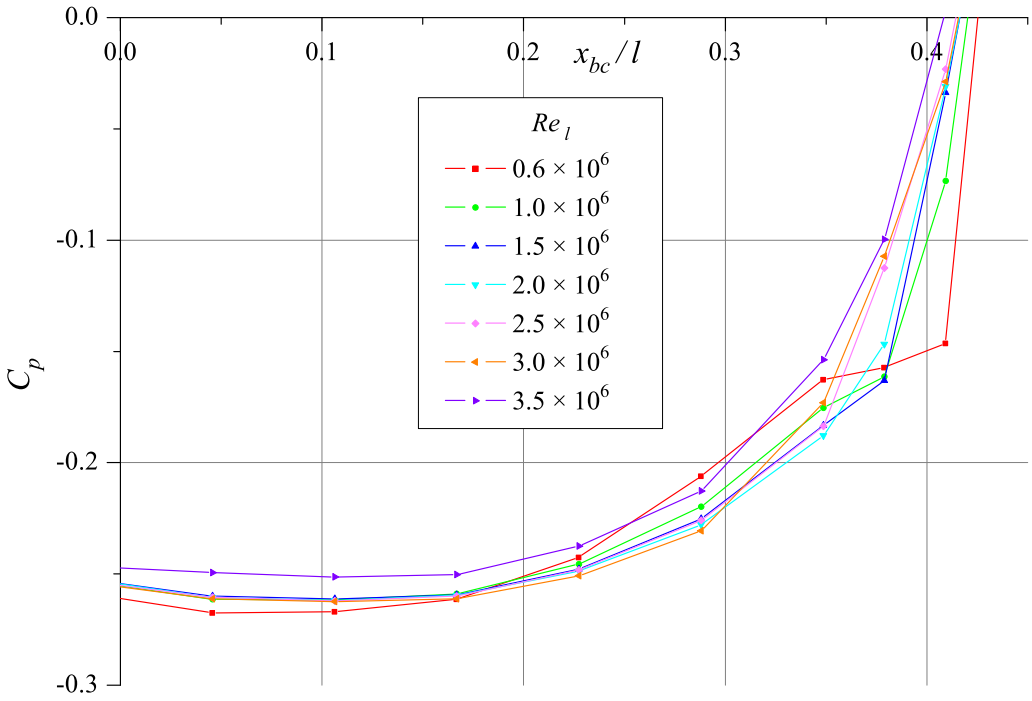

(a) Surface pressure variation with laminar separation bubble for $Re_l = 0.6 \times 10^6$ and 1.0×10^6, $\alpha = -4.2°$, $\varphi = -30°$.

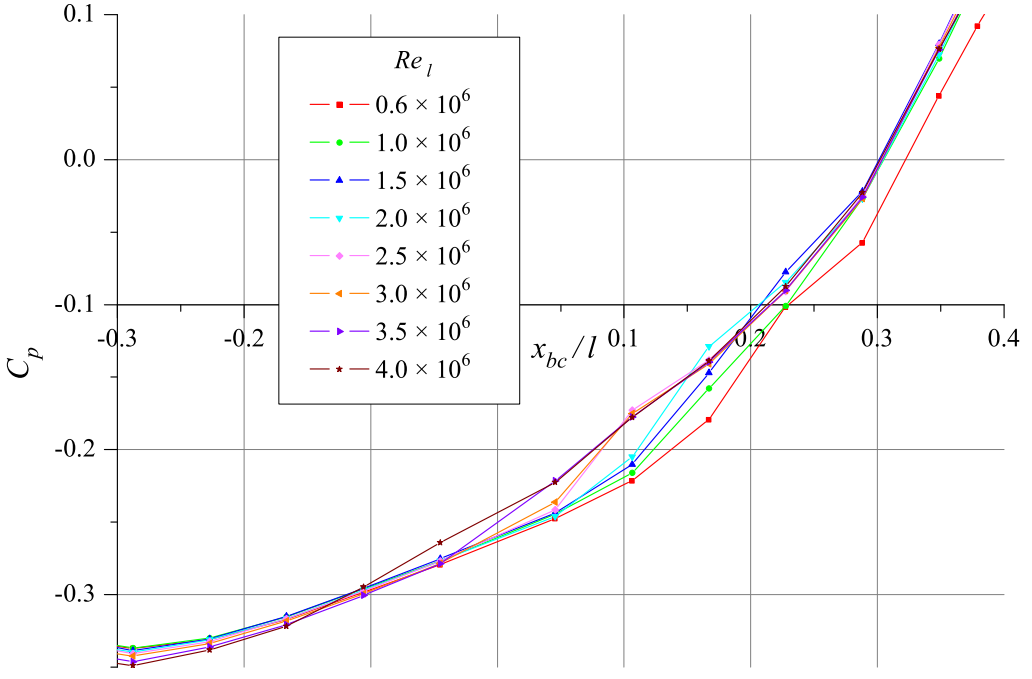

(b) Surface pressure variation during boundary layer transition for $Re_l = 1.5 \times 10^6$ to 4.0×10^6, $\alpha = -10.2°$, $\varphi = -150°$.

Figure 4.9: Surface pressure characteristics in region of adverse pressure gradient.

These features may also be observed on the pressure plots with the spheroid at $-0.2°$ incidence; however, they are more distinct with the greater range of pressure variation available at higher angles of incidence. At the two lowest Reynolds numbers the laminar separation bubble is apparent on the pressure side but decreases in extent as φ decreases. For $Re_l = 0.6 \times 10^6$ and 1.0×10^6 the laminar separation bubble is no longer discernible after $\varphi \leqslant -135°$ and $\varphi \leqslant -150°$ respectively.

Fig. 4.10 shows surface flow visualisation that supports the existence of boundary layer transition occurring near the locations of perturbations in the surface pressure distributions. Table 4.2 compares estimates for transition locations taken from the pressure plots and the flow visualisation.

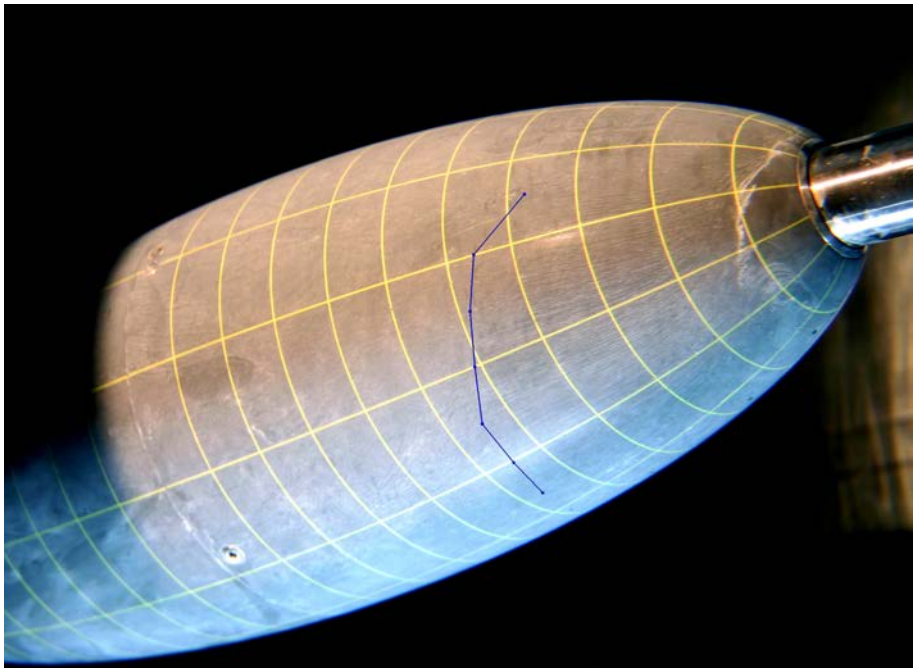

Figure 4.10: Boundary layer transition location estimated from flow visualisation on spheroid at $\alpha = 6.2°$, $Re_l = 2.0 \times 10^6$. Transition to turbulence is indicated by surface streamlines becoming apparent in the oil mixture in a region of decelerating flow. The higher wall shear stress in turbulent flow region allows the water to shift the oil mixture.

Towards the rear of the body at the lowest Reynolds number the surface pressure curve exhibits a large laminar separation bubble on the pressure side of the body. This laminar separation bubble becomes less noticeable on the suction side as φ increases from $-105°$ to $-180°$. As earlier noted this large laminar separation bubble is believed to be responsible for the surface pressure at the front of the model for this Reynolds number not following the trend seen for the other Reynolds numbers. If this is the case it is worth noting that the change in

φ	Flow Visualisation $Re_l = 2.0 \times 10^6$ x_{bc}/l	Surface Pressure $Re_l = 2.0 \times 10^6$ x_{bc}/l	Surface Pressure $Re_l = 2.5 \times 10^6$ x_{bc}/l
90°	0.29		
105°	0.28		
120°	0.27	$0.23 \leftrightarrow 0.29$	$0.17 \leftrightarrow 0.23$
135°	0.25	$0.17 \leftrightarrow 0.23$	$0.17 \leftrightarrow 0.23$
150°	0.25	$0.17 \leftrightarrow 0.23$	$0.17 \leftrightarrow 0.23$
165°	0.23	$0.17 \leftrightarrow 0.23$	$0.11 \leftrightarrow 0.17$
180°		$0.17 \leftrightarrow 0.23$	$0.11 \leftrightarrow 0.17$

Table 4.2: Comparison of estimated transition point from surface pressure and flow visualisation.

base pressure has resulted in a (minor) gradual shift in the surface pressure distributions rather than the more sudden shift in surface pressure distributions associated with laminar-turbulent transition of the boundary layer.

Reynolds Numbers 3.5×10^6

For the largest Reynolds numbers, the measured surface pressure curves on the front of the body for $-30° \geqslant \varphi \geqslant -135°$ lie with the results at the lower Reynolds numbers and continue the trend shown of transitioning upstream of the results measured at $Re_l = 3.0 \times 10^6$. When a greater adverse pressure gradient exists for a longer distance ($-150° \geqslant \varphi \geqslant -180°$) the increase in pressure associated transition due to with the thicker turbulent boundary layer moves towards the nose (Fig. 4.8(b)). Transition closer to the nose also occurred for $\varphi = 0°$ and $-15°$ at $x_{bc}/l \approx -0.1$ and $x_{bc}/l \approx -0.2$ respectively; despite the increased distance of favourable pressure gradient. This may be explained by the thinner boundary layer at these azimuthal angles being more influenced by disturbances on the surface. The most likely source for this disturbance is the tapping holes. It is worth recalling at $\alpha = -0.2°$, $Re_l = 3.5 \times 10^6$ for $\varphi = 0°$ and $-15°$ boundary layer transition occurs further upstream ($x_{bc}/l \approx -0.43$). At $\alpha = -10.2°$, $Re_l = 3.5 \times 10^6$ for $\varphi = 0°$ and $-15°$ boundary layer transition does not occur until the rear half of the model.

4.4.3 Spheroid at $\alpha = -10.2°$

A maximum Re_l of 4.0×10^6 was obtained for measurements at $\alpha = -10.2°$. Except for the azimuth angles of $0°$, $-15°$, $-165°$ and $-180°$ the transition point was not seen to shift upstream into the region of favourable pressure gradient for the largest Reynolds numbers. The surface pressure distributions for a range of Reynolds numbers is displayed in Fig. 4.11 and 4.13.

Reynolds Numbers 0.6×10^6 to 3.5×10^6

Over the region of favourable pressure gradient the measured curves have a very small spread and are close to the calculated potential line for φ between $0°$ and $-90°$. As φ approaches $-180°$ the measured curves are still grouped with a similar spread but the distance from the calculated potential line increases. In regions of small favourable pressure gradient or very slight unfavourable pressure gradient between azimuth angles of $-60°$ and $-150°$ the spread in the C_p is easily seen in Fig. 4.13(b)–(d). Between these azimuth angles C_p has the most negative values at the largest Reynolds number. As previously noted this characteristic was present to a lesser extent when the spheroid was at a $-6.2°$ incidence but not apparent when $\alpha = -0.2°$. The spread in the curves is not obvious at $\varphi = 0°$, $-15°$ and $-30°$ (Fig. 4.13(a)). This spread appears to be most apparent in areas of favourable pressure gradient with strong crossflow. A similar spread occurs with the surface pressure distributions for the ellipsoid model and are discussed in Section 5.3.

The characteristic laminar separation and transition described in Subsection 4.4.2 are present in these results in regions of adverse pressure gradient. At the lowest Reynolds numbers the laminar separation bubble is seen to occur near $x_{bc}/l = 0.4$ when φ equals $0°$ and moves upstream to $x_{bc}/l = 0.2$ as φ approaches $-120°$. For φ between $-150°$ and $-180°$ no laminar separation bubble is obvious and it appears that the flow may have transitioned. At $Re_l = 1.0 \times 10^6$ a significantly smaller laminar separation bubble is apparent for φ between $-0°$ and $-90°$ (except for $-60°$) near $x_{bc}/l = 0.4$. This laminar separation bubble decreases in size as the Reynolds number increases and is no longer apparent for $Re_l > 2.0 \times 10^6$ although the change in pressure due to transition is noted for the higher Reynolds numbers upstream. Downstream of the laminar separation bubble/transition the pressure increases rapidly for φ between $-90°$ and $-135°$ before flattening out, this flattening indicates separation of the turbulent boundary layer (Fig. 4.11(a)). The results for the lowest Reynolds number, and to a lesser extent for the next lowest, show that as φ decreases from $-150°$ there is little if any flattening in the surface pressure curve before the base (Fig. 4.11(b)). This suggests that the flow is able to stay attached near the base for the azimuth with the greatest length of adverse pressure gradient at the lowest Reynolds number.

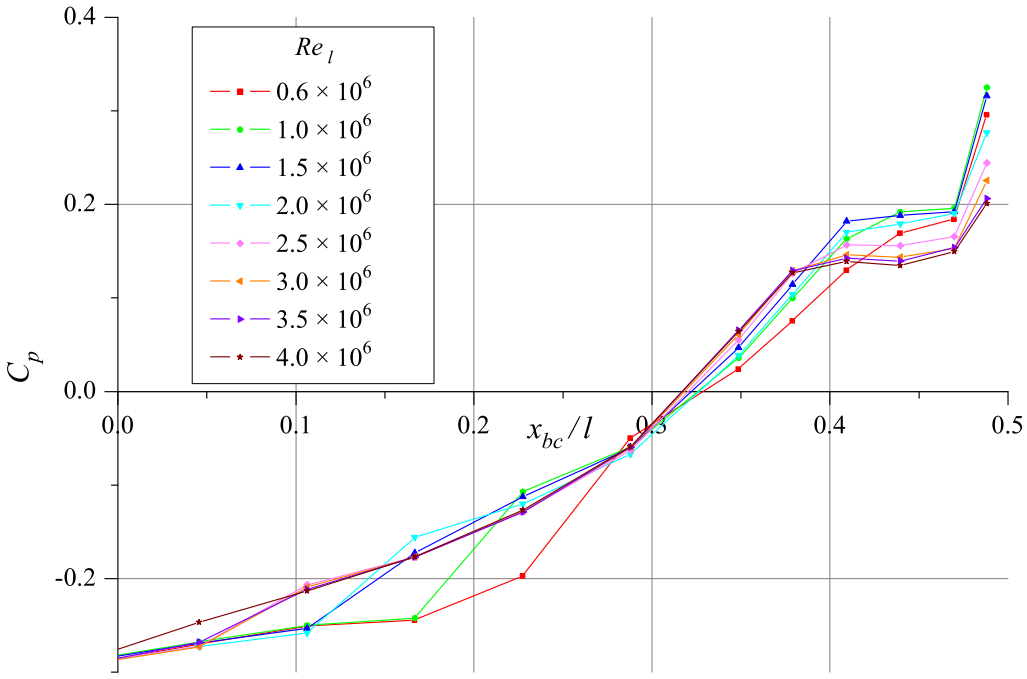

(a) Laminar seperation bubble prior to boundary layer transition for $Re_l \leqslant 1.0 \times 10^6$. Probably boundary layer transition without separation for $Re_l \geqslant 2.5 \times 10^6$. Turbulent separation on rear of the model for all Re_l, $\varphi = -135°$

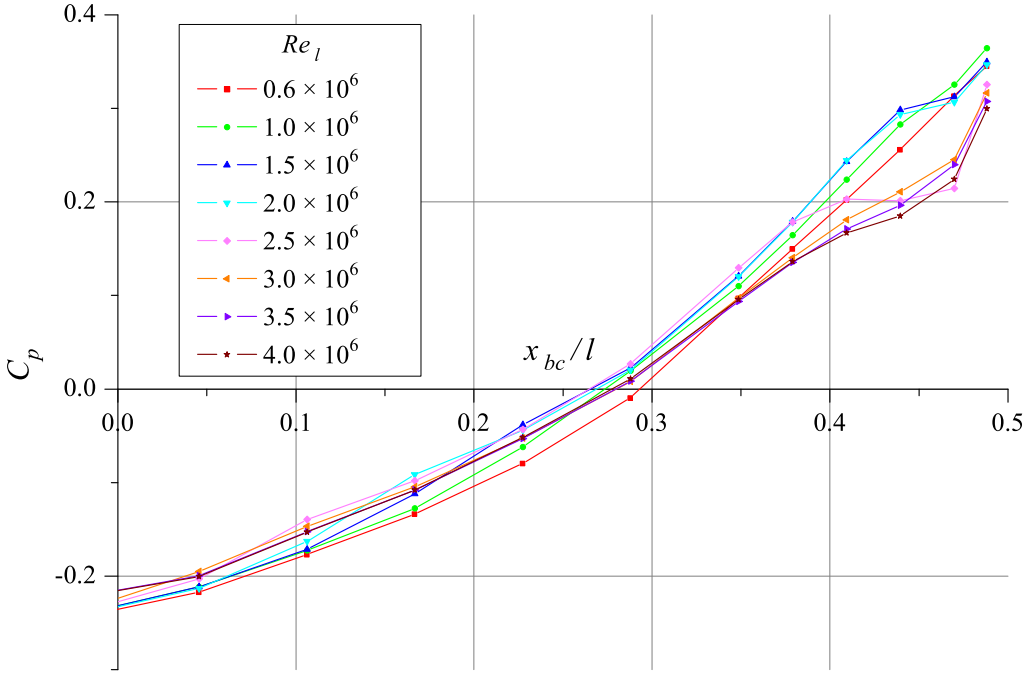

(b) Minimal separation, $\varphi = -180°$. Flow visualisation in Fig. 7.9 and 7.11 confirms flow attachment until $x_{bc}/l \approx 0.45$ for $Re_l = 2.0 \times 10^6$ and 4.0×10^6 respectively.

Figure 4.11: Surface pressure at rear of model on suction side, $\alpha = -10.2°$

The atypical behaviour of the lowest Reynolds number described in Subsection 4.4.2 is also observed for this angle of incidence. In this case it is restricted to a smaller region of the suction side, $\varphi \leqslant -165°$.

For higher Reynolds numbers a reversal in surface pressure gradient occurs near the third last port, $x_{bc}/l = 0.44$, when φ is between $-75°$ and $-120°$ (Fig. C.21). The location of this reversal in pressure gradient coincides with a large vortical structure that may be seen in the corresponding flow visualisation photos. Fig. 4.10 shows surface flow visualisation that supports the existence of boundary transition occurring near the locations shown by the surface pressure measurements. Table 4.3 compares estimates for transition location taken from the pressure plots and the flow visualisation. The perturbations in the surface pressure indicative of transition are more difficult to identify in regions where the pressure changes rapidly due to surface curvature effects.

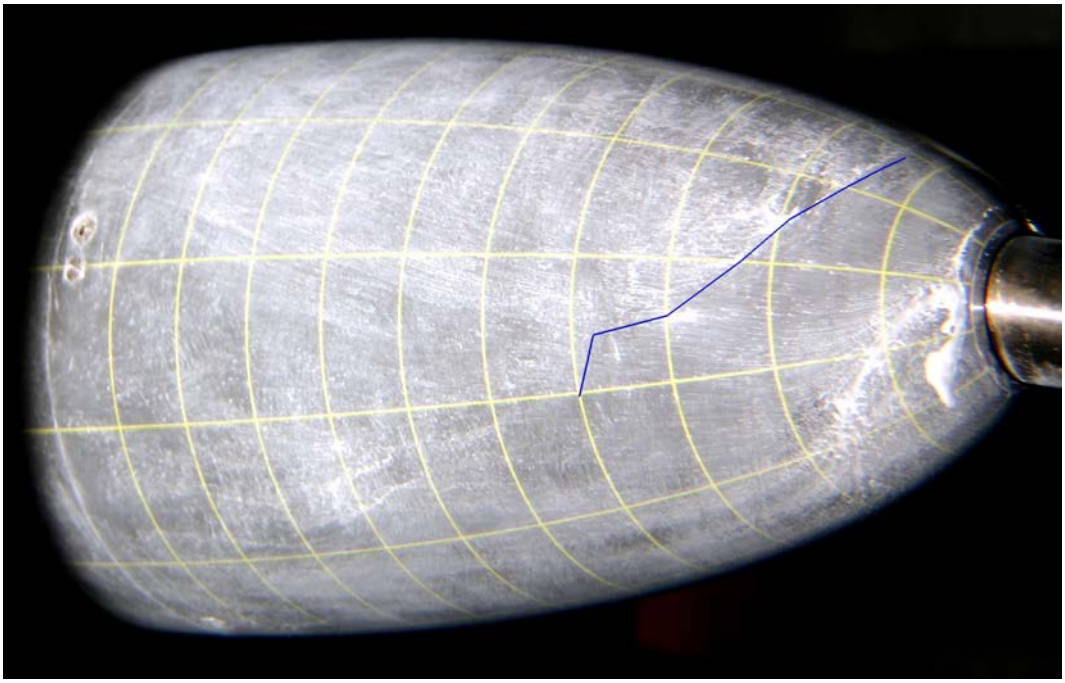

Figure 4.12: Transition estimate from flow visualisation on spheroid at $\alpha = 10.2°$, $Re_l = 2.0 \times 10^6$. Transition to turbulence is indicated by greater scouring of the oil mixture. Higher wall shear stress in turbulent flow regions increases scouring.

Reynolds Number 4.0×10^6

As previously noted, except for azimuth angles of $0°$, $-15°$, $-165°$ and $-180°$ the surface pressure measurements at $Re_l = 4.0 \times 10^6$ displayed similar characteristics to the measurements taken at lower Reynolds numbers. The measurements when the body was at $\alpha = -6.2°$ with

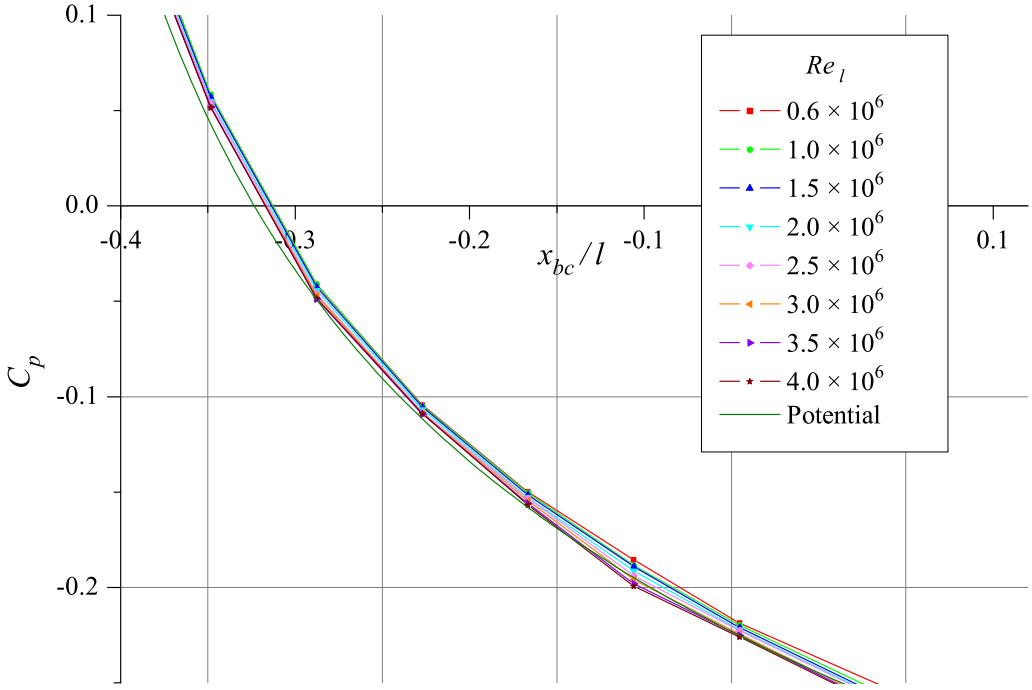

(a) $\varphi = -30°$. Minimal spread of surface pressure distribution in region of favourable pressure gradient and small azimuthal pressure gradient.

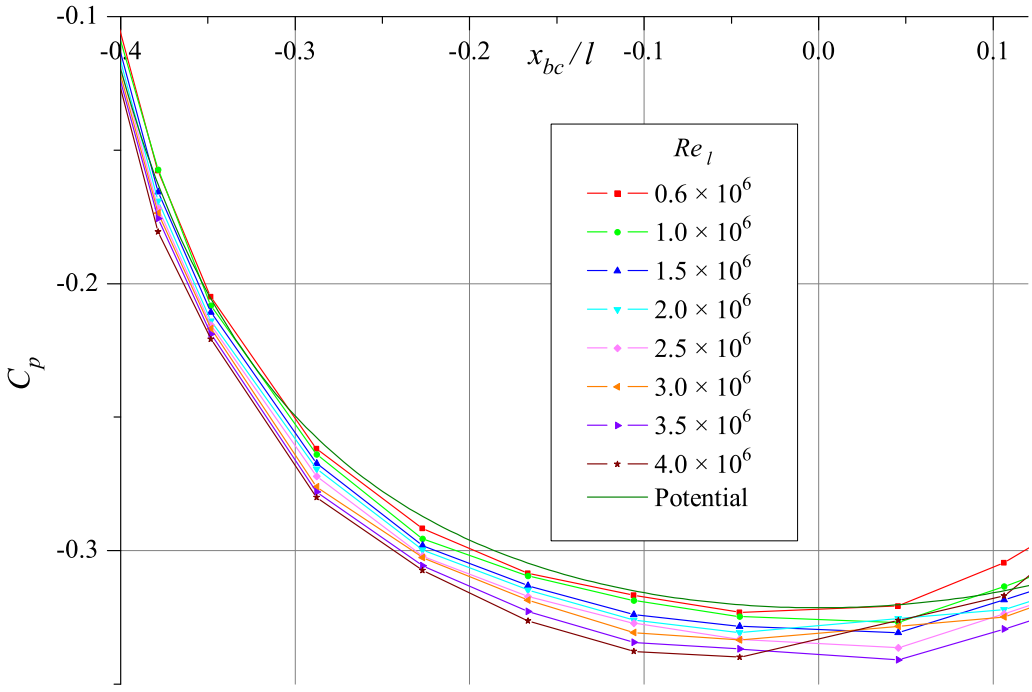

(b) $\varphi = -90°$. Larger spread of surface pressure distribution in region of extended favourable pressure gradient and large azimuthal pressure gradient.

Figure 4.13: Magnified view of surface pressure distribution on spheroid, $\alpha = -10.2°$.

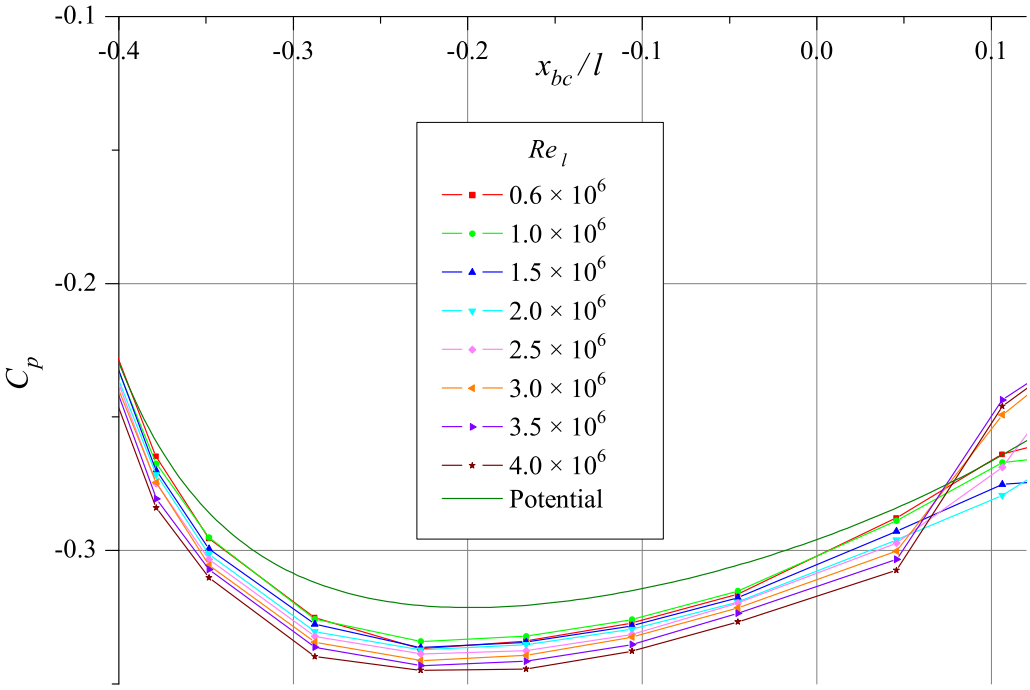

(c) $\varphi = -120°$, slightly reduced spread in surface pressure distribution.

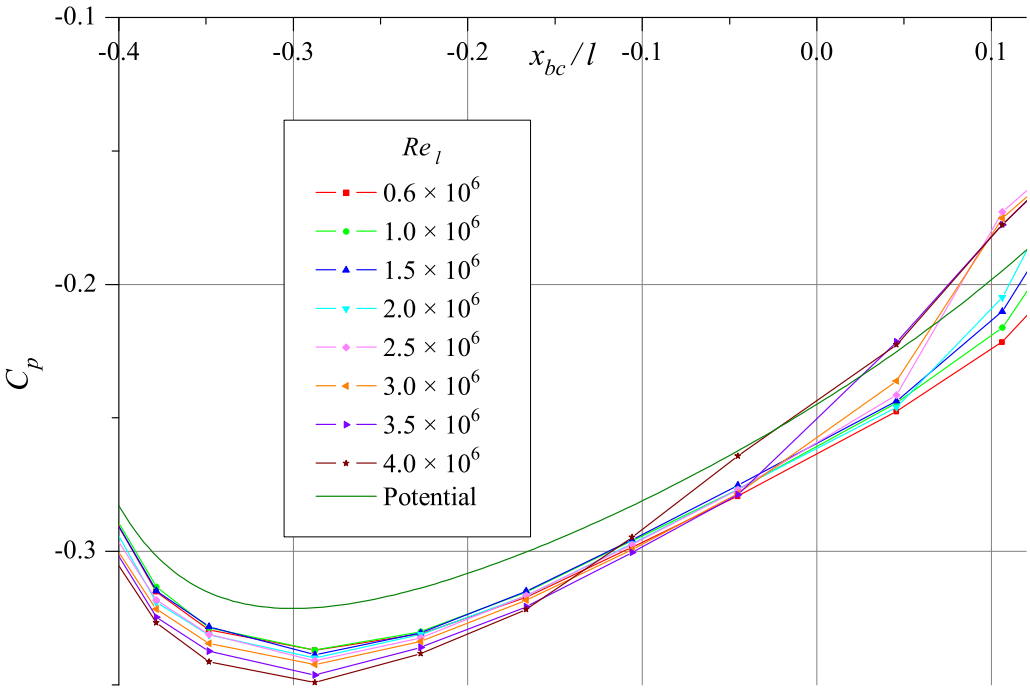

(d) $\varphi = -150°$. Slightly reduced spread in surface pressure distribution, transition of largest Re_l after short length of adverse pressure gradient.

Figure 4.13: Magnified view of surface pressure distribution on spheroid, $\alpha = -10.2°$ (cont).

φ	Flow Visualisation $Re_l = 2.0 \times 10^6$ x_{bc}/l	Surface Pressure $Re_l = 2.0 \times 10^6$ x_{bc}/l	Surface Pressure $Re_l = 2.5 \times 10^6$ x_{bc}/l
0°	0.44	0.44 →	0.41 ↔ 0.44
−15°	0.44	0.42 ↔ 0.46	0.41 ↔ 0.44
−30°	0.44	0.41 ↔ 0.44	0.41 ↔ 0.44
−45°	0.42	0.41 ↔ 0.44	0.41 ↔ 0.44
−60°	0.40	0.38 ↔ 0.41	0.38 ↔ 0.41
−75°	0.37	0.29 ↔ 0.35	0.27 ↔ 0.35
−90°	0.32	0.29 ↔ 0.35	0.23 ↔ 0.29

Table 4.3: Comparison of estimated transition points from surface pressure and flow visualisation.

$Re_l = 3.5 \times 10^6$ also showed transition moving to the nose for comparable azimuth angles. For $\varphi = 0°$ and $-15°$ the transition locations determined from the pressure measurements were close to $x_{bc}/l = -0.4$ and -0.2 respectively. The surface pressure for these azimuths is slightly greater than the that measured for the lower Reynolds number cases through to the rear of the model, $x_{bc}/l = 0.4$, where the pressure rises rapidly ahead of the corresponding rise at the lower Reynolds number. The base pressure (Port 24) for these measurements and the ones at lower Reynolds numbers showed variations in C_p of up to 0.12 for individual Reynolds numbers. When the boundary layer was tripped this variation in C_p reduced to less than 0.01 across all the Reynolds numbers for which the boundary layer was tripped. Fig. 4.2 shows this result. The base pressure may be susceptible to significant variation due to relatively small changes in the boundary layer, as the pressure is changing rapidly near the base.[1]

4.4.4 Spheroid at $\alpha = -10.2°$, Boundary Layer Tripped at 20% of Total Length

The boundary layer on the spheroid was tripped at $x_{bc}/l = -0.3$, between 6^{th} and 7^{th} pressure taps, using circular elements of $1.25\,mm$ diameter, spaced $2.5\,mm$ apart centre to centre. The height of the trip strip, $0.16mm$, was determined using the technique of Braslow and Knox [58].

[1] Examining the base pressure (Port 24), ideally constant for all values of φ, it is noticeable that it deviates for the higher Reynolds number at $\varphi = -165°$ and $-180°$ and to a lesser extent does the same for $\alpha = -6.2°$. This may not be the correct conclusion however as the testing with the ellipsoid has the tappings either up or down and there appears to be no definitive difference in the base pressure for the readings with the taps up verses down.

A critical roughness Reynolds number Re_k of 400 rather than the more commonly quoted value of 600 [59] was chosen. Re_k of 600 is based on the maximum probable height in a distribution of sand particles. When elements of uniform height create the trip strip the work this value was drawn from [60] suggests that a lower value for Re_k is suitable. The trip was designed to promote turbulent flow for $Re_l \gtrapprox 1.3 \times 10^6$ ($\approx 4\ ms^{-1}$ at $20°C$). The momentum thickness, θ, for these conditions at zero degrees incidence was calculated by applying the Mangler transformation to Thwaites' method [14]. The ratio of fluid velocity at the edge of the boundary layer to the freestream velocity was determined from the surface pressure distribution determined from potential theory. The calculated momentum thickness using Thwaites' method at $x_{bc}/l = -0.3$ when the spheroid was at zero incidence was $55\ \mu m$ ($Re_\theta = 220$).

The trip strip was cut into self adhesive PVC sheet by a Roland Camjet vinyl cutter. The material used in this case was a reflective Class 2 engineering vinyl, chosen for its thickness of $0.15\ mm$. A range of other thinner sheets was readily available. The circular elements were cut into the centre of $330\ mm$ long by $10\ mm$ wide strips. The required length of pre-cut vinyl strip was then firmly pressed onto the surface. The strip was then gently peeled back with care being taken to ensure that the circular elements were left on the surface of the model. These trip strips were relatively quick to apply, provided elements uniform in height and thickness, required no waiting for glue to set, had little increased difficult when applied to doubly curved surfaces, and had excellent adhesion with only a minimal loss of elements throughout testing and handling. The elements are shown on the model in Fig. 4.14 with the tunnel running at $12\ ms^{-1}$ and cavitation occurring at the elements. The pressure was set during testing to ensure that no cavitation occurred.

The trip strip is seen in Fig. 4.15 to have minimal influence on the surface pressure at low Reynolds number, while effectively leading to a Reynolds number independent surface pressure at the higher Reynolds number. The results obtained at the higher Reynolds numbers were similar to those obtained when the boundary layer transition moved forward to the front section of the nose at $\alpha = -10.2°$.

Reynolds Numbers 0.6×10^6 to 1.0×10^6

The surface pressure measurements show similar characteristics to those seen at this incidence without the trip strip. A laminar separation bubble near $x_{bc}/l = 0.4$ when $\varphi = 0°$ moves upstream to $x_{bc}/l = 0.2$ as φ approaches $-135°$. It is interesting to note that at $\varphi = 45°$ the laminar separation bubble disappears for $Re_l = 1.0 \times 10^6$ for the non-tripped flow; a similar change in the laminar separation bubble occurs at $\varphi = 60°$ for the results of the tripped spheroid. Unfortunately the flow visualisation was unsuccessful at this Reynolds number so the

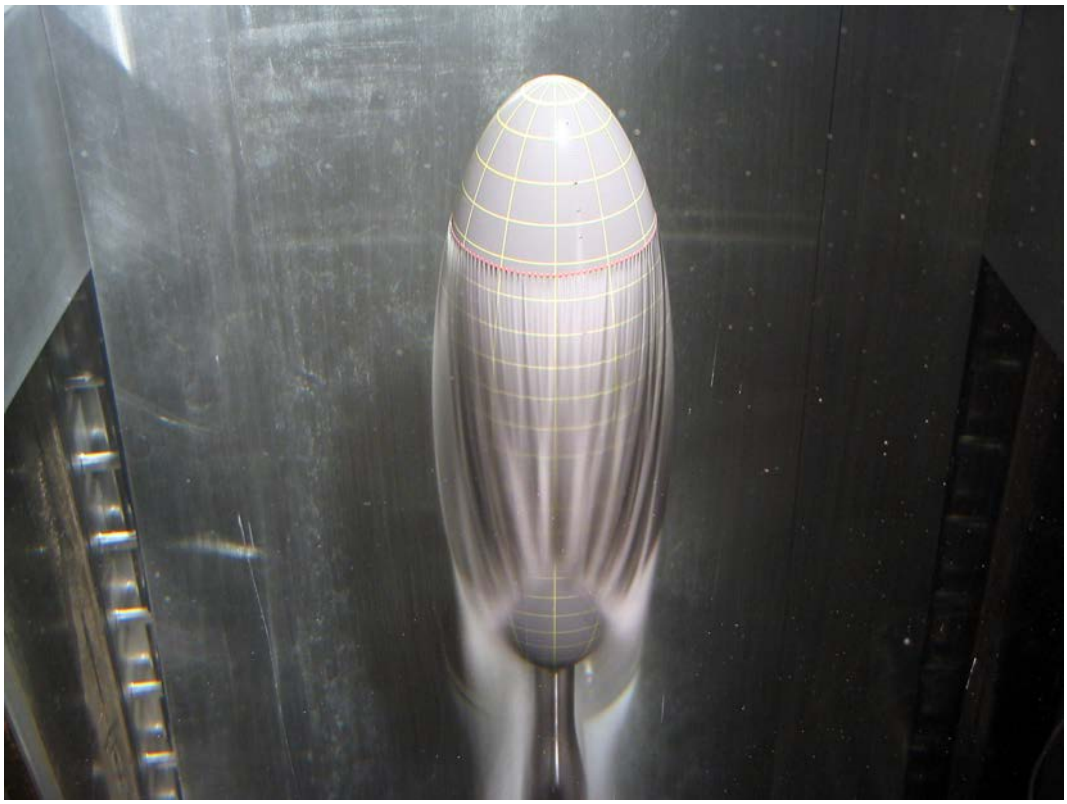

Figure 4.14: Cavitation inception at trip strip on spheroid

flow topology for these conditions is uncertain.

Reynolds Numbers 1.5×10^6 to 4.0×10^6

The measured surface pressures for flows between $Re_l = 1.5 \times 10^6$ and 4.0×10^6 are extremely close, showing that the trip has successfully created a Reynolds number independent flow over this range. The main difference is that in some cases the lower Reynolds number curve in this range does not join the grouping of tripped curves until the second tap after the trip showing, that it takes a greater distance for the trip to destabilise the boundary layer at the lower Reynolds number.

Over the front of the model before the trip strip where a favourable pressure gradient exists ($\varphi > -90°$), the measured surface pressure is close to the pressure calculated from potential theory. In regions of adverse pressure gradient before the trip the measured surface pressure is less than the calculated pressure. After the trip strip, placed just before the 7^{th} tap, the measured surface pressure increases in a manner similar to that seen with unforced transition. On the rear of the model from $\varphi = -45°$ through to $\varphi = -120°$ the pressure increases upstream of the location observed for the non-tripped lower Reynolds numbers. A small flattening of

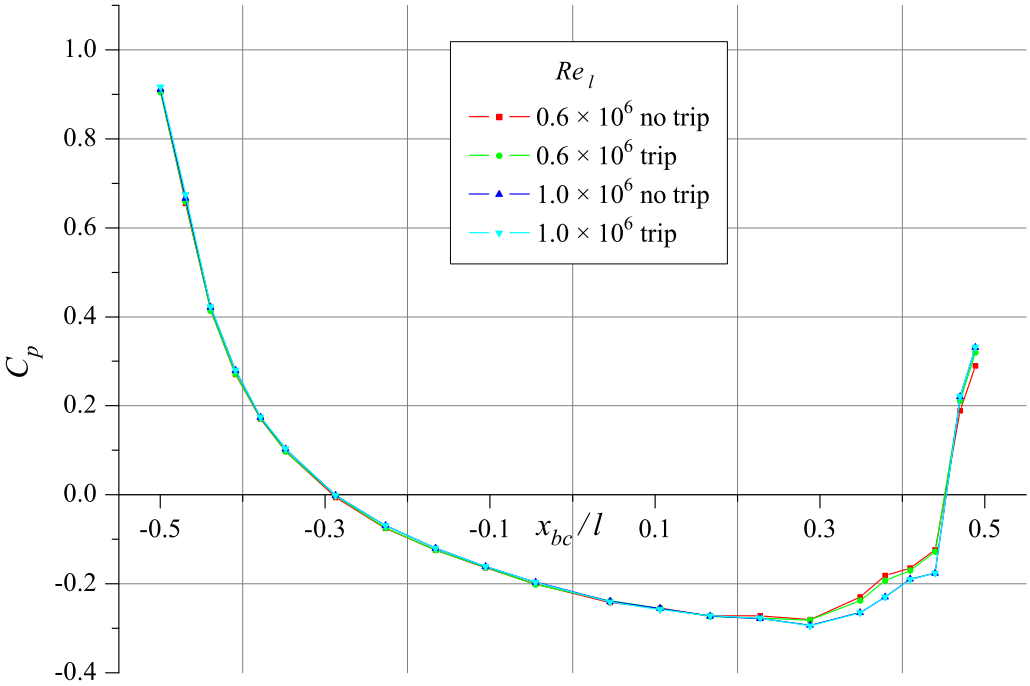

(a) Low Reynolds number trip strip comparison at $\varphi = 0°$. No definitive difference in surface pressure distributions with and without the trip strip prior to the Reynolds numbers when it becomes effective ($Re_l \leqslant 1.3 \times 10^6$).

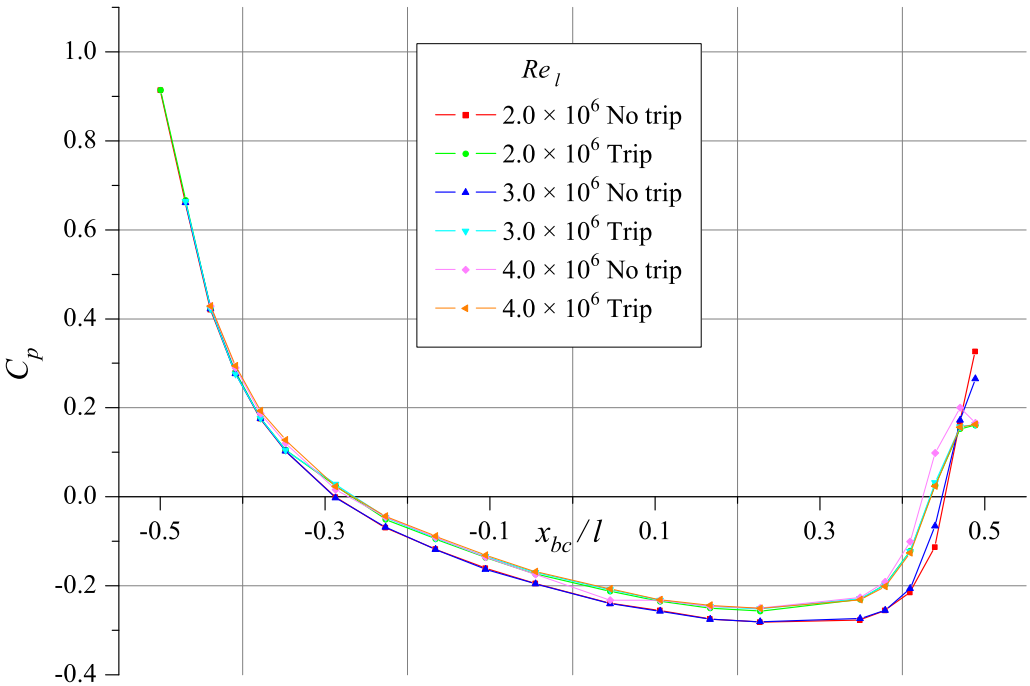

(b) High Reynolds number trip strip comparison at $\varphi = 0°$. Reynolds number independence for tripped results for $2.0 \times 10^6 \leqslant Re_l \leqslant 4.0 \times 10^6$. The tripped results display a high degree of correlation with the untripped results at $Re_l = 4.0 \times 10^6$.

Figure 4.15: Surface pressure distribution for tripped and untripped spheroid, $\alpha = -10.2°$.

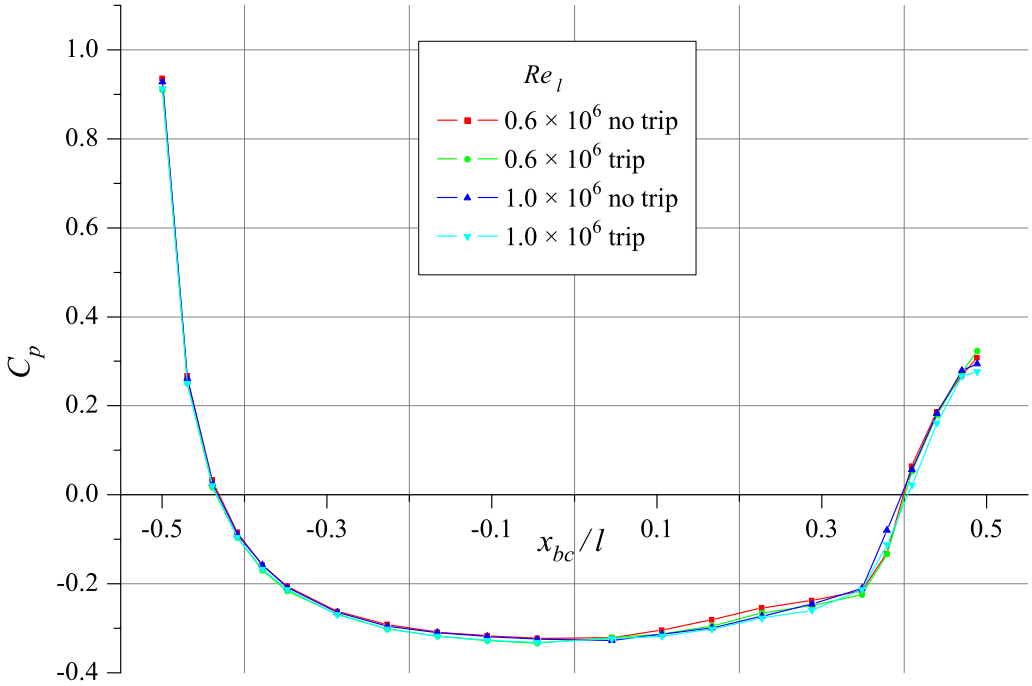

(c) Low Reynolds number trip strip comparison at $\varphi = -90°$. Minimal difference in surface pressure distributions with and without the trip strip prior to the Reynolds numbers when it becomes effective ($Re_l \leqslant 1.3 \times 10^6$).

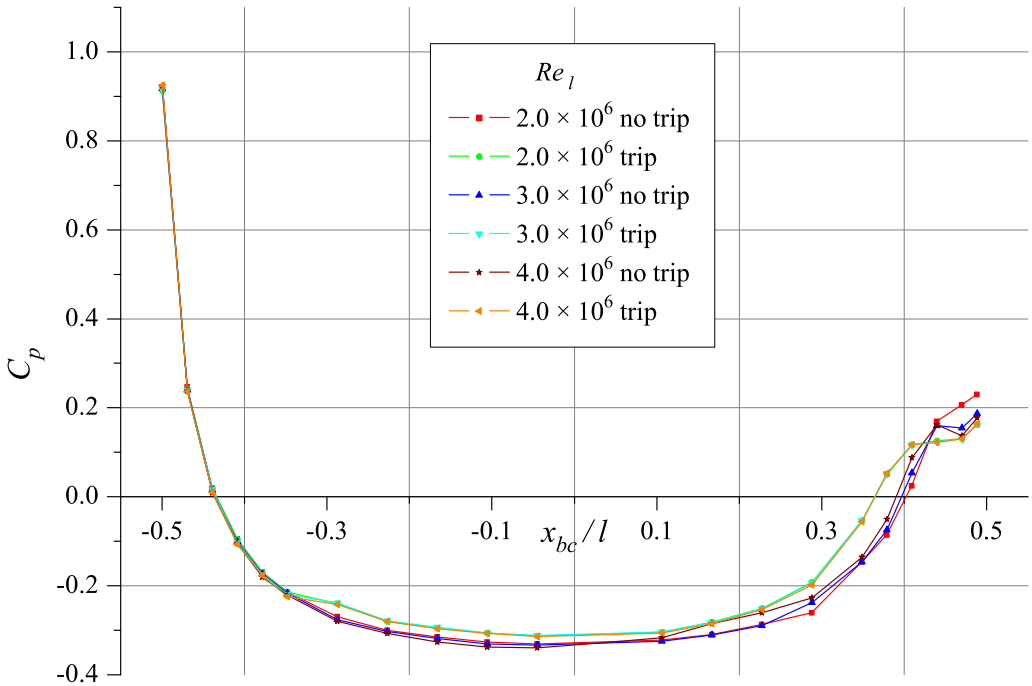

(d) High Reynolds number trip strip comparison at $\varphi = -90°$. Reynolds number independence for tripped results for $2.0 \times 10^6 \leqslant Re_l \leqslant 4.0 \times 10^6$.

Figure 4.15: Surface pressure distribution on tripped and untripped spheroid, $\alpha = -10.2°$ (cont).

the curve at $\varphi = -30°$ moves upstream to $x_{bc}/l = 0.38$ as $\varphi \to -105°$. This flattening of the surface pressure curve at the base of the model is maintained through to $\varphi \to -150°$, after which it reduces in size and gains a small gradient. The existence of a major separation at this point is supported by the corresponding flow visualisation.

4.5 Summary

The high level of precision obtained in the surface pressure measurements allows small variations in the surface pressure to be measured. Comparison of variations in surface pressure with Reynolds number have allowed the identification of surface pressure changes due to thickening boundary layers, laminar–turbulent boundary layer transition, laminar separation bubbles, and turbulent flow separation. However, the ability to identify these features is reduced in regions of rapid change in surface pressure due to surface curvature effects.

The main source of uncertainty in the results was due to the sensitivity of the boundary layer to minor surface variations. This was evident as tripping the boundary layer improved repeatability of the base pressure to better than 1% (Fig. 4.2). The base pressure is expected to be sensitive to minor variations in flow due to the rapid change in pressure at the rear of the model.

Over the front $\frac{1}{3}$ to $\frac{1}{2}$ of the model the surface pressure calculated using the classical potential flow method was comparable to the measured surface pressure. The agreement was poorer on the suction side of the model and of little relevance on the rear of the model. This agreement is consistent with the increasing thickness of the boundary layer downstream and on the suction side. These calculations of potential flow make no allowance for the displacement of the freestream flow due to the increased boundary layer thickness. The separation of the boundary layer is also not calculated as the potential calculations show full pressure recovery. Even with these limitations the curves provide a useful reference. A comparison between measurements and potential flow calculations by Meier and Kreplin [55] at incidences of 0° and 5° shows a similar trend with the measured C_p increasing more rapidly downstream of the centre than the potential calculations. The most downstream pressure measurements of Meier and Kreplin [55] occur near $x_{bc}/l \approx 0.44$,[2] on the finer 6–1 spheroid; this location is not far enough downstream to observe the flattening of the C_p curve associated with boundary layer separation at the rear of the body for incidences of 0° and 5°. The characteristic flattening of the C_p curve in regions of separated flow is apparent in the C_p curves of Ahn [26] when examining the pressure distribution in regions experiencing crossflow separation for the spheroid at high

[2]Assuming the origin is located at the centre of the body, in the coordinates of Meier and Kreplin, who measure from the nose this is at $x/2a = 0.94$.

angles of incidence.

The laminar-turbulent transition location was determined from the surface pressure measurements using curves for a range of Reynolds numbers plotted in the direction of the major axis of the spheroid. The transition process was identified when the curve for the highest Reynolds number in the range showed a small sudden shift in the positive direction. This was generally followed (downstream) by the curve for the next largest Reynolds number in the group of curves undergoing a similar shift to joining the curve for the higher Reynolds number. This process was often repeated until a new group of high Reynolds numbers was formed (Fig. 4.9(b), Fig. 4.13(d)). When the boundary layer was tripped, all the curves for Reynolds numbers above that for which the trip was designed showed a similar shift shortly after the location of the trip (Fig. 4.15(d)).

The surface pressure curve for the lowest Reynolds number was seen to not follow the trend seen for the curves for the higher Reynolds number. This is believed to be associated with a large laminar separation bubble on the pressure side.

A small but definite spread in the surface pressure was seen in regions where both extended favourable pressure gradients (or slight adverse gradient) and crossflow exist. The spread has the pressure slightly greater at the lower Reynolds numbers (Fig. 4.13(b)–(d)) and is further discussed in Section 5.3.

Chapter 5

4.2–2–1 Ellipsoid Surface Pressure Measurements

5.1 Experimental Setup

A separate model was constructed for the surface pressure measurements. This ellipsoid had a tapping at the nose and seven series of tappings running from front to rear. Each series comprised 20 tappings, except for the sets at 0° and −15° which did not include the most downstream tapping. The values of azimuthal angle mapped to an ellipse, φ_e, for these tapping series were 0°, −15°, 30°, −45°, 60°, −75° and 90°. The coordinate system used with the ellipsoid is the same as that used with the spheroid (Fig. 3.2) with the ellipsoid's shortest axis aligned with the z_{bc} direction. Alternating the tappings across the vertical plane $y_{bc} = 0$ allowed an increased separation between tappings, facilitating the manufacture of the model. The measurements on the opposing side of the model (−90°, 105°, −120°, 135°, −150°, 165° and −180°) were obtained by rotating the model 180° about its longitudinal axis, x_{bc}. In order to be consistent with the measurements taken for the spheroid the results will be graphed and referenced as negative azimuthal angles (0°, −15°, −30°, ..., −165° and −180°). φ_e is calculated from the mapping of a circle to the ellipse that forms the minor axes of the ellipsoid, as given by

$$\varphi_e = tan^{-1}\left(\frac{c_e}{b_e} tan\,(\varphi)\right) \tag{5.1}$$

where b_e and c_e are the minor axis lengths in the y_{bc} and z_{bc} directions respectively. The streamwise location for these tappings was identical to those for the spheroid except:

- at $\varphi_e = 0°$, −15° and 30°, Port No. 22 is located as noted in Table 5.1.

- at $\varphi_e = 30°$, Port No. 23 is located as noted in Table 5.1.
- at $\varphi_e = 0°$ and $-15°$, Port No. 23 does not exist.

Port No. 24 was used to measure the base pressure. Flexible tubing was used to connect the tappings to a manifold. Two manifolds were used for each row: one for the front half of the model, and one for the rear half. The use of separate manifolds for the front and rear allow these parts of the model to be handled separately. When the pressure from a row of tappings is to be measured, the manifolds from that row are connected to two manifolds attached via flexible tubing to the Scanivalve. The manifolds were joined by two small screws with a rubber gasket providing a seal. When a row of tappings was not required, the manifold was blocked with a rubber gasket and a blanking piece to prevent flow. The equipment was otherwise as used for the surface pressure testing with the spheroid.

Port No.	Tap No.	x_{bc} (mm)	x_{bc}/l
22	20	142.5	0.432
23	21	150.0	0.455

Table 5.1: Modified axial location of surface pressure tappings.

5.2 Ellipsoid Surface Pressure Results

The surface pressure measurements on the ellipsoid were conducted for Re_l values between 0.65×10^6 and 4.0×10^6, as a water temperature of at least $20°C$ was available for this testing. The distance between the tubes and the edge of the manifold proved to be less than desirable for easy reliable operation. The gasket would squeeze out if tightened too firmly, or not seal if inadequate pressure was applied. Despite care being taken in mating the manifolds, some measurements have had to be deleted due to concerns with possible leakage. The joins between the tapping and the flexible tubing closest to the centre at φ_e equal to $0°$ and $-15°$ were damaged during testing due to the cramped conditions inside the model; the affected measurements were deleted. The surface pressure calculated using classical potential theory (Appendix A) is plotted on many of the figures and used as a reference during the discussion.

For $\alpha = -0.2°$ the readings at $\varphi_e = -90°$ and $90°$ allowed the yaw alignment of the model to be checked (Fig. 5.1). The suspected influence of the support foil is evident on the measurements at $0°$ and $-180°$. The classical potential calculations show the surface pressure for any pair of readings equidistant from $\varphi_e = 90°$ ($0°$ and $-180°$, $-15°$ and $-165°$, etc.) to be a mirror image about $x_{bc}/l = 0$. In this case the influence of the support foil is believed to have increased the

pressure on the upper surface of the ellipsoid, forcing the intersection of the surface pressure curves for 0° and −180° downstream except for the case at $Re_l = 0.65 \times 10^6$.

An inspection of the surface pressure measurements at the nose tap for $\alpha = -0.2°$ is used to provide an estimate of the accuracy of the measurements. The worst measurements are just over 0.01 from the expected C_p value of unity at the nose (Fig. 5.2).

The precision of the measurements was estimated from the standard deviation of the mean using the equations developed in Section 4.3. The error bars on Fig. 5.3 show three times the standard deviation of the mean.

5.2.1 Ellipsoid at $\alpha = -0.2°$

Due to its non-axisymmetric shape there are strong azimuthal pressure gradients near the front of the model even with an essentially zero incidence, as displayed in Fig. 5.4. The model has flow symmetry, and thus a zero pressure gradient in the vertical plane (through $\varphi_e = 0°$ and $-180°$). The influence of the support, and to a lesser extent the slight incidence, prevent the flow about the horizontal plane (through $\varphi_e = 90°$ and $-90°$) being symmetrical for this incidence. However, it should be close to symmetrical.

With this model, as for the spheroid at incidence, the tapping series do not necessarily follow the surface streamlines. Strong crossflows result in surface pressure measurements that are more complex to interpret.

Reynolds Numbers 0.6×10^6 to 2.5×10^6

For the Reynolds numbers in this range the measured surface pressures over the front of the model are close to the values calculated using classical potential theory. There is a tendency for the measured pressure to be a fraction greater on the upper surface ($\varphi_e = 0°$), trending to a fraction lower than the potential curve on the under side. This trend was also seen with the spheroid and is believed to be due to the blockage associated with the support foil.

On the front of the model, where strong azimuthal pressure gradients exist, the surface pressure measurements exhibit a spread with Reynolds number. The lower the Reynolds number, the (slightly) greater the surface pressure. In some cases the lowest Reynolds number observations may not follow this trend where the flow has a laminar separation bubble at the rear. The magnified results in Fig. 5.5 show the lack of spread on the symmetry plane at $\varphi_e = 0°$ and $-90°$. The spread in the results is apparent at $\varphi_e = -75°$ and $-105°$. This appears to be the same characteristic as observed on the spheroid at incidence; but in this case the azimuthal pressure gradients are due to the model geometry rather than the incidence of the model.

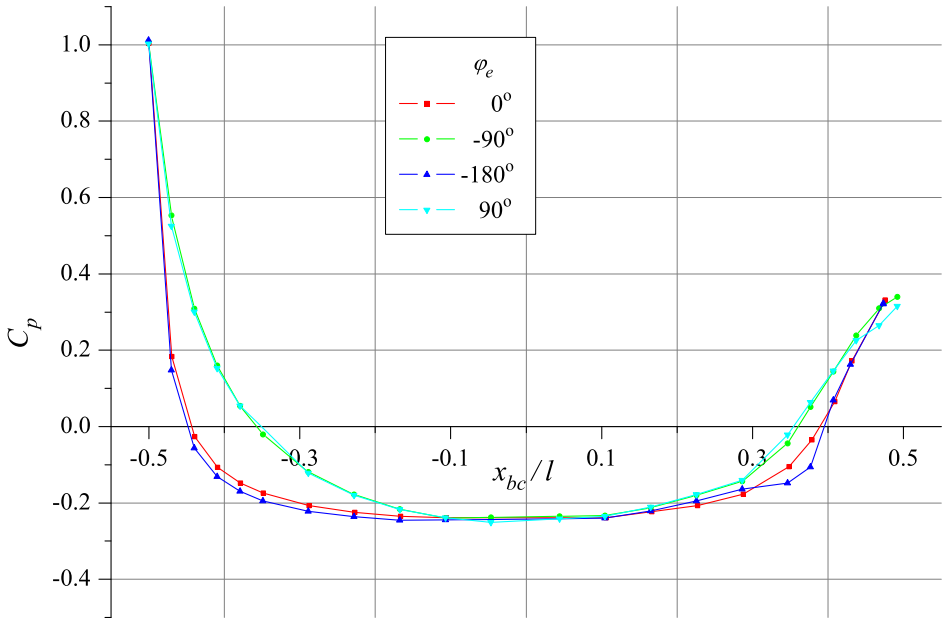

(a) $Re_l = 0.65 \times 10^6$

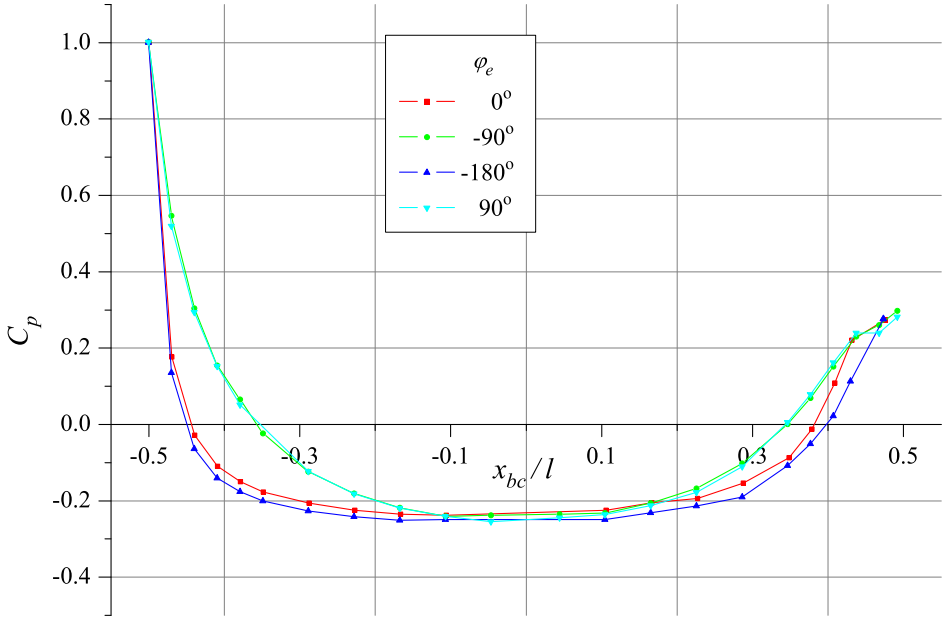

(b) $Re_l = 2.0 \times 10^6$

Figure 5.1: Comparison of surface pressure distributions on ellipsoid used to confirm alignment, $\alpha = -0.2°$

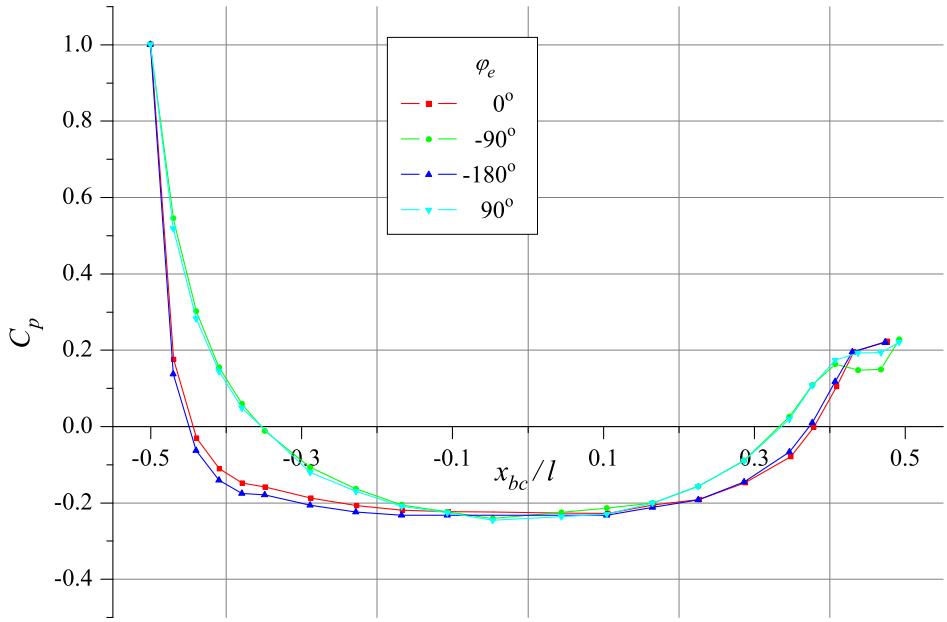

(c) $Re_l = 3.0 \times 10^6$

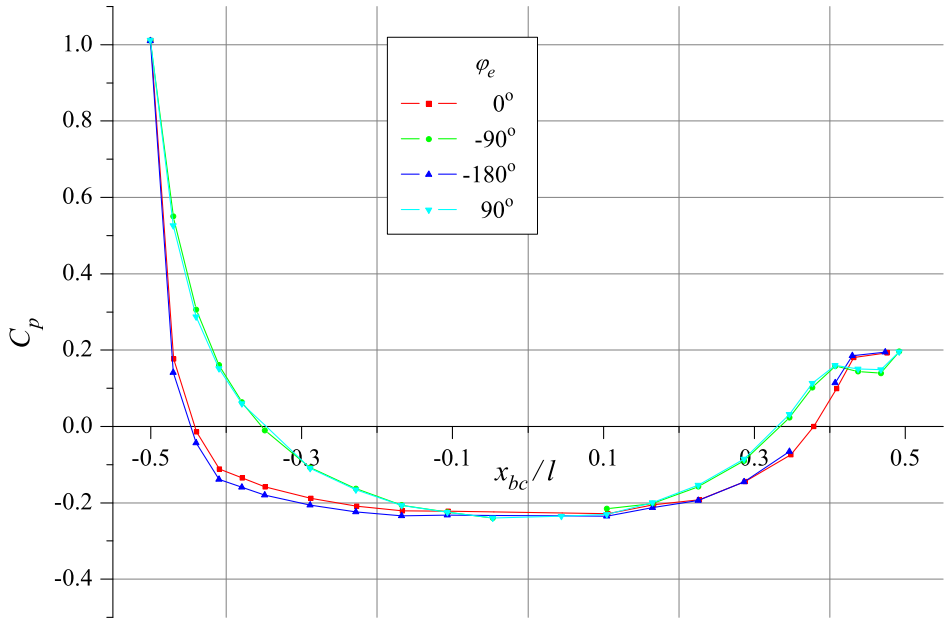

(d) $Re_l = 4.0 \times 10^6$

Figure 5.1: Comparison of surface pressure distributions on ellipsoid used to confirm alignment, $\alpha = -0.2°$ (cont)

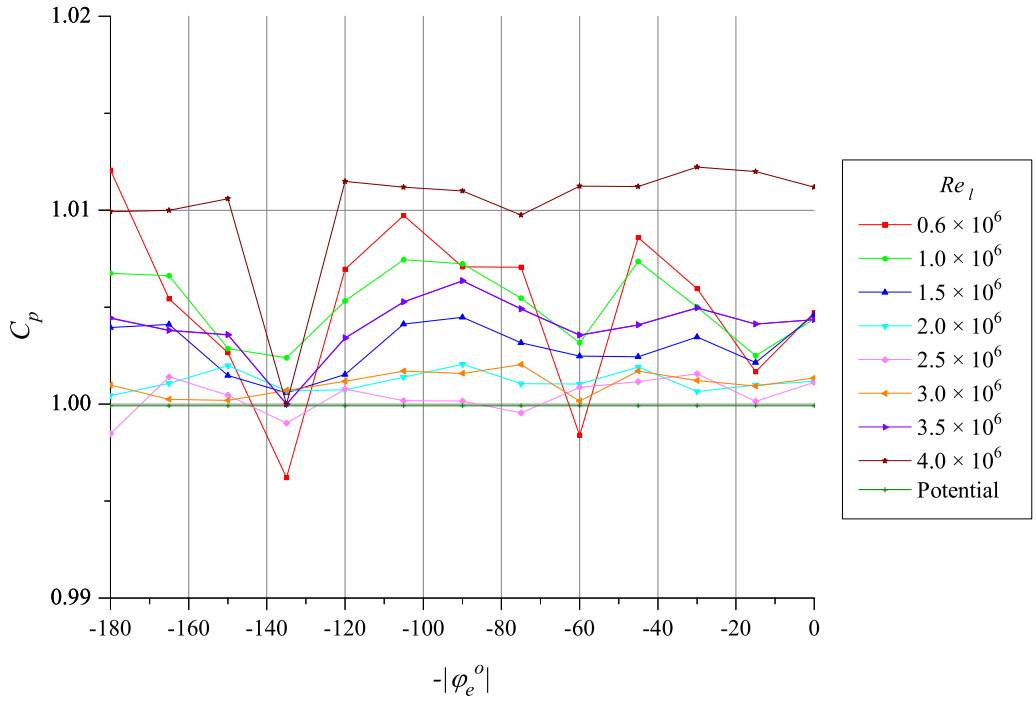

Figure 5.2: Comparison of nose pressure values, $\alpha = -0.2°$

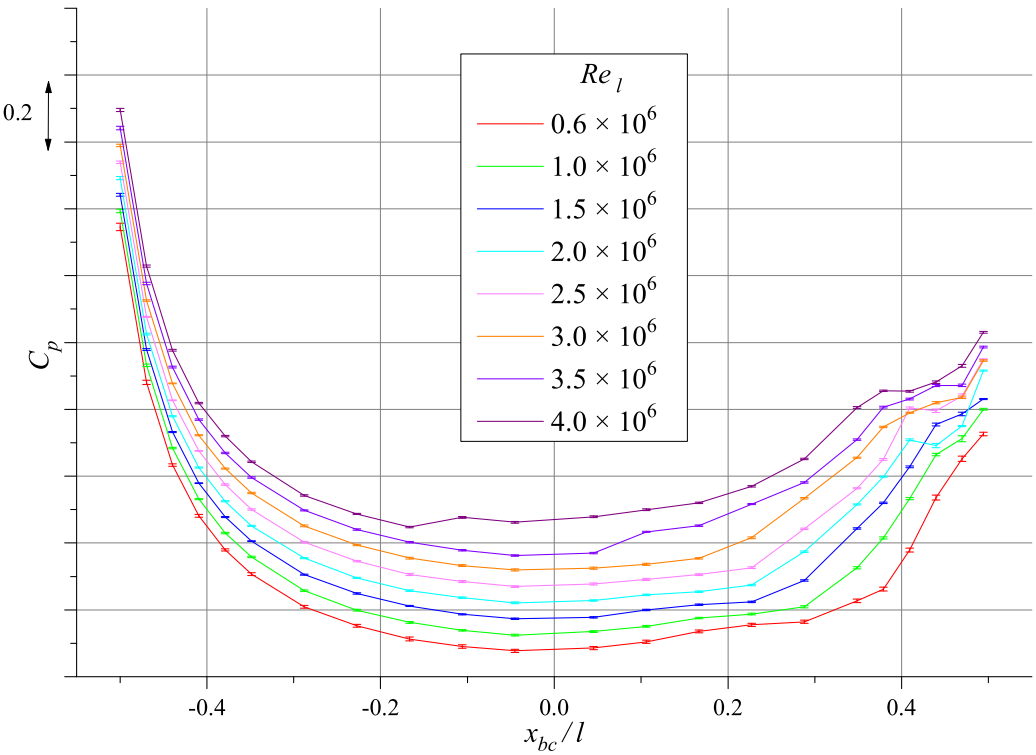

Figure 5.3: Ellipsoid surface pressure measurements with $\pm 3\sigma_{\bar{C}_{P_i}}$ error bars, $\alpha = -6.2°$

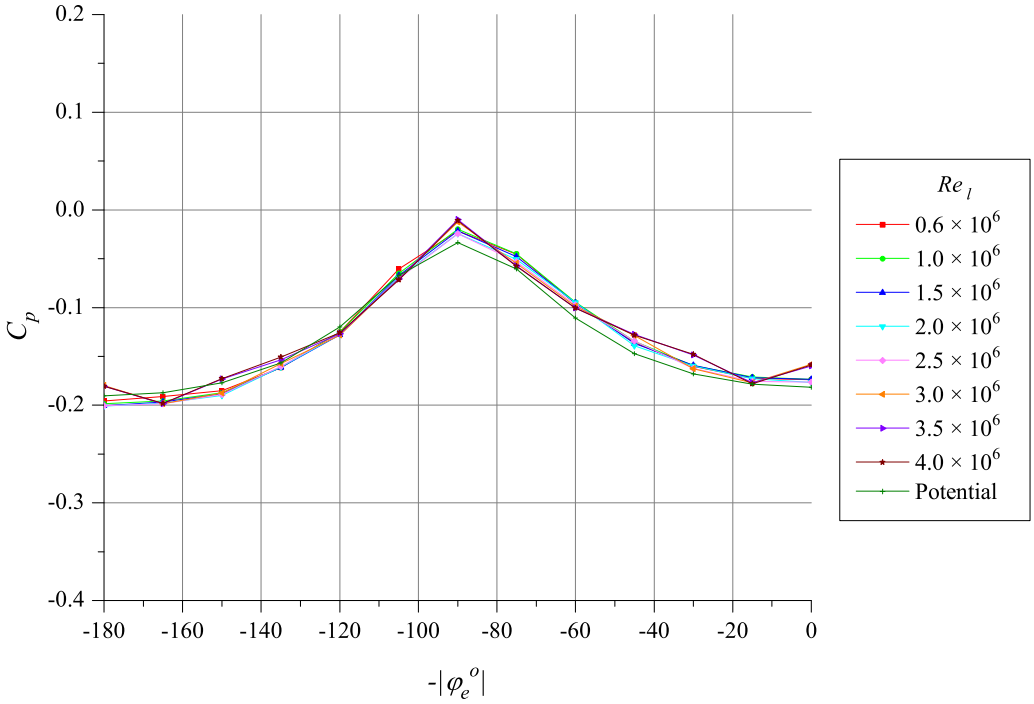

Figure 5.4: Surface pressure around front of ellipsoid, $\alpha = -0.2°$, $x_{bc}/l = -0.348$

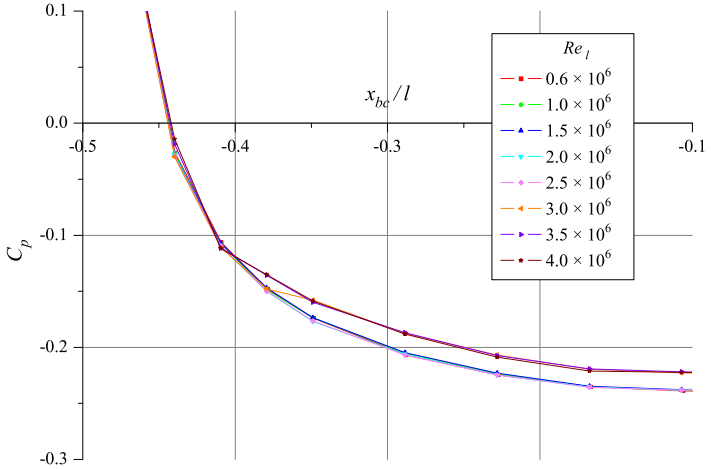

(a) $-|\varphi_e| = 0°$

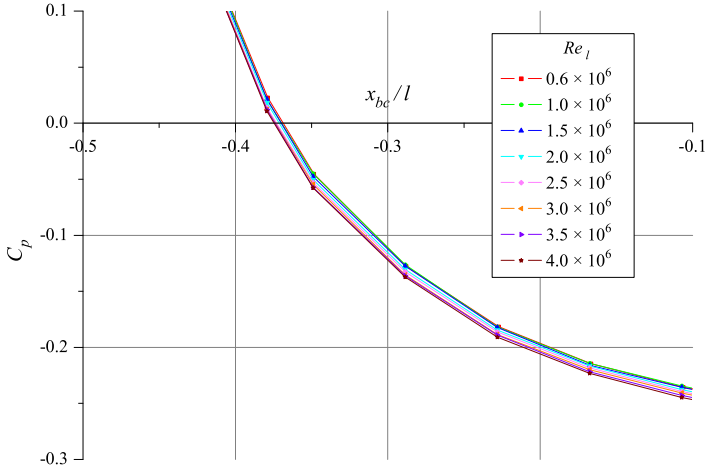

(b) $-|\varphi_e| = -75°$

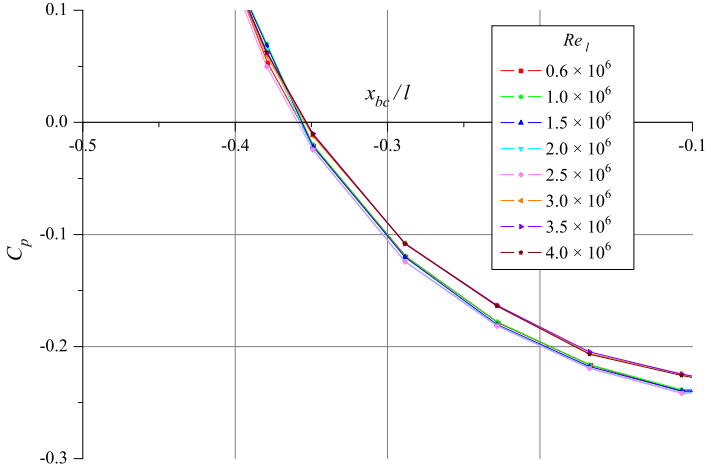

(c) $-|\varphi_e| = -90°$

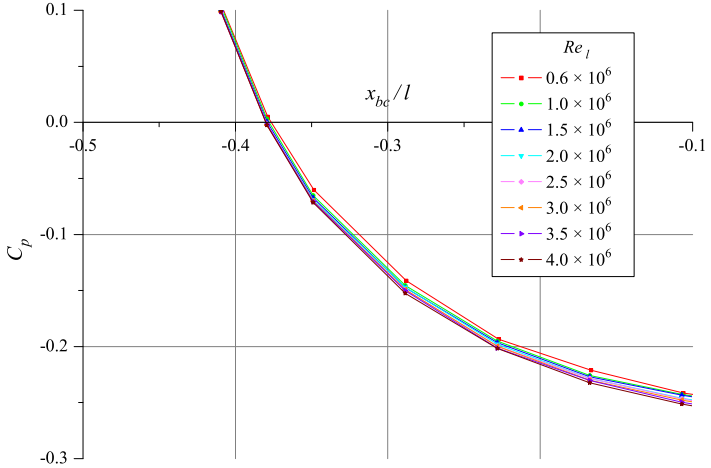

(d) $-|\varphi_e| = -105°$

Figure 5.5: Effect of azimuthal pressure gradients on surface pressure at $\alpha = -0.2°$

The characteristic changes in surface pressure associated with a laminar separation bubble and boundary layer transition described in 4.4.2 are also seen in these results. A separation bubble is apparent at the lowest Reynolds number over the rear of the model near $x_{bc}/l \approx 0.36$ for $\varphi_e = -15°$ and $-30°$; a larger separation bubble exists between $-120°$ and $-165°$. The separation on the underside is present to a lesser extent at the next largest Reynolds number. As seen with the 3-1 spheroid, the surface pressure curves for the higher Reynolds numbers in regions of adverse pressure gradient show the perturbation associated with boundary layer transition upstream of those for the lower Reynolds numbers. The curves for higher Reynolds numbers in this range leave the grouping of the other curves in this range, but do not tend to join the curves in the higher Re_l range (3.0×10^6 to 4.0×10^6); they form a new grouping of curves as seen in Fig. 5.6. An obvious explanation for this is the significantly earlier flow separation displayed by the curves in the higher Reynolds number range.

Another notable feature is the more rapid pressure increase at the rear of the model for $\varphi_e = 0°$ than at $-180°$, whereas, for the higher Re_l (2.5×10^6) the curves are very close (see Fig. 5.1). The curves over the rear half of the model for the adjacent azimuthal angles of $-15°$ and $-165°$ are almost identical over the full range of Reynolds numbers.

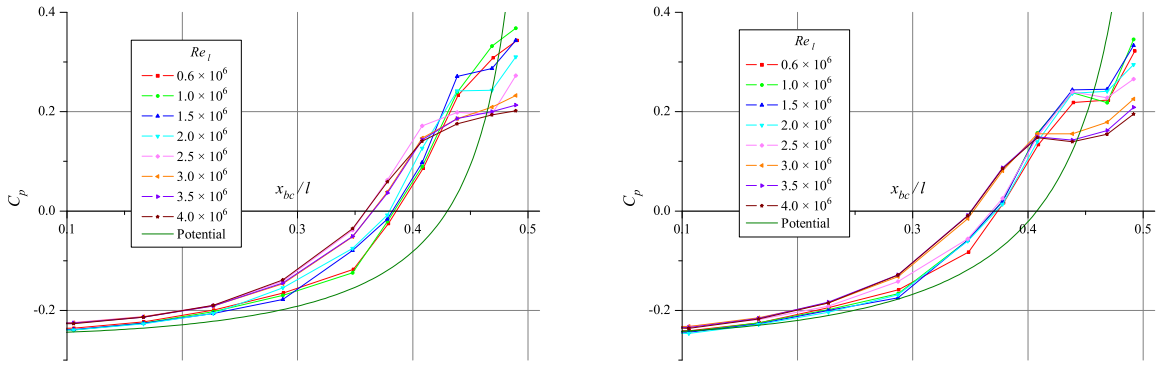

(a) $-|\varphi_e| = -45°$ (b) $-|\varphi_e| = -60°$

Figure 5.6: Early separation of higher Reynolds number flow at $\alpha = -0.2°$

Over the rear of the model, except for φ_e between $-75°$ and $-105°$, the results for the measured surface pressure are greater than those calculated using potential theory. The deviation from the potential curve begins near the start of the adverse pressure gradient region. The gap between the measured values and the potential curve increases as the rear of the model is approached. (An exception occurs at the lower Reynolds numbers where a separation bubble exists.) Near the horizontal plane the curves sit close to the potential curve. Given the different behaviour in comparison to the potential curve in these regions, the presence of a vortical flow feature in one or both of these regions is suspected. The existence of such a flow feature is demonstrated by the flow visualisation (Fig. 5.7). The region of the model where the large

vortical structures are shown, centred at $x_{bc}/l \approx 0.45$ and $\varphi_e \approx -145°$, corresponds to the area where the pressure has increased.

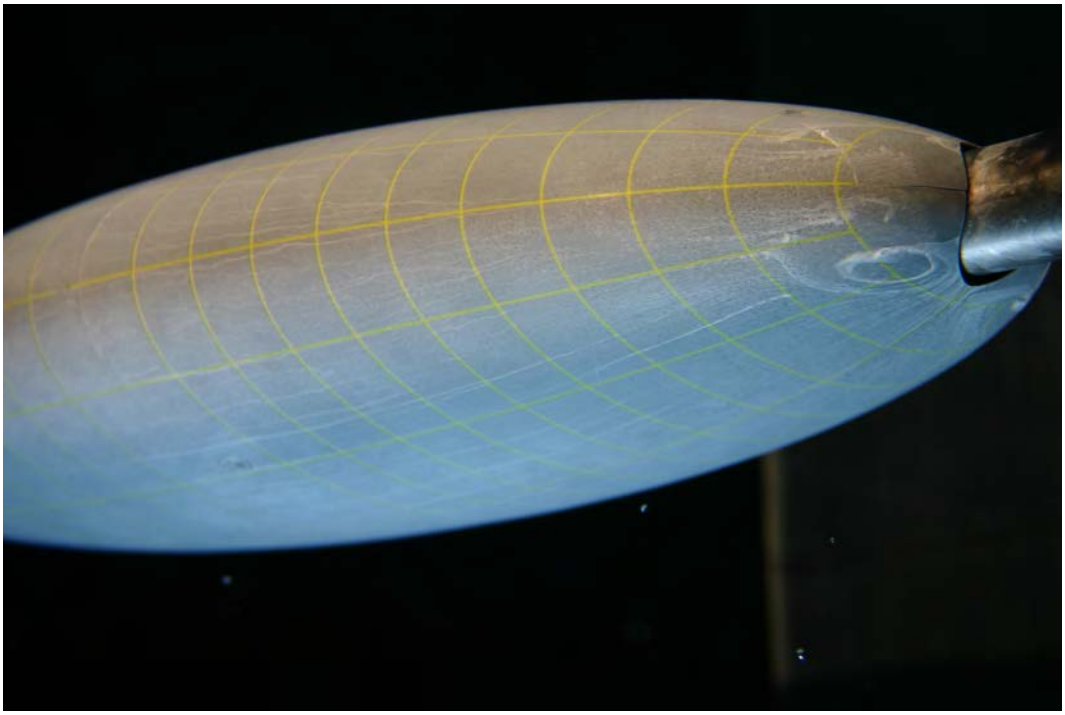

Figure 5.7: Surface flow visualisation at rear of ellipsoid, $\alpha = -0.2°$, $Re_l = 2.5 \times 10^6$

Reynolds Numbers 3.0×10^6 to 4.0×10^6

Fig. 5.5 shows that the flow has undergone laminar-turbulent transition near the nose for these Reynolds numbers on horizontal plane, but has not transitioned for the adjacent azimuthal angles in the streamwise range shown by this figure. The measurements in the vertical plane show that boundary layer transition occurs near the nose for Re_l in this range. At $\varphi_e = -15°$ and $-165°$ the results for 3.0×10^6 no longer show transition near the nose. As φ_e approaches the horizontal plane the location of boundary layer transition for the two largest Reynolds numbers gradually moves rearward until at $-75°$ and $-105°$ transition is not seen to occur until the rear half of the model ($x_{bc}/l \approx 0.17$) as noted at the start of this paragraph. The measurements at the rear of the model display a significant separation starting at $x_{bc}/l \approx 0.4$ at $\varphi_e = -90°$. The separation line moves a little rearward as the vertical plane is approached. The pressure recovery for the Reynolds number in this range is significantly less than at lower Reynolds numbers (Fig. 5.6).

5.2.2 Ellipsoid at $\alpha = -6.2°$

On the pressure side the minimum pressure is significantly less than predicted by the potential calculations and occurs upstream of the predicted point. On the vertical symmetry plane, where this difference is at its greatest for $Re_l = 2.5 \times 10^6$, the minimum C_p of -0.25 occurs at $x_{bc}/l \approx 0.16$; the potential calculations determine a minimum C_p of -0.31 at $x_{bc}/l \approx 0.36$. The difference is greater for lower Reynolds numbers, where a laminar separation occurs, and for larger Reynolds numbers where the boundary layer is turbulent.

The base pressure values for the range of Reynolds numbers tested are clustered in two groups. When boundary layer transition occurs on the pressure side well before the end of the model, the base C_p decreases from approximately 0.25 to 0.23 as Re_l increases from 3.0×10^6 to 4.0×10^6. When the boundary layer transition occurs near the end of the model, the base C_p decreases from 0.35 to 0.29 as Re_l increases from 1.0×10^6 to 2.5×10^6.

Reynolds Numbers 0.6×10^6 to 2.5×10^6

Over the front of the model for φ_e between 0° and −75° the surface pressure curves are closely grouped. Where strong azimuthal pressure gradients are present, for φ_e between −75° and −105°, a spread in surface pressure exists as seen in similar circumstances on previous tests (Fig. 5.8(b) and (c)). This spread is most apparent in extended regions of favourable streamwise pressure gradient. At φ_e equal to −120°, even though a strong azimuthal pressure gradient is present upstream of $x_{bc}/l \approx -0.35$, the lack of extended favourable pressure gradient in the streamwise direction appears to minimise the spread in the measurements (Fig. 5.8(d)).

Over the front half of the model for φ_e between 0° and −75° the measured surface pressure curves are close to the values calculated using classical potential theory. For φ_e between −75° and −180° the measured values are noticeably smaller.

At the lower Reynolds numbers the surface pressure measurements indicate two regions on the rear of the body between $\varphi_e = 0°$ and −135° have separated flow. At the lowest Reynolds number a laminar separation bubble is present at the rear of the model on the pressure side. It is visible at 0° and −15° with the maximum near −30° starting at $x_{bc}/l \approx 0.35$ (Fig. 5.9(a)). At the adjacent azimuthal angle, −45°, the separation bubble is small for the lowest Reynolds number and not apparent for larger values. A significant separation centred on $\varphi_e = -105°$ starts near $x_{bc}/l \approx 0.05$ for $Re_l \leqslant 1.5 \times 10^6$ and extends downstream to $x_{bc}/l \approx 0.23$ in the case of the lower two Reynolds numbers (Fig. 5.9(b)); for these Reynolds numbers it is visible at the adjacent azimuthal angles.

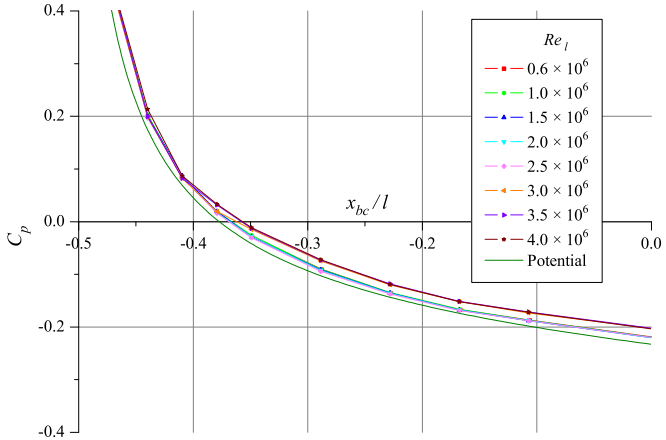

(a) Extended favourable streamwise pressure gradient, no azimuthal pressure gradient, $-|\varphi_e| = 0°$

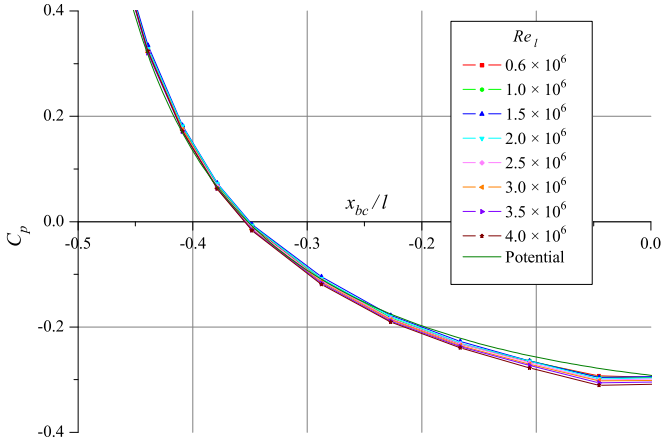

(b) Extended favourable streamwise pressure gradient, strong azimuthal pressure gradient, $-|\varphi_e| = -75°$

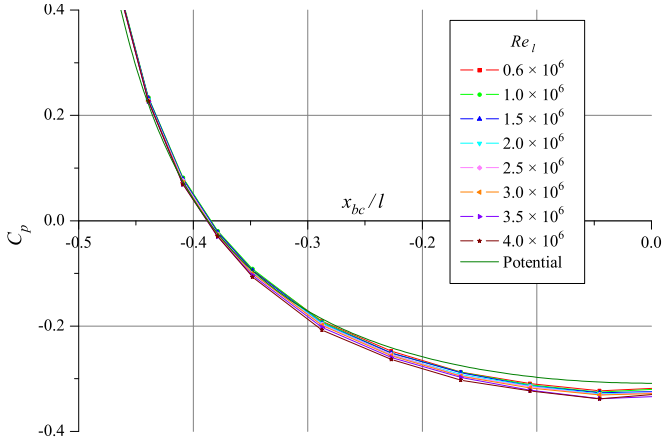

(c) Extended favourable streamwise pressure gradient, strong azimuthal pressure gradient, $-|\varphi_e| = -90°$

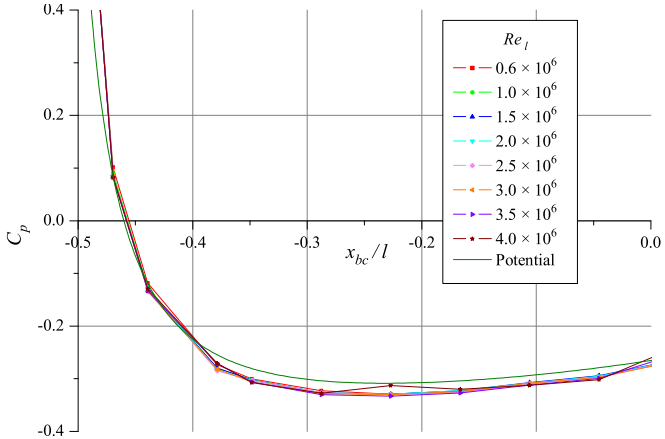

(d) Short favourable streamwise pressure gradient, strong azimuthal pressure gradient, $-|\varphi_e| = -120°$

Figure 5.8: Comparison of surface pressure in regions of favourable pressure gradient with varying azimuthal pressure gradient, $\alpha = -6.2°$

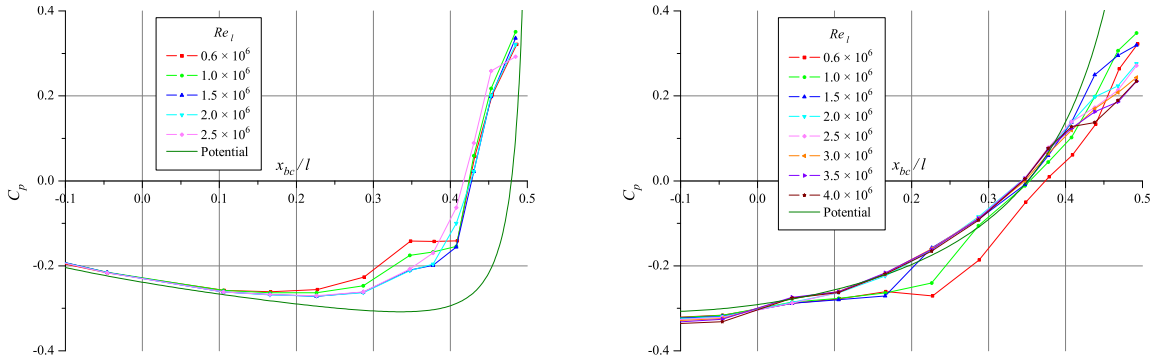

(a) $-|\varphi_e| = -30°$ (b) $-|\varphi_e| = -105°$

Figure 5.9: Separation bubbles on ellipsoid at $\alpha = -6.2°$

On the suction side ($-120° \geqslant \varphi_e \geqslant -180°$) the flow appears to stay attached until at least $x_{bc}/l \approx 0.43$. The pressure is considerably lower than predicted by the potential calculation over the rear half of the suction side until boundary layer transition occurs. With considerable length of adverse pressure gradient it is noteworthy that the flow has stayed attached, as was the case with the spheroid at incidence. An unusual flat, or at least flattening in the surface pressure curves, occurs near the centre of the body as seen in Fig. 5.10. When this occurs on the suction side it may be tempting to call these laminar separations, but that explanation is rejected as the low Reynolds number flows are still laminar after the flat. (It could possibly be one laminar flow forcing another off the surface, but at $\varphi_e = -165°$ minimal cross flow is expected.) It is also possible that there is an error in measurement, yet the curves on either side of the flat are consistent and in at least one case ($\varphi_e = -120°$) one of these flats occurs for the lowest Reynolds numbers further downstream than usual; but all the measurements for the higher Reynolds numbers appear reasonable at this location. The presence of a physical disturbance is also unlikely as there is no tendency for boundary layer transition to occur at this point, or for the flows with the thinner boundary layers to exhibit a greater disturbance. For $\varphi_e = -165°$ this flat occurs in the curves regardless of whether boundary layer transition has occurred prior to the flat or not, except at $Re_l = 2.0 \times 10^6$. For $Re_l = 2.0 \times 10^6$, where boundary layer transition occurs upstream of the location where the curves for the other Reynolds numbers display a flat, no flat in the curve is apparent. At $\varphi_e = -135°$ a flattening occurs in the surface pressure curves for $Re_l \leqslant 2.0 \times 10^6$ that are yet to undergo boundary layer transition and at $Re_l = 4.0 \times 10^6$ for which boundary layer transition occurred near the nose. Boundary layer transition is occurring near this location for $Re_l = 2.5 \times 10^6$ and $Re_l = 3.0 \times 10^6$ so any flattening in the curve is difficult to isolate; for $Re_l = 3.5 \times 10^6$ where transition has occurred just prior to $x_{bc}/l = 0$ for this and adjacent azimuths there is less flattening than at

$Re_l = 4.0 \times 10^6$. Metrology performed on this model before and after the testing showed no problems with the surface shape.

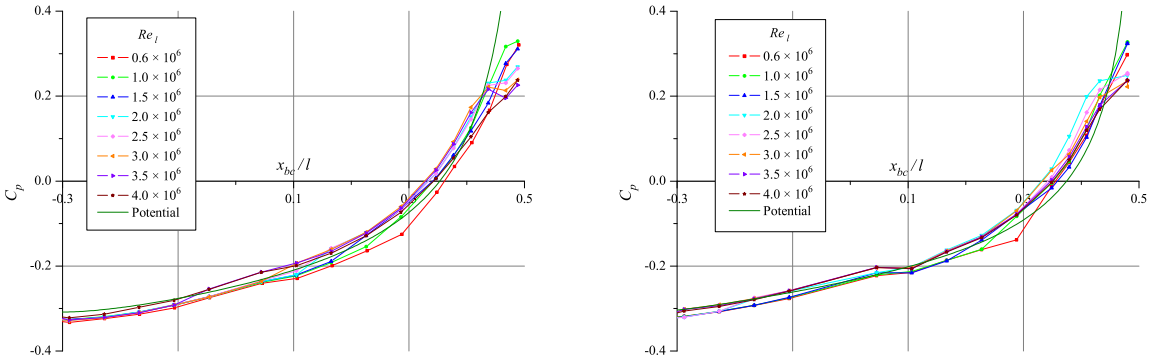

(a) $-|\varphi_e| = -135°$ (b) $-|\varphi_e| = -165°$

Figure 5.10: Flats on suction side pressure curves, $\alpha = -6.2$

Reynolds Numbers 3.0×10^6 to 4.0×10^6

The measurements at $\varphi_e = -30°$ and $-150°$ were discarded due to a surface irregularity at one of the taps compromising the measurements for this range of Reynolds numbers.

On the pressure side for $0 \geqslant \varphi_e \geqslant -30°$ the location of the transition is similar to those that for $-0.2°$ incidence. At $\varphi_e = -45°$ the boundary layer transition location has moved downstream of the corresponding point for the same Reynolds number at $\alpha = -0.2°$, suggesting that the favourable pressure gradient, and/or greater crossflow occurring at an increased angle of incidence, has provided a stabilising influence on the boundary layer. The boundary layer transition line moves downstream as φ_e approaches $-75°$ from $-45°$. Between $-75°$ and $-105°$ the transition for $Re_l = 4.0 \times 10^6$ occurs near $x_{bc}/l = 0$. For the two low Reynolds numbers in this range at $\varphi_e = -90°$ the laminar-turbulent transition has moved downstream to $x_{bc}/l \approx 0.17$. This transition line stays close to the middle of the body for Reynolds numbers in this range for $\varphi_e = -120°$ and $-135°$. For $\varphi_e = -165°$ and $-180°$ laminar-turbulent transition for these Reynolds numbers occurs soon after the adverse pressure gradient starts near $x_{bc}/l = -0.3$.

At the rear of the model for φ_e between $0°$ and $-30°$ the pressure over the later part of the model increases significantly before the pressure increase at lower Reynolds numbers. The overall pressure recovery before separation is less. These two flow regimes are apparent in Fig. 5.11(a). At $\varphi_e = -45°$, except for the earlier separation of the higher Reynolds number flows, the surface pressure measurements do not exhibit significant differences over the majority of this azimuth. The increase in pressure for the lower Reynolds numbers has moved upstream (Fig. 5.11(b)).

On the suction side there tends to be a smaller difference between the curves for the transitioned lower Reynolds number flows and the curves for the Reynolds number in this range up until the point where boundary layer separation occurs. The boundary layer on the suction side separates earlier for the Reynolds numbers in this range. The early separation on the pressure side of the body is probably producing an earlier separation on the suction side.

The final on-body measurement location shows a reversal in surface pressure at $\varphi_e \approx -120°$. This reversal is no longer seen for $\varphi_e = -165°$ and $-180°$ where the surface curvature is greatly reduced and the flow remains attached.

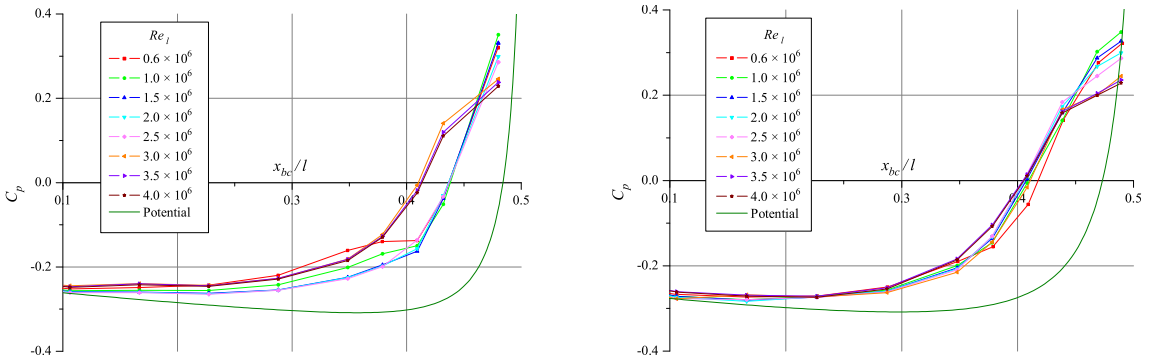

(a) Segregation of surface pressure distributions for low and high Reynolds numbers, $-|\varphi_e| = -15°$

(b) Early flow separation of higher Reynolds number flow, $-|\varphi_e| = -45°$

Figure 5.11: Early pressure side flow separation of higher Reynolds number flow, $\alpha = -6.2°$

5.2.3 Ellipsoid at $\alpha = -10.2°$

At $\alpha = -10.2°$ the characteristics of the surface pressure measurements displayed similar characteristics to those at $-6.2°$ incidence. Notably:

- the minimum measured surface pressure was greater, and located upstream of the predicted minimum using potential theory.
- the base pressure for the three largest Reynolds numbers was less than that for smaller Reynolds numbers.

Reynolds Numbers 0.6×10^6 to 2.5×10^6

Over the front half of the model at $\varphi_e = 0°$ the measured surface pressure is marginally greater than that calculated using potential theory. As φ_e decreases, the measured surface pressure decreases in comparison to the potential calculation; at φ_e around $-45°$ the values for the measured and potential pressure are similar over the front half of the model. For φ_e between $-75°$ and $-180°$ the measured surface pressure over the front half of the model is noticeably less

than the values calculated from potential theory. Fig. 5.12 shows the spread in the measured curves is again observed in regions of combined favourable streamwise pressure gradients and azimuthal pressure gradients.

These measurements show a discontinuity near the centre of the model for $\varphi_e = -90°$, $-105°$ and $-120°$ across all Reynolds numbers in this range (Fig. 5.14(c)). A large separation exists for the lowest two Reynolds numbers, centred at $\varphi_e = -105°$ and starting at $x_{bc}/l \approx 0.05$; the reattachment, if any, is not apparent. At $\varphi_e = -120°$ this separation has moved upstream to $x_{bc}/l \approx -0.05$. For the larger Reynolds numbers in this range the length of separated flow is relatively short. On-surface flow visualisation makes the flow structure of the separation more apparent (Fig. 5.13) although as noted in Subsection 7.3.2 and Section 10.2 the upstream extent of the separation at $Re_l = 2.0 \times 10^6$ is difficult to determine.

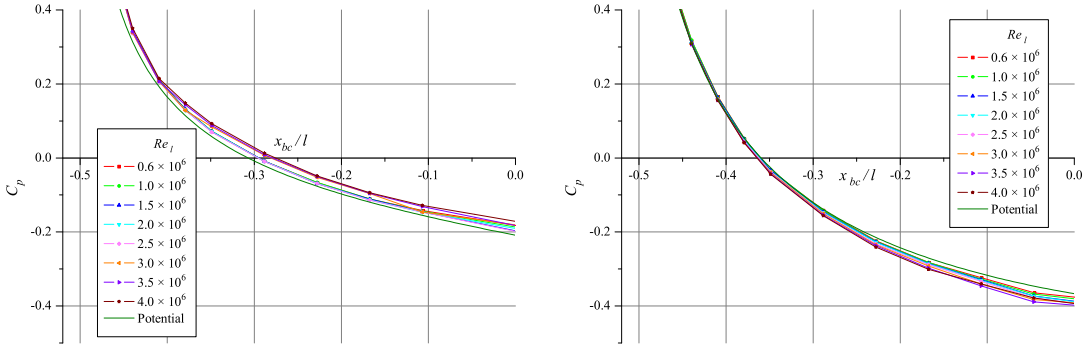

(a) Extended favourable streamwise pressure gradient, no azimuthal pressure gradient, $-|\varphi_e| = 0°$

(b) Extended favourable streamwise pressure gradient, strong azimuthal pressure gradient, $-|\varphi_e| = -75°$

Figure 5.12: Spread of surface pressure curves in presence of extended favourable streamwise pressure gradient and strong azimuthal pressure gradient

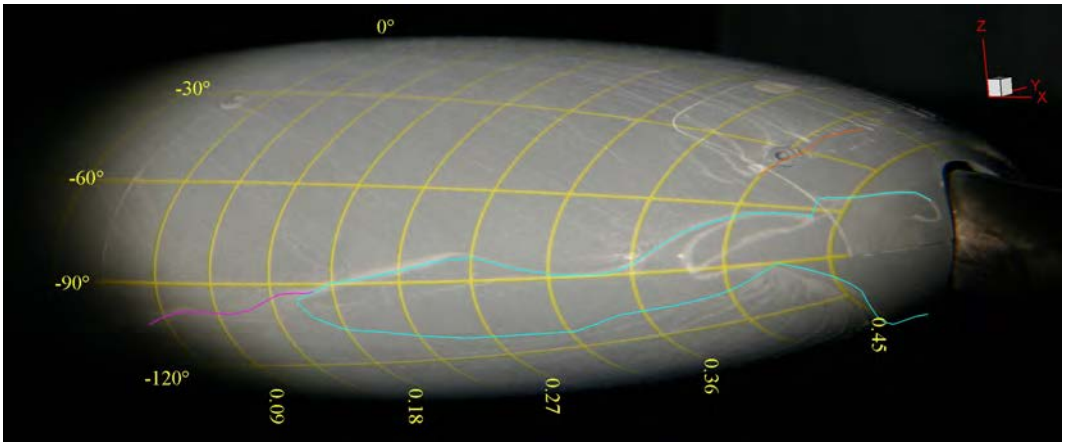

Figure 5.13: Surface flow visualisation at rear of ellipsoid, $\alpha = -10.2°$, $Re_l = 2.0 \times 10^6$ (cyan line - limiting surface streamline, magenta line - limiting surface streamline in early photos in sequence, orange line - location of short separation bubble)

As was the case at $-6.2°$ incidence for φ_e between $0°$ and $-30°$, the lowest three Reynolds number flows appear to separate just prior to the end of the body. For $Re_l = 2.0 \times 10^6$ and 2.5×10^6 the flow appears to stay attached at least until the most downstream surface tap, remembering that the last measurement is the base pressure (Fig. 5.14(a)). At $\varphi_e = -45°$ there is close grouping of curves for flows that do not have a laminar separation near the base (Fig. 5.14(b)); this grouping spreads at $\varphi_e = -60°$ and $-75°$. Near the base, the curves for $-90°$ to $-120°$ display a number of discontinuities which are probably due to structures similar to those seen in Fig. 5.13.

The curves for φ_e between $-135°$ and $-180°$ show that, with the exception of the lowest Reynolds number, the boundary layer has transitioned before or near the start of the rear half of the model, the flow appears to stay attached until the last on-body measurement point (Fig. 5.14(d)). The curve for the lowest Reynolds number in this range is separate from the other curves; a small positive deviation just prior to $x_{bc}/l = 0.2$ may be associated with boundary layer transition. This curve may not group with the other curves due to the large laminar separation bubble that occurs on the pressure side for this Reynolds number.

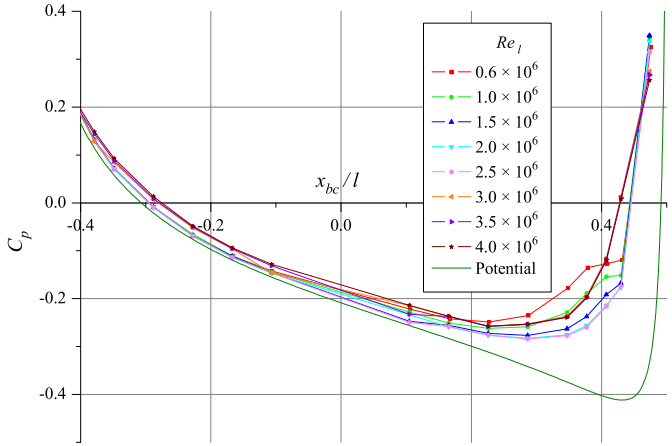

(a) $-|\varphi_e| = 0°$. Largest Reynolds numbers exhibit an increase in pressure upstream and lower base pressure

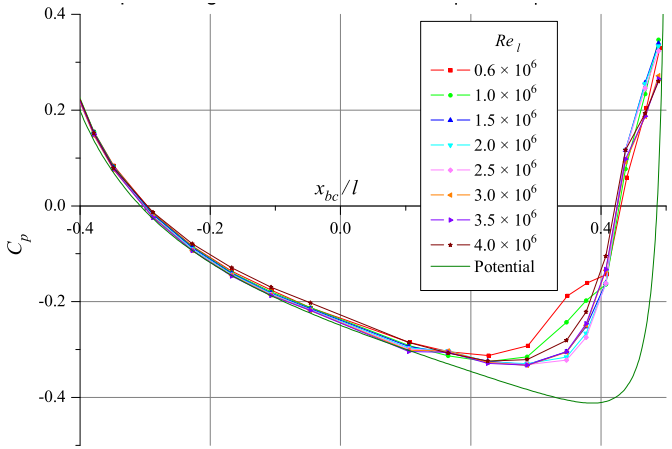

(b) $-|\varphi_e| = -45°$. Lack of flow separation and close grouping of curves for all but the lowest Reynolds numbers

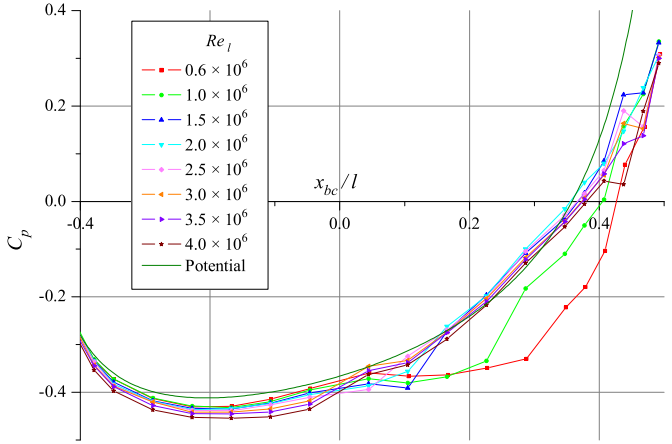

(c) $-|\varphi_e| = -105°$. Flow separation and discontinuity on side of model

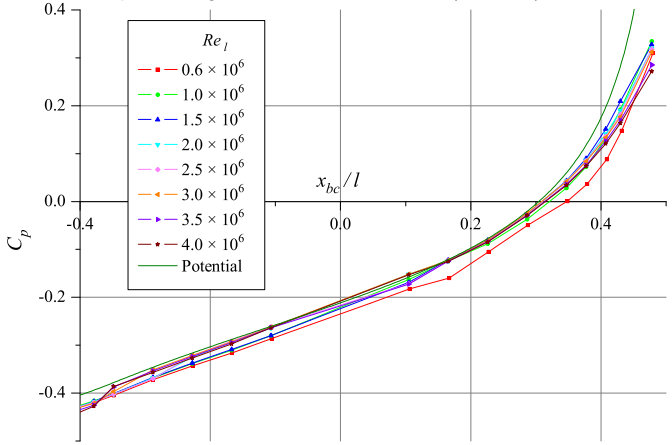

(d) $-|\varphi_e| = -165°$. Flow attachment despite extended adverse pressure gradient on suction side of model

Figure 5.14: Surface pressure features for ellipsoid, $\alpha = -10.2°$

Reynolds Numbers 3.0×10^6 to 4.0×10^6

Separation is apparent near the front of the model near $x_{bc}/l = -0.36$ at $\varphi_e = -120°$ and $-135°$ for $Re_l = 3.5 \times 10^6$ and 4.0×10^6 (Fig. 5.16). Downstream of this separation the surface pressure distributions for these Reynolds numbers at $\varphi_e = -120°$ and $-135°$ are again grouped for a short distance with those for the lower Reynolds number flows which have not transitioned. An explanation for this observation is that laminar flow from the pressure side has crossed the $\varphi_e = -120°$ and 135° azimuths. For this explanation to be reasonable the laminar flow has to come past $\varphi_e = -120°$ to $-135°$, yet the length of laminar flow after the apparent separation at $-120°$ is less than at $-135°$. At this point of the analysis it is important to remember that the measurements were actually taken at $\varphi_e = -120°$ and 135°, on opposite sides of the vertical plane. Hence the observation in the previous sentence may be explained by the flow not being perfectly symmetrical. Although no flow visualisation was performed at the front of the model for these Reynolds numbers, visualisation at $Re_l = 2.5 \times 10^6$ shows significant crossflow (Fig. 5.15) at the front of the model at the relevant location, suggesting that this explanation may be correct. The results for $Re_l = 3.0 \times 10^6$ suggest that the flow stays attached over the front half of the model. Another possible explanation for this observation is that a change in flow conditions occurred over the time of measuring the tappings on this section of the body. This explanation is believed to be the least likely as this behaviour appears relatively consistent for two different Reynolds numbers and two different azimuths.

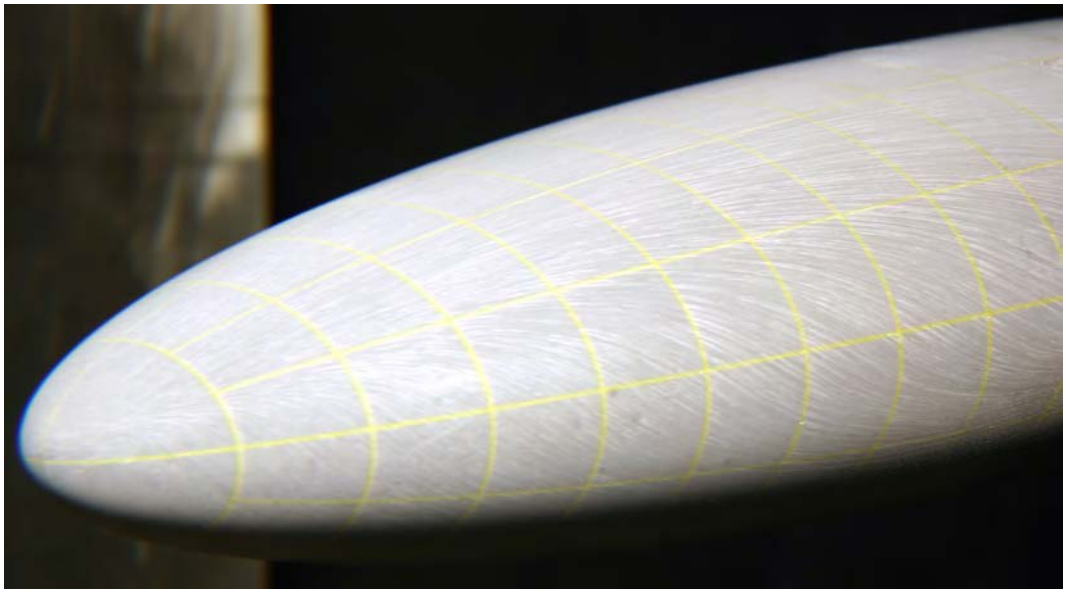

Figure 5.15: Surface flow visualisation at front of ellipsoid, $\alpha = -10.2°$, $Re_l = 2.5 \times 10^6$

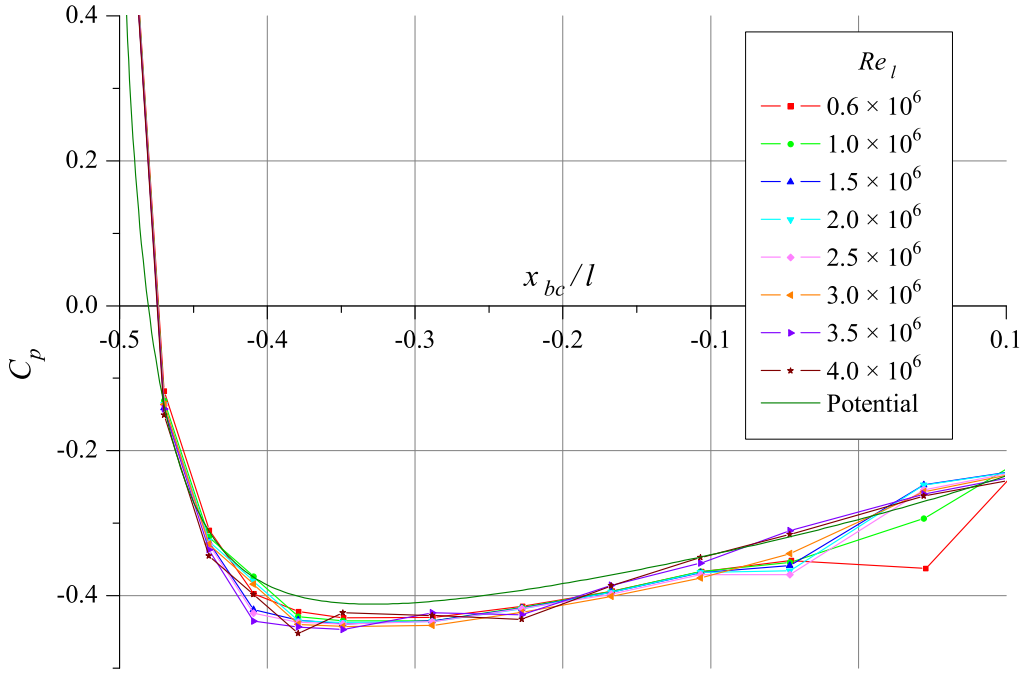

(a) $-|\varphi_e| = -120°$

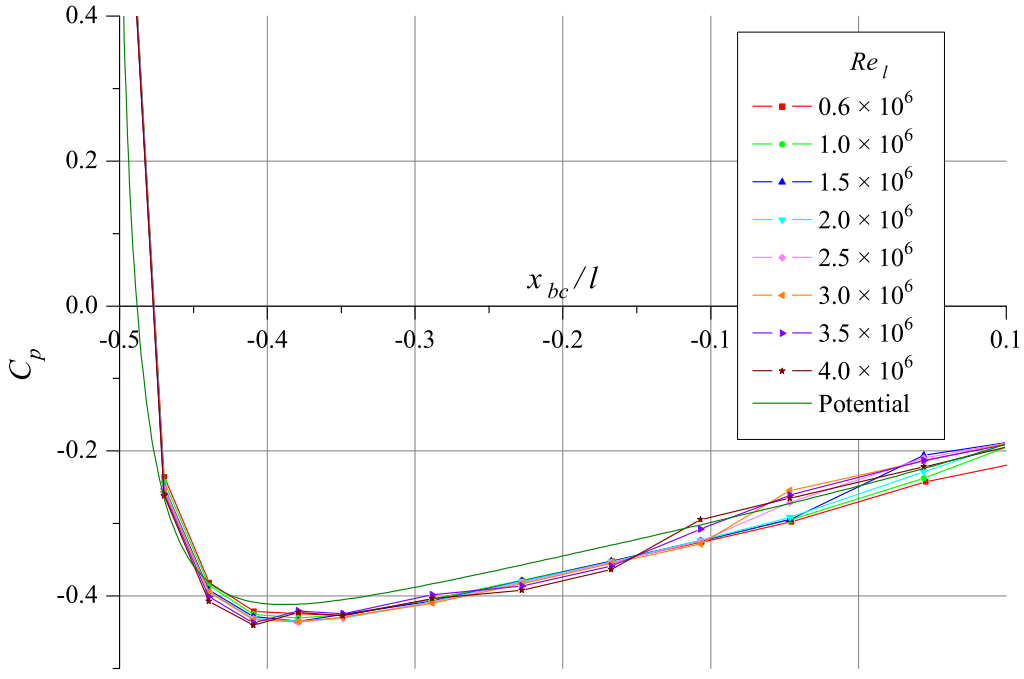

(b) $-|\varphi_e| = -135°$

Figure 5.16: Measured surface pressure on the suction side over the front of the ellipsoid, $\alpha = -10.2°$

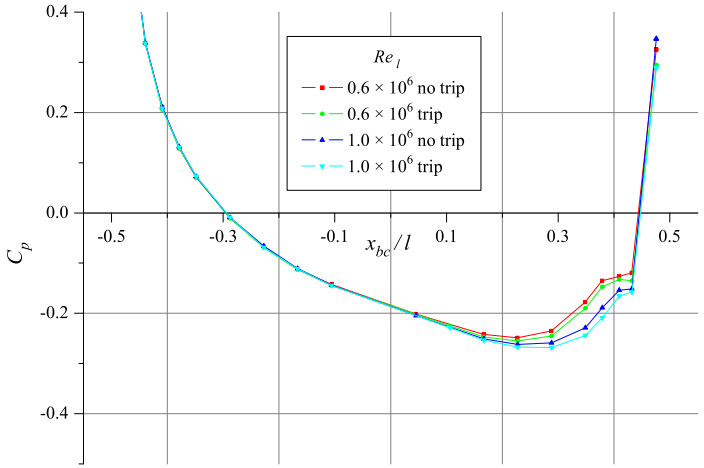

(a) $-|\varphi_e| = 0°$

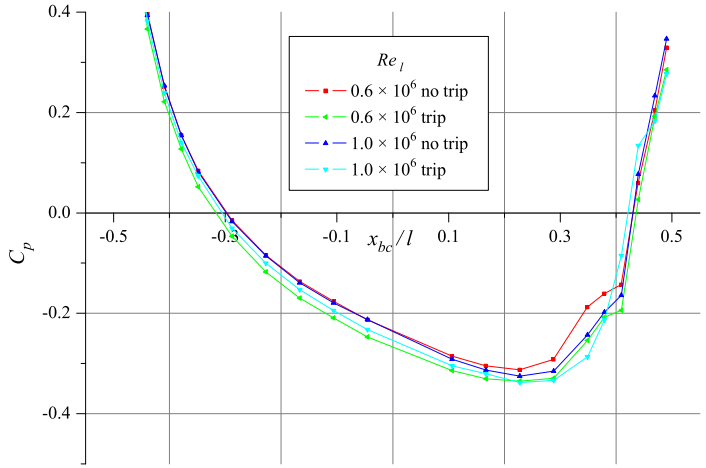

(b) $-|\varphi_e| = -45°$

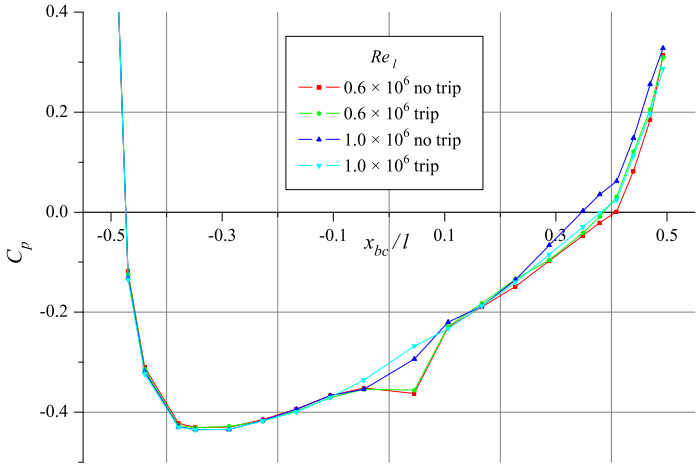

(c) $-|\varphi_e| = -120°$

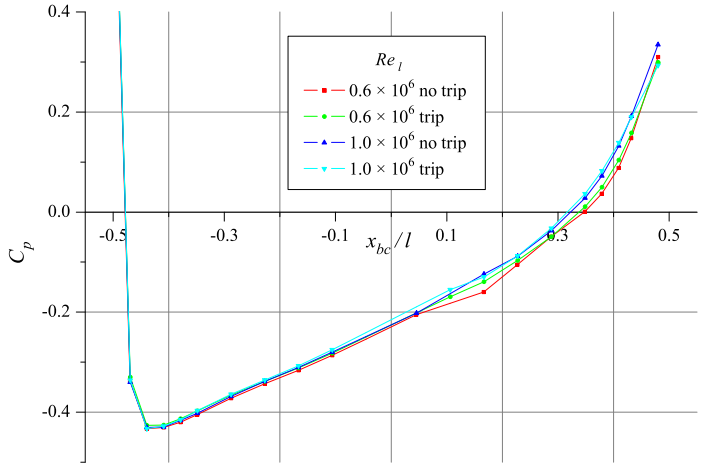

(d) $-|\varphi_e| = -165°$

Figure 5.17: Comparison of Surface Pressure on a 4.2–2–1 ellipsoid at $\alpha = -10.2°$ with unforced and forced boundary layer transition at low Reynolds number

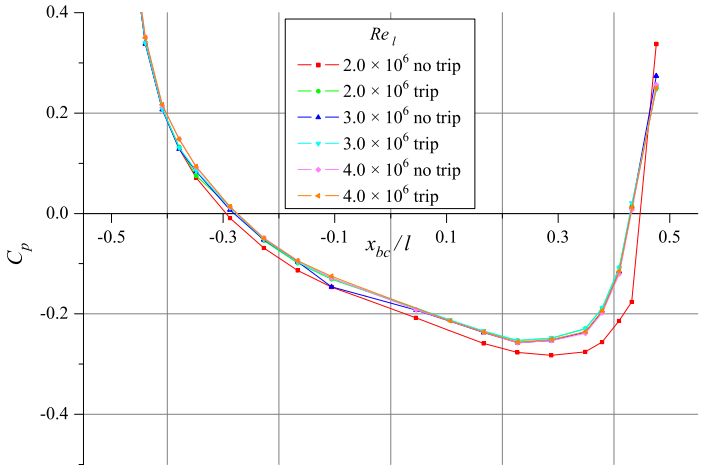

(a) $-|\varphi_e| = 0°$

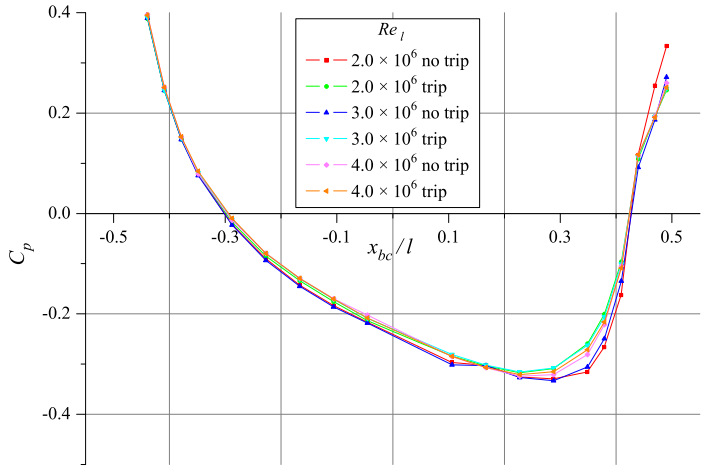

(b) $-|\varphi_e| = -45°$

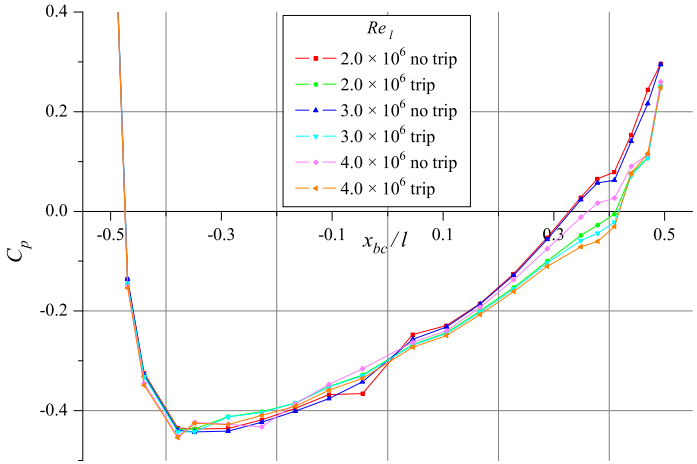

(c) $-|\varphi_e| = -120°$

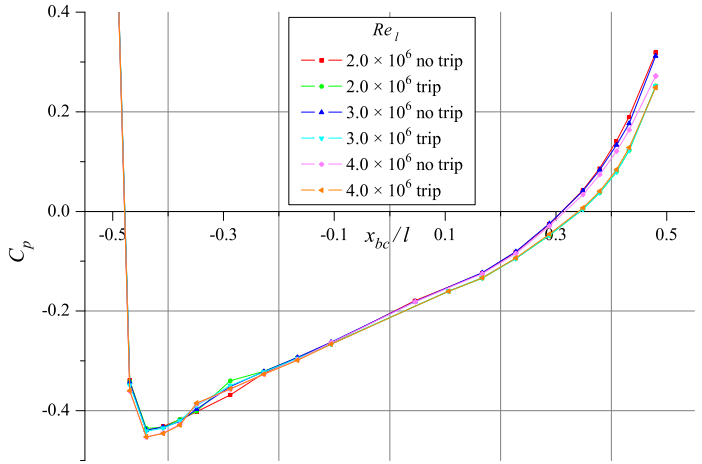

(d) $-|\varphi_e| = -165°$

Figure 5.18: Comparison of surface pressure on a 4.2–2–1 ellipsoid at $\alpha = -10.2°$ with unforced and forced boundary layer transition at high Reynolds number

5.2.4 Ellipsoid at $\alpha = -10.2°$, Boundary Layer Tripped at 20% of Total Length

The position, size and geometry of the boundary layer trip for the ellipsoid was identical to that used with the spheroid. The trip strip stimulated the creation of a turbulent boundary layer for $Re_l \gtrapprox 1.3 \times 10^6$.

Reynolds Numbers 0.6×10^6 to 1.0×10^6

As expected, the surface pressure distributions for these Reynolds numbers are very close to those for the flow without the trip strip. The match over the front of the model is closer than at the rear.

Reynolds Numbers 1.5×10^6 to 4.0×10^6

At the maximum Reynolds numbers tested at this incidence with no trip strip the boundary layer did not transition at the front of the model for $\varphi_e = -60°$. Hence the results for the tripped flow are not expected to match exactly the results for the maximum Reynolds number with unforced transition. With the tripped boundary layer the flow for this range of Reynolds number appears almost independent of Reynolds number, except for a minor variation at the rear of the model near $\varphi_e = -120°$.

Subsection 5.2.3 identified a region of flow near the nose at $\varphi_e = -120°$ and $-135°$ for the highest Reynolds numbers where there appeared to be a region of separated flow along an azimuth followed by attached turbulent flow. The curves for these Reynolds numbers shortly rejoined those of lower Reynolds numbers that had not transitioned, indicating that the flow was now laminar; the explanation that flow across the azimuths was providing the path for the laminar flow to reappear on the azimuth was provided. For the tripped boundary layer the flow had transitioned at one streamwise location, so the reappearance of laminar flow on an azimuth should not occur due to flow across the azimuths (without relaminarisation). Fig. 5.19 provides a comparison of the results for the model with unforced and forced transition. The results are consistent with the explanation given in Subsection 5.2.3, as no laminar section is now seen with the forced transition.

The base pressure values when the trip strip is effective are clearly separated from the base pressure for the two lowest Reynolds numbers flows (Fig. 5.20).

The results on the pressure side at $\varphi_e = -15°$ show a close match between the results for the maximum Reynolds number with the unforced transitioning boundary layer and those with forced transition. The results for the lowest Reynolds number with the ineffective trip and no

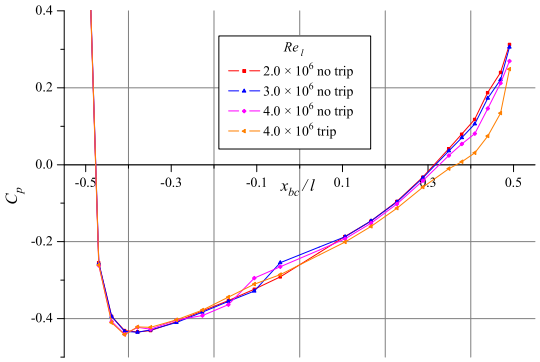

Figure 5.19: Surface pressure around front of ellipsoid, $\alpha = -10.2°$, $-|\varphi_e| = -135°$

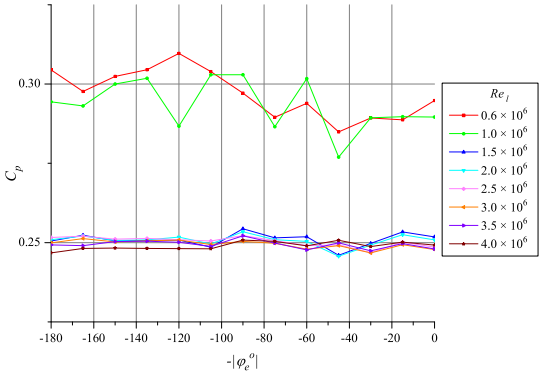

Figure 5.20: Base pressure of ellipsoid with trip strip, $\alpha = -10.2°$

trip strip are again a close match (Fig. 5.21(a)).

Fig. 5.21(b) shows that the discontinuity in the surface pressure curve associated with the large structure centred near $\varphi_e = -105°$ at $x_{bc}/l \approx -0.4$ has moved upstream and is longer than was the case with unforced transition at the maximum Reynolds number. The comparison at the lowest Reynolds numbers were the trip strip is ineffective shows a close match. The results for the tripped flow show no obvious dependency for these Reynolds numbers at this azimuth.

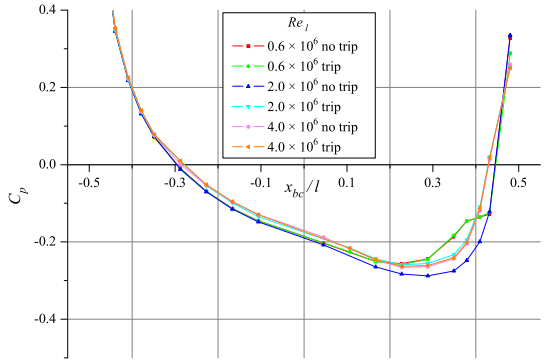

(a) $-|\varphi_e| = -15°$

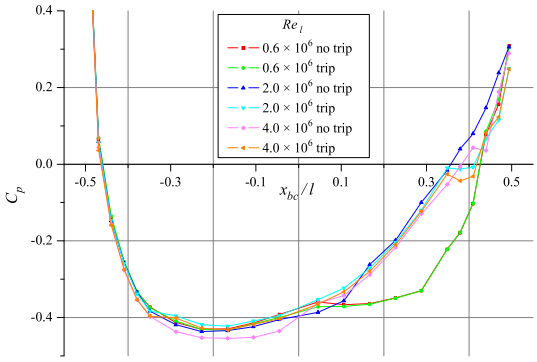

(b) $-|\varphi_e| = -105°$

Figure 5.21: Comparison of surface pressure on a 4.2–2–1 ellipsoid at $-10.2°$ with unforced and forced boundary layer transition

5.3 Summary

Surface pressure characteristics associated with boundary layer thickening, laminar separation bubbles, transition and separation as earlier identified for the spheroid were also present on the ellipsoid.

Under particular described conditions in this and the previous chapter a small spread in

the surface pressure curves with Reynolds number has been noted. This feature occurred in regions of laminar boundary layer with strong azimuthal pressure gradients in extended regions of favourable or only slightly adverse streamwise pressure gradients.

A possible explanation for this spread may be found by considering the influence of the azimuthal pressure gradient on the boundary layer fluid. Over the front of the model the boundary layer is thin and in the absence of any separation the classical potential flow solution should provide a reasonable indication of the flow direction at the boundary layer edge. At the front of the ellipsoid flow visualisation (Figs. 7.19(a), 7.24(a), and 7.27(a)) shows the surface streamlines at a significantly different angle to that predicted by the classical potential solution. This variation in flow angle between the edge of the boundary layer and the surface is due to the pressure gradient having a greater influence on the direction of the lower inertia fluid close to the surface. This variation in flow direction must in-turn have an influence, even if only small, on the pressure. The boundary layer thickness is greater at lower Reynolds numbers so the azimuthal pressure gradient will have a larger influence on flow direction and thus the measured surface pressure at the lower Reynolds number. Panaaras and Steger [61] in their numerical solution for a 6–1 spheroid at $\alpha = 10°$, $Re_l = 7.7 \times 10^6$ note a variation in pressure gradient across the boundary layer in a similar azimuthal range ($40° \leqslant \varphi \leqslant 180°$) but further downstream at 74% of the body length.

Reduced base pressure was observed when boundary layer transition occurred near the front of the model. This reduced base pressure is associated with flow separation occurring further upstream (Fig. 5.11).

At $\alpha = -10.2°$ the flow near the symmetry plane on the suction side stays attached until at least the last on-body tapping for the model. For $\alpha = -6.2°$ flow separation occurs in the vicinity of the last on-body tap on the suction side. The ability of the flow to stay attached further downstream at $\alpha = -10.2°$ than $-6.2°$ may be due to the larger azimuthal pressure gradient seen near the base in Fig. 5.22.

An important feature of the surface pressure data measured on the spheroid and ellipsoid is that measurements are provided in the region of separated flow at the rear of the body at low to moderate incidence. These low incidence angles are important as they represent the conditions many UUVs will be operating in for a large part of the time. The ability to correctly calculate the pressure recovery in this region is important for confidence in the calculated drag.

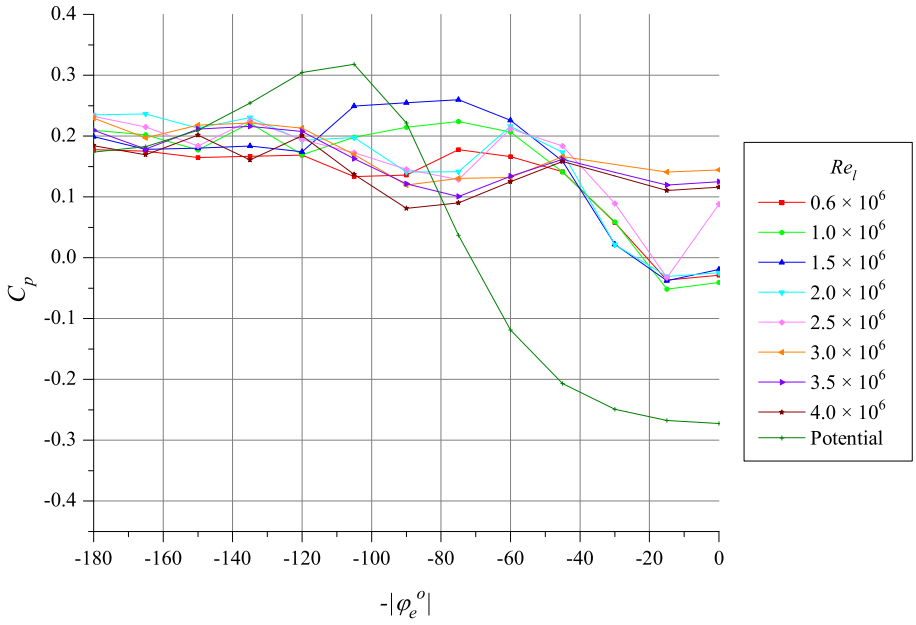

(a) $\alpha = -6.2°$, $x_{bc}/l \approx -0.44$

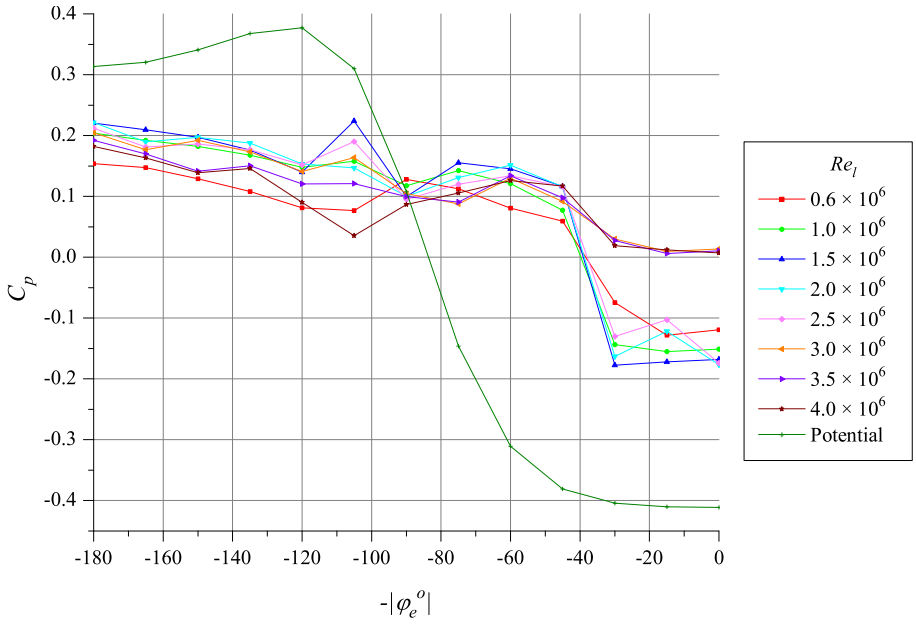

(b) $\alpha = -10.2°$, $x_{bc}/l \approx -0.44$

Figure 5.22: Surface pressure around rear of ellipsoid, Port No. 22

Chapter 6

Force and Moment Measurements

The design of a six component external balance based on load cells and flexures was being completed when this study commenced, along with a calibration frame that allows known loads to be applied parallel to the balance axes. The load is applied via a hardened cup and cone to provide precise location and direction. Calibrated masses are used to load the vertical axis; a low friction pulley is employed to redirect the force when calibrating horizontal axes. The three force components are calibrated with one component applied at a time. Calibration of the moments is performed by offsetting the load from the balance centre via a precision machined arm; thus a force and moment component is present. The calibration is performed over a full cycle of loading and unloading so hysteresis effects can be identified. The calibration results in a 6×6 matrix. Results are non-dimensionalised using the maximum cross-sectional area of the model normal to x_{bc}, $A_{x_{bc}}$, the nominal length of the model, l, and the freestream dynamic pressure q_{ref} as appropriate.

6.1 3–1 Spheroid

Force and moment measurements for the 3-1 spheroid are performed using the external balance attached to the top window. The support foil is attached to the measurement side of the balance. A shroud, designed and manufactured to fit around the support foil, mounts to the top window to minimise tare corrections. The lower section of the support foil, sting and spheroid are exposed to the flow as seen in Fig. 6.1.

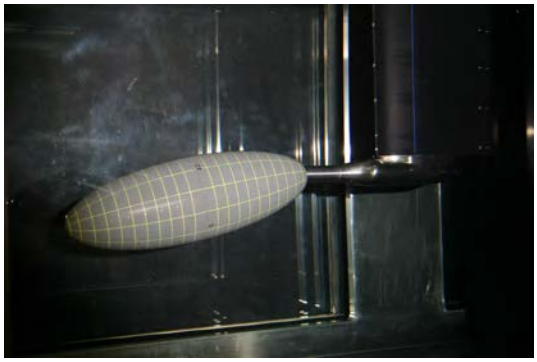

Figure 6.1: Spheroid model with shrouded support foil

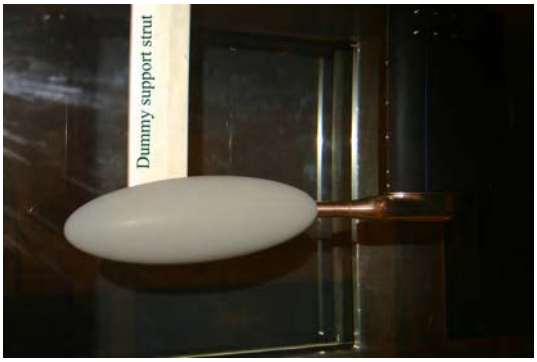

Figure 6.2: Dummy spheroid model with shrouded support foil

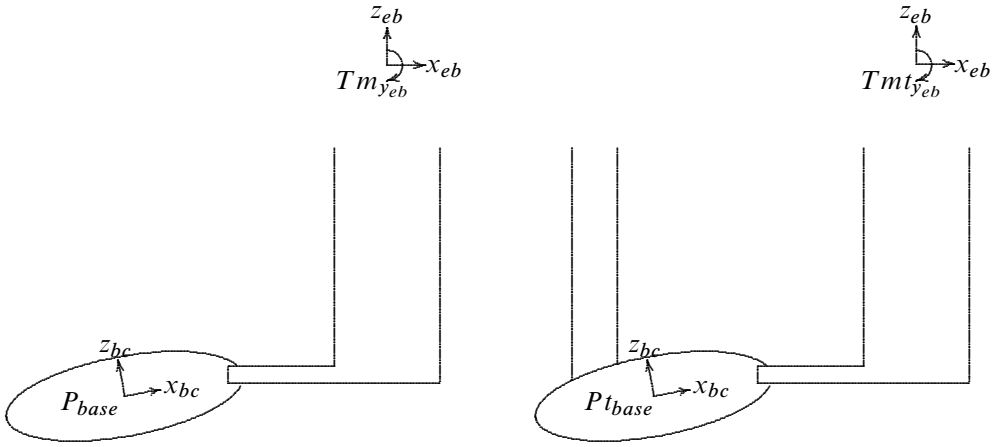

Figure 6.3: Schematic for force and moment calculations with external balance

6.1.1 Setup and Calculations for External Balance

The tare corrections are performed with a dummy model supported via a streamlined strut at the appropriate position and angle from the top window as shown in Fig. 6.2. This setup allows the wake from the streamlined dummy support strut to impinge on the shroud and thus cause minimal interference to the measurements on the sting and exposed portion of the support foil. The boundary layer on the shroud is tripped at 20% of the chord so the flow around the support foil is relatively consistent with or without the presence of the dummy support.

A small ($0.5\,mm$) gap exists between the sting and the spheroid. This gap results in a net force due to the internal pressure as the force on the internal surface that is the mirror image of the gap through the $x_{bc} = 0$ plane is not opposed. Only force and moments due to the external flow over the body are desired so the internal (base) pressure is measured and the corresponding correction applied. This correction needs to allow for the possibility that the internal pressure may not be identical between the primary and the tare correction measurements, ideally the

difference in internal pressure between these measurements should approach zero. The corrected force component on the external surfaces of the spheroid due to the flow in the x_{eb} direction is given by

$$F_{x_{eb}} = Fm_{x_{eb}} - P_{base}A_{sting_{x_{eb}}} + P_{base}A_{base_{x_{bc}}}cos(\alpha_t) - Fmt_{x_{eb}} + Pt_{base}A_{sting_{x_{eb}}} \quad (6.1)$$

where $Fm_{x_{eb}}$ is the force measured in the x_{eb} direction of the external balance during the primary measurement, $Fmt_{x_{eb}}$ is the force measured in the x_{eb} direction of the external balance during the tare correction measurement, P_{base} is internal pressure during the primary measurement, Pt_{base} is internal pressure during the tare correction measurement, $A_{sting_{x_{eb}}}$ is the cross sectional area of the sting at exit from the spheroid ($x_{bc} = 161\,mm$) normal to the x_{eb} axis, $A_{base_{x_{bc}}}$ is the area of the hole at the base of the model projected onto the plane normal to the x_{bc} axis, and α_t is the pitch angle of the model in tunnel coordinates. The first three terms of Eq. 6.1 calculate the force on the external surfaces of the ellipsoid, sting and support foil in the x_{eb} direction. The last two terms subtract the force on the external surfaces of the sting and support foil measured during the tare correction in the x_{eb} direction.

A corresponding correction for the spheroid-sting gap is required in the z_{eb} direction. An additional correction is required when calculating the lift if the static pressure differential between the top of the foil (internal static pressure of the external balance housing), and the bottom of the support foil varies between the primary and tare correction test. This pressure differential acts on the cross sectional area of the support foil normal to the z_t axis, $A_{foil_{z_{eb}}}$. An estimate of this correction was obtained by measuring the internal pressure of the balance housing, P_{eb}. This neglects the possible variation in the average pressure on the lower surface of the support foil between the primary, $\bar{P}_{lsf}$, and tare correction measurement, $\bar{P}t_{lsf}$. When the spheroid is at negative incidence a minimal difference should exist between the flow impinging on this surface for the primary and tare measurements. This is due to the model's negative incidence directing the fluid from the suction side of the spheroid onto the lower surface of the support foil, the suction side of the model being close to identical for the two cases. The lift force, $F_{z_{eb}}$, due to flow over the external surfaces of the spheroid is given by

$$\begin{aligned} F_{z_{eb}} &= Fm_{z_{eb}} + (P_{eb} - \bar{P}_{lsf})A_{foil_{z_{eb}}} + P_{base}A_{base_{x_{bc}}}cos(\alpha_t) - Fmt_{z_{eb}} + (Pt_{eb} - \bar{P}t_{lsf})A_{foil_{z_{eb}}} \\ &\approx Fm_{z_{eb}} + P_{eb}A_{foil_{z_{eb}}} + P_{base}A_{base_{x_{bc}}}cos(\alpha_t) - Fmt_{z_{eb}} + Pt_{eb}A_{foil_{z_{eb}}}. \end{aligned} \quad (6.2)$$

The pitching moment measured at the model centre, $T_{y_{bc}}$ is given by

$$T_{y_{bc}} = Tm_{y_{eb}} - Tmt_{y_{eb}} - \Delta x_{bc_{eb}}F_{z_{eb}} + \Delta z_{bc_{eb}}F_{x_{eb}} \quad (6.3)$$

where Tm_y is the moment measured about the y_{eb} direction due to flow during the primary measurement, Tmt_y is the moment measured about the y_{eb} direction due to flow during the tare correction measurement, $\Delta x_{bc_{eb}}$ is the x position of body centre in the external balance coordinates, and $\Delta z_{bc_{eb}}$ is the z position of body centre in the external balance coordinates.

6.1.2 Force and Moment Measurements

Force and moment measurements on the spheroid were for the most part unsuccessful. The support strut holding the dummy model for the tare corrections has a significant influence on the spheroid boundary layer, and thus influences the flow around the rear of the model. This influence is apparent from the internal pressure at the same incidence being different when the ellipsoid is supported from the sting or the dummy support strut. The only time this was not the case was when the boundary layer on the spheroid was transitioned using the trip strip as seen from Fig. 6.4. The forces and moment on the spheroid due to the external flow when the boundary layer is tripped are shown in Fig. 6.5. The kinks in pitching moment measurement are not present until the translation from the external balance centre to model centre. These kinks are a result of the kinks in the lift measurements.

No error analysis is presented for the external balance measurements. A discussion of the uncertainties in the results for the internal balance is presented in the next section along with a comparison between some results obtained using the internal and external balances for the 4.2-2-1 ellipsoid when a trip strip is used.

6.2 4.2–2–1 Ellipsoid Model

In order to avoid the issue of tare corrections a small six-component transducer was purchased: a Delta SI-660-60 unit manufactured by ATI Industrial Automation. A waterproof housing was designed and constructed to allow this to be fitted inside the ellipsoid model. The specifications of the transducer are shown in Table 6.1. The pancake shaped package, $28\,mm$ high and $92\,mm$ diameter (without the electrical connector), is small enough to fit inside this ellipsoid and has a suitable range.

The transducer is machined from a single piece of stainless steel. The measurement side is connected to the non-measurement side via three rectangular cross-section elements spaced 120° degrees apart. The load on the measurement side is determined from six half-bridge silicon strain gauge pairs placed on the elements between the measurement and non-measurement sides. The output from the half-bridges was measured on a 16 bit ISA-bus supplied by the manufacturer. Before digitisation the output is filtered using a low pass filter with a $-3\,dB$ point at $235\,Hz$ and

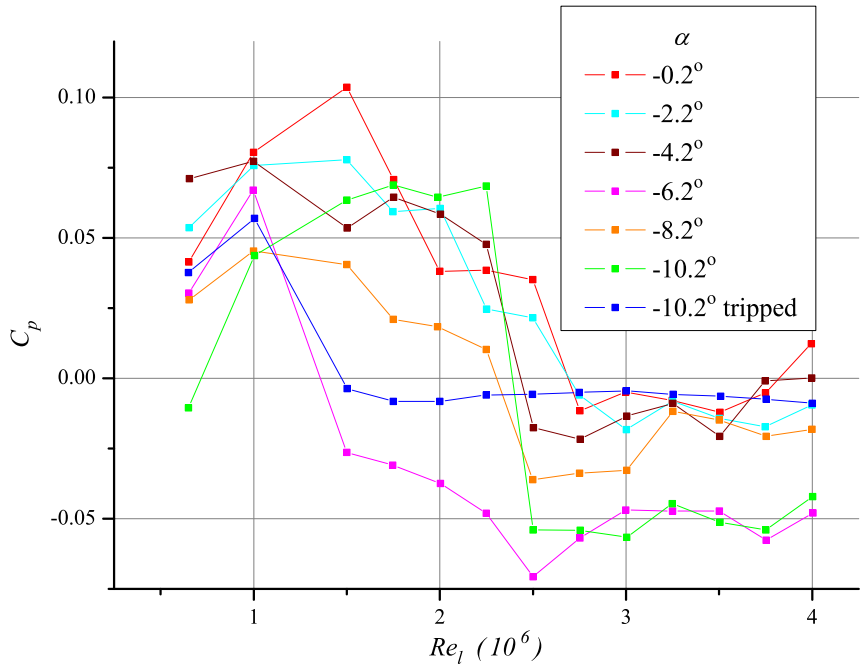

Figure 6.4: Difference in base pressure between primary and tare correction measurements

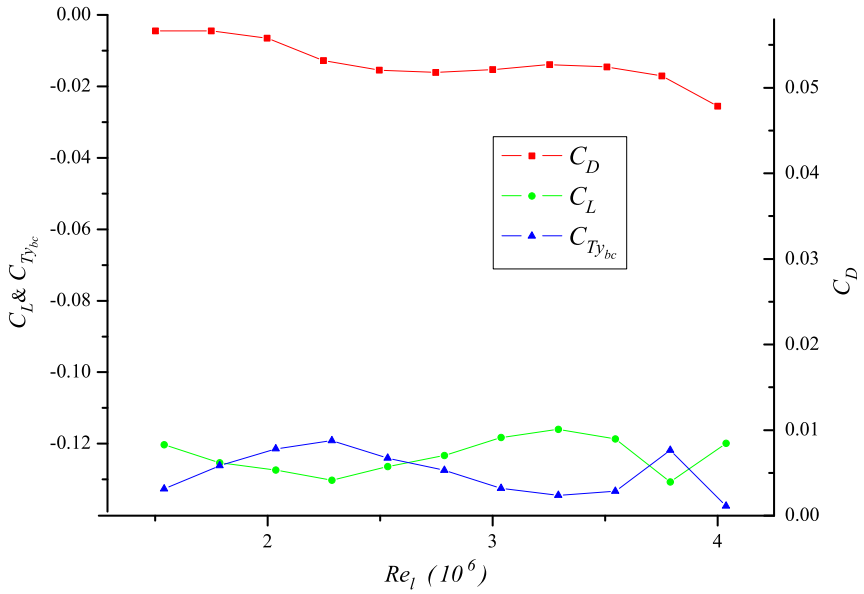

Figure 6.5: Non-dimensional forces and moment determined from external balance measurements for spheroid with trip strip located at $x/l = -0.3$, $\alpha = -10.2°$.

Component	Range	Resolution	Units
F_x	± 660	$\frac{1}{32}$	N
F_y	± 660	$\frac{1}{32}$	N
F_z	± 1980	$\frac{1}{16}$	N
T_x	± 60	$\frac{3}{1600}$	Nm
T_y	± 60	$\frac{3}{1600}$	Nm
T_z	± 60	$\frac{3}{1600}$	Nm

Table 6.1: ATI Industrial Automation Delta SI-660-60 Force/Torque transducer data.

an approximate $17\,dB$ per decade roll off. The change in sensitivity with temperature between $17°C$ – $27°C$ is stated as 0.02% per $°C$ [62].

6.2.1 Transducer Housing

The waterproof housing for the internal transducer must perform the following functions:

- prevent water damaging the transducer or influencing its operation
- allow the measurement side of the transducer to move with minimal restriction
- allow for equalisation of pressure between the inside and outside of the housing without loading the transducer
- provide electrical connection for the transducer
- provide stiff upper and lower attachment points, between which the transducer inside the housing will measure the loads.

Fig. 6.6 shows the internal housing. The circular planform transducer is fitted in a elliptical planform housing. The extra length of the housing at the end attached to the dogleg is strengthened with internal and external ribs. The external ribs are shaped to provide a precision fit to the dogleg in order to maximise stiffness and provide accurate alignment. The additional housing length at the other end is used to accommodate the transducer's electrical connector. The x axis of the transducer is rotated by 45° about its z axis so the electrical connector is aligned with the major axis of the housing. This rotation is of no consequence as the transducer is recalibrated in body coordinates once fitted to the housing.

Sealing between the housing base and upper is provided by a V-shaped diaphragm, which is permanently fixed to the housing using adhesive. Internal access to the housing without

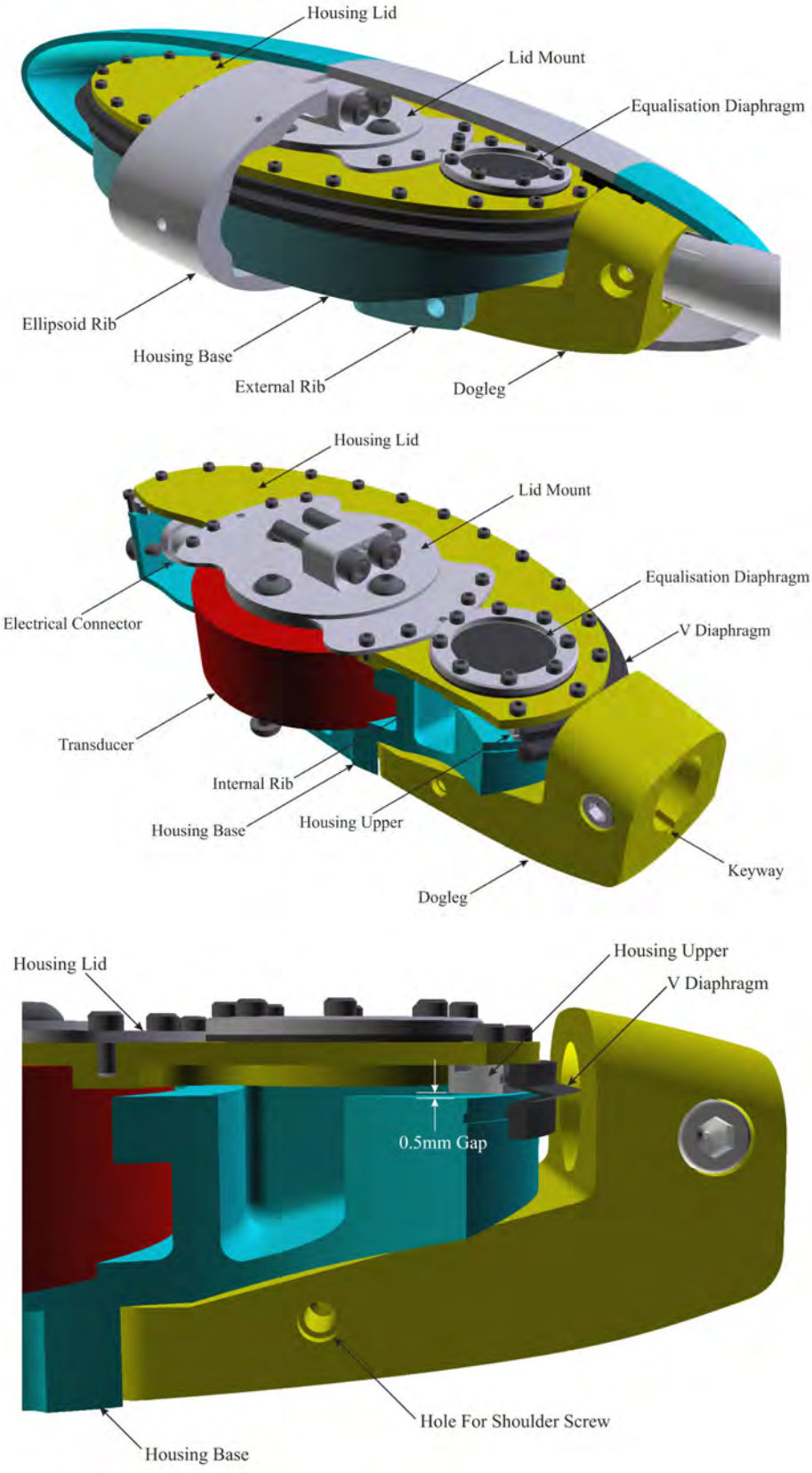

Figure 6.6: Transducer housing for internal balance

disturbing the delicate V-shaped diaphragm is provided by a housing lid which is fixed to the housing upper by numerous small screws; this is sealed using an O-ring. The connection between the transducer and ellipsoid rib is provided by the lid mount; this is bolted through the housing lid to the transducer, clamping the lid between the two. Adhesive is used to seal between the housing lid and the lid mount; washers that incorporate a rubber seal prevent leakage past the bolts connecting the lid mount and transducer. The connection between the lid mount and the rib of the ellipsoid is a precise fit on four faces to maximise the stiffness of the connection. The structural elements of the housing are fabricated from stainless steel.

The waterproof housing is filled with a non conducting, non corroding, low viscosity fluid[1], Dow Corning® 200 fluid, $10\,cSt$. The low viscosity fluid inside the housing displaces the vast majority of air inside the housing so volumetric changes due to external pressure fluctuations are minimised. Pressure equalisation is allowed for with a thin diaphragm on the top of the housing that allows for minor volumetric changes. The housing lid is manufactured from clear PVC to facilitate purging air from the housing. Pressure equalisation between the inside and outside of the housing is desirable as it:

- prevents the balance being loaded in the direction of the z axis
- allows very thin material to be used for the diaphragm between the base and the lid of the housing as they will be under minimal loads.

The thin rubber V-shaped diaphragm between the base and the top will also allow pressure equalisation, but any strain on it will have an influence on the measured force in the Z axis.

A sealed bulkhead connector suitable for underwater use was fitted to the housing to provide electrical connection and prevent flow of water or silicone oil. In the course of the setup, problems threading the mating connector through the sting resulted in the bulkhead fitting being replaced by a cable gland. This unfortunately allowed the flow of silicone oil inside the cable; this is suspected of causing pressure sensitivity in the Z axis force measurements. To minimise the influence of this sensitivity the tunnel static pressure was adjusted so the measurements were performed with a constant static pressure inside the ellipsoid, except for the results at $\alpha = -0.2°$. If no pressure compensation is used the expected pressure sensitivity, based on the area of the housing lid, is $71\ N/kPa$; the measured sensitivity after fitting the cable gland is approximately $1\ N/kPa$. Pressure compensation is clearly necessary, as without it a C_p of 0.13 at $12\,ms^{-1}$ would be sufficient to overload the transducer in the z axis.

[1]This fluid was also selected in order to have minimal effect on the coating placed over the strain gauges and on the acrylic windows in the tunnel if leakage should occur.

					Applied Load							
F_z (N)	0.0	-49.1	-98.1	-147.2	-196.2	-245.3	-245.3	-196.2	-147.2	-98.1	-49.1	0.0
T_y (Nm)	0.00	7.36	14.72	22.07	29.43	36.79	36.79	29.43	22.07	14.72	7.36	0.00
					Measured Load							
F_x (N)	0.0	0.4	0.52	0.4	0.1	-0.2	-0.3	-0.5	-0.5	-0.6	-0.6	-0.6
F_y (N)	0.0	-0.2	-0.39	-0.4	-0.2	0.1	0.1	0.1	0.2	0.2	0.2	0.1
F_z (N)	0.0	-49.0	-98.09	-147.3	-196.3	-245.0	-245.0	-196.7	-147.8	-98.7	-49.3	0.2
T_x (Nm)	0.00	0.00	-0.013	-0.02	-0.01	-0.01	-0.01	-0.04	-0.06	-0.06	-0.05	-0.03
T_y (Nm)	0.00	7.35	14.73	22.11	29.49	36.81	36.82	29.53	22.19	14.83	7.46	0.09
T_z (Nm)	0.00	0.00	0.000	0.00	0.00	0.00	-0.00	-0.01	-0.01	-0.02	-0.01	0.00

Table 6.2: Calibration of T_y component of six component transducer.

6.2.2 Calibration of Internal Six Component Transducer

The calibration frame used for the external balance is fitted with modifications to allow the transducer in the waterproof housing to be calibrated. The low friction pulley used to redirect the force was replaced with an air bearing to further minimise friction. The transducer in the housing is calibrated so the axes align with those of the model, x_{bc}, y_{bc} and z_{bc}.

All six components are calibrated. However due to model and flow symmetry about the $y_{bc} = 0$ plane the average force in the y_{bc} direction should be zero, as will the moments about the x_{bc} and z_{bc} axes. When the model is at incidence it experiences a large moment about y_{bc} and a large force in the z_{bc} direction. While subject to these loads it is important that it is able to measure small loads in the x_{bc} direction. Table 6.2 shows the measured force determined using the calibration matrix when a moment is applied to the housing/transducer assembly using a force in the z_{bc} direction at $x_{bc} = 150\,mm$. The results show minimal cross-talk to the other components.

The greatest error in the mean measurement that occurred during the calibration process for each axis is noted in Table 6.3. The larger error for the F_z and T_y components is attributed to a greater noise/drift that was observed from the time series data from one of the strain gauges used to determine these components.

	F_x	F_y	F_z	T_x	T_y	T_z
N or Nm	0.6	0.7	1.9	0.06	0.12	0.05
% of Fullscale	0.1	0.1	0.3	0.1	0.2	0.1

Table 6.3: Maximum error during calibration of six component transducer.

6.2.3 Setup and Calculations for Internal Transducer

The six component transducer within its housing is mounted to the sting via the dogleg brackets. The ellipsoid is attached to the measurement side of the transducer. Three different dogleg brackets place the housing and transducer at a incidence of either $0°$, $-6°$, or $-10°$ to the sting. The support foil, sting, and doglegs are the same as those used in previous testing. An ellipsoid of identical external dimensions and materials but with a single attachment point on the stainless steel rib was manufactured. This model has a pressure tapping at the nose and another pressure measurement was taken internally. The desired measurements are the forces and moments due to the flow over the external surface of the ellipsoid. The opening at the base of the ellipsoid, for the sting, results in the internal pressure causing a net force on the body in the x_{bc} direction. This net force for the internal balance is a result of the pressure over the entire opening, rather than only the gap between the model and the sting as was the case for the external balance, as the sting is on the non-measurement side of the balance. Measurement of the internal pressure allows the following correction to be applied:

$$F_{x_{bc}} = Fm_{x_{bc}} + A_{base_{x_{bc}}} \times P_{base} \tag{6.4}$$

The data from the transducer was sampled at 1024 Hz for 56 seconds at each Reynolds number. Measurements were taken between $Re_l = 0.70 \times 10^6$ and $Re_l = 4.0 \times 10^6$ in 0.25×10^6 increments (except for the first step of $Re_l = 0.3 \times 10^6$). The trip strip was applied to the model for one set of measurements at $\alpha = -10.2°$, the position, materials, and application where identical to that described in Subsection 4.4.4.

The first resonance peak for this system was at approximately 40 Hz, the additional mass of the balance and housing has reduced this from approximately 50 Hz. Fig. 6.7 shows the model fitted with a trip strip has less excitation between approximately 20 Hz and 40 Hz.

6.2.4 Estimate of Measurement Uncertainties

The precision of the time-averaged force and moment measurements is estimated from the standard deviation of these measurements, σ_i (Eq. 4.9). The number of samples used to calculate σ_i was adjusted to allow for the bandwidth of the transducer ($\approx 235\ Hz$).

At the lowest Reynolds number, $Re_l = 0.70 \times 10^6$, the standard deviation of the time-averaged force and moment measurements is an order of magnitude larger than when the flow has zero velocity. This suggests that the majority of the imprecision in the measurements is due to unsteady loading from the flow. Examination of the standard deviations in Fig.6.8(a)–(c) show a small kink in the curves for the ellipsoid with the trip strip at $\alpha = -10.2°$ near

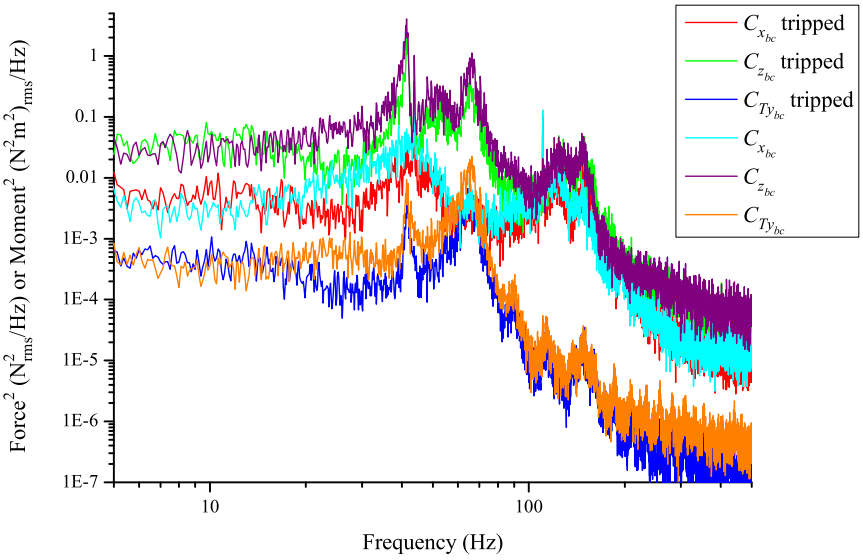

Figure 6.7: Frequency response of ellipsoid model with internal balance at $Re_l = 3.0 \times 10^6$

$Re_l = 1.25 \times 10^6$. $Re_l = 1.25 \times 10^6$ coincides with the value at which the trip strip is designed to stimulate transition of the boundary layer to a turbulent state. It is reasonable to expect that the switch from predominately laminar to turbulent boundary layer will significantly influence the loading on the body. Over the remaining range of Re_l the curves for the tripped ellipsoid are relatively smooth. The curves for the untripped cases show kinks for Re_l between 2.0×10^6 and 3.0×10^6. This occurs within the Reynolds number range where on-body flow visualisation shows a change in the type and size of separation on the model's flank (Section 7.3). The corresponding curves for σ_{C_D}/C_D in Fig. 6.8 have peaks at the Reynolds numbers where the kinks in the σ_{C_D} curve occurred.

The maximum error values determined during calibration (Table 6.3) provide an estimate of the accuracy of the force and moment measurements. The contribution to inaccuracy due to the correction for the spheroid-sting gap has not been taken into account as the associated inaccuracy is small compared to that of the transducer.

The imprecision of the internal balance measurements as determined from the standard error is significantly smaller than their inaccuracy. Uncertainty in the measured mean force or moment at the lowest Reynolds numbers is dominated by two orders of magnitude by this inaccuracy. At the highest Reynolds numbers the inaccuracy is still dominated by a factor of five for the lift and drag and a factor of two for the pitching moment (T_{ybc}). The author believes that this analysis overestimates the error at low Reynolds numbers and underestimates it at high Reynolds numbers and that the errors are less than 25% of the measured value at the lowest Reynolds numbers decreasing towards 5% at the largest Reynolds numbers. The error bars in Fig. 6.9 are determined from the estimate of inaccuracy.

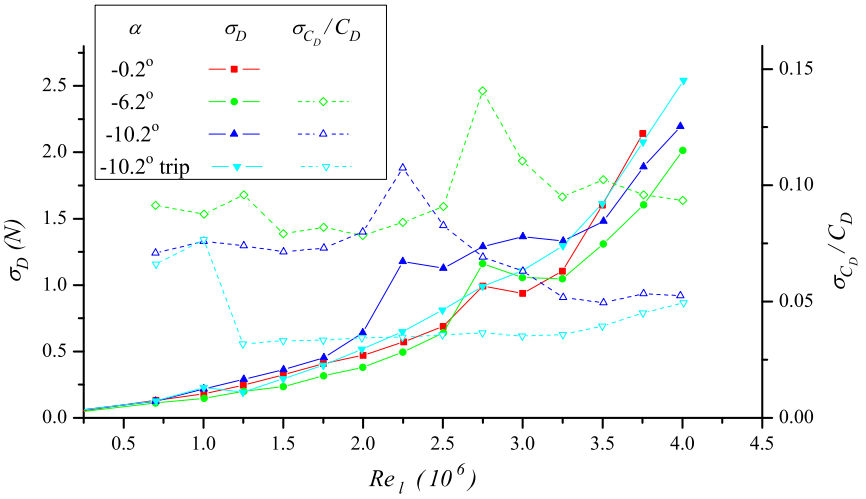

(a) Drag

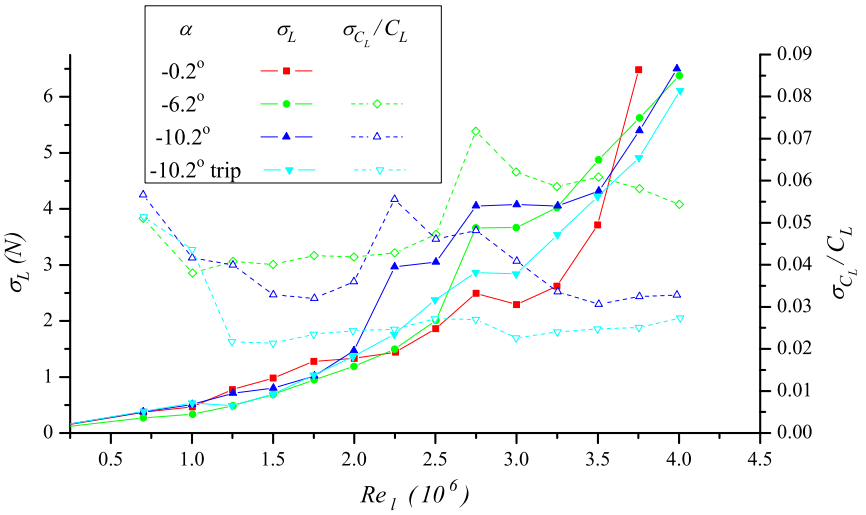

(b) Lift

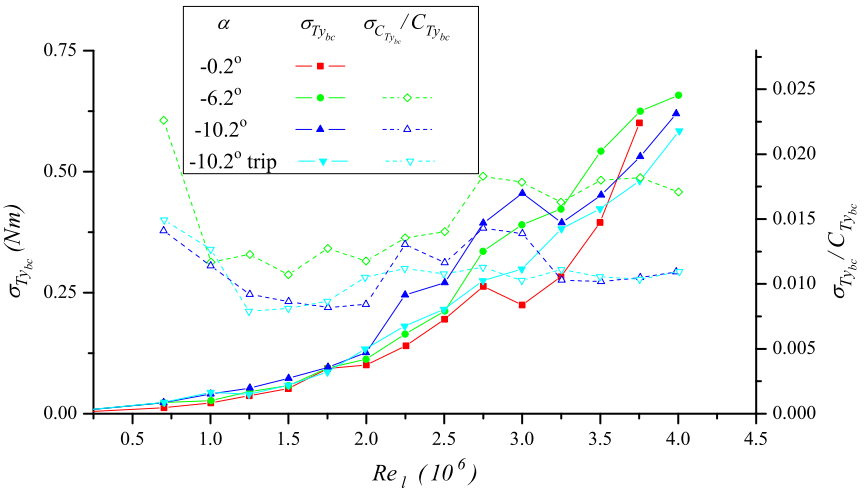

(c) $T_{y_{bc}}$

Figure 6.8: Standard deviation of force and moment readings on 4.2-2-1 ellipsoid.

The housing was designed to compensate for pressure changes. However as noted in Subsection 6.2.1 a modification during setup is suspected of rendering this aspect of the housing less effective. The size of the correction is minimised by adjusting the tunnel static pressure so the internal pressure of the model is constant. The magnitude of the correction using this technique varied from 5% to 0.1% of the measured reading at the lowest and highest Reynolds numbers respectively. Thus the uncertainty in this correction is small compared to the already existing uncertainties. The exception to this occurred at $\alpha = -0.2°$ were the technique of setting the tunnel static pressure to minimise the correction was not used. The results for the $F_{z_{bc}}$ for this incidence are discarded and the minimal contribution to the drag ignored. The other undesirable aspect of failing to use this technique to minimise the correction is that crosstalk between the z_{bc} and x_{bc} axes that otherwise could be avoided is present for this measurement.

6.2.5 Force and Moment Measurements

Measurements with unforced transition were performed for $\alpha = -0.2°$, $-6.2°$, and $-10.2°$. A second set of measurements was conducted at $\alpha = -10.2°$ with a trip strip placed at $x_{bc}/l = -0.3$.

The force and moment measurements are shown in Figs. 6.9 and 6.10. The drag coefficient, C_D, shows a gradual decrease as Re_l increases from 0.7×10^6 to 2.0×10^6 for the cases with unforced transition. For $\alpha = -0.2°$ and $-6.2°$ C_D remains fairly constant between $Re_l = 2.0 \times 10^6$ and 3.5×10^6 before increasing as Re_l approaches 4.0×10^6. For $\alpha = -10.2°$ with unforced transition a gradual increase in C_D is observed between $Re_l = 2.0 \times 10^6$ and 2.75×10^6; it then levels out until after $Re_l = 3.5 \times 10^6$ when it gradual increases. The measured C_D at $\alpha = -0.2°$ appears to have a low value, this is discussed in Subsection 10.5.

The measured drag for the model with the trip strip is approximately 10% greater than that of the clean model when the trip strip is not expected to be effective. Immediately after the Reynolds number where the trip strip is designed to be effective, $Re_l = 1.25 \times 10^6$, C_D increases suddenly. After this it shows a steady decrease as Re_l approaches 4.0×10^6, this decrease in drag is due to a reduction in the component from $F_{x_{bc}}$. A repeat of this test resulted in essentially identical results. The surface pressure curves for the corresponding case appear to be independent of Reynolds number, except for a small region upstream of the trip strip and another in the region of separated flow near $x_{bc}/l = 0.38$, $\varphi_e = 105°$. The following reasons are not considered to explain the decrease in $F_{x_{bc}}$ from 0.031 to 0.016 as the Reynolds number increases from 1.5×10^6 to 4.0×10^6:

- the slight decrease in surface pressure seen with increasing Reynolds number in the separated region (on the back half of the body) will increase $F_{x_{bc}}$

- the elements of the trip strip are likely to increase $F_{x_{bc}}$ as their height becomes a greater proportion of the boundary layer height
- the viscous drag coefficient on a flat plate decreases with increasing Reynolds number. However this expected decrease for a flat plate is of the order of 20% over this Reynolds number range and is unlikely to account for the observed reduction in $F_{x_{bc}}$.

This leaves the slight change in surface pressure over the front 20% of the body as a possible (but unlikely) explanation for this trend (as discussed later, the integration of the surface pressure is not considered an accurate method of determining the form drag given the relatively coarse pressure tapping spacing). The spheroid with the trip strip at $\alpha = -10.2°$ showed a decline in C_D of approximately half that seen here over the same Reynolds number range. The difference between C_D values at $\alpha = -10.2°$ with the forced and unforced transition decreases as Re_l approaches 4.0×10^6.

The lift and pitching moment coefficient comprise a component due to the angle of incidence and another due to the blockage caused by the support foil. The support foil is in a position $(+Z)$ such that the increased upstream pressure it induces creates a lift force in the same direction as caused by a negative angle of incidence. The increase in pressure upstream induced by the support foil decreases with distance upstream. This streamwise pressure distribution creates a pitching moment in the same direction as caused by a positive angle of incidence. The lift and moment due to the foil will be present for all incidences, but is more noticeable at low incidences. It will result in non-zero crossings for the lift and moment versus incidence curves at $\alpha = 0°$.

The lift measurements at $\alpha = -0.2°$ were discarded as earlier mentioned. At $\alpha = -6.2°$ a steep initial decrease in the magnitude of C_L for Re_l less than 1.25×10^6 moderates to a very slight decrease as Re_l approaches 3.5×10^6 before increasing again. The magnitude of C_L for $\alpha = -10.2°$ decreases for Re_l between 0.7×10^6 to 1.75×10^6 and gradually increases after this with a small kink at 2.75×10^6. The lift and drag curves at $\alpha = -6.2°$ and $-10.2°$ have similar shapes as a result of the lift-induced drag.

For $\alpha = -10.2°$ with trip strip applied C_L is close to constant for Re_l between 1.25×10^6 and 4.0×10^6. At $Re_l = 0.7 \times 10^6$ and 1.0×10^6 the C_L values are 16% and 5% larger respectively than for the similar cases without the trip strip. C_L remains smaller for the case with unforced boundary layer transition, but approaches the value of the forced boundary layer transition case as Re_l approaches 4.0×10^6.

The pitching moment coefficient at $\alpha = -0.2°$ is close to constant for the range of Reynolds numbers measured. At $\alpha = -6.2°$ the magnitude of the pitching moment coefficient increases between $Re_l = 0.7 \times 10^6$ and 1.25×10^6 and remains constant for the remainder of the range.

For $\alpha = -10.2°$ the moment magnitude increases between $Re_l = 0.7 \times 10^6$ and 1.75×10^6; it then gradually decreases as Re_l approaches 4.0×10^6, flattening more at the higher end of the range. The moment magnitude at $\alpha = -10.2°$ with the trip strip matches the values of the corresponding case without the trip strip for Reynolds numbers before the trip is effective. Once the trip is effective the moment magnitude drops to a constant value through to $Re_l = 2.5 \times 10^6$. After this the magnitude gradually increases towards the value shown for the case with unforced transition.

Comparison of the lift and pitching moment results for the tripped and untripped cases, once the trip is effective, shows that there must be a significant shift in the centre of pressure between the two cases. The lift magnitude is greater for the case with the trip strip but the magnitude of the pitching moment less.

For the observations at low Reynolds numbers in this subsection the trends described are less than the maximum inaccuracy. Hence confirmation of these trends requires further supporting evidence.

The force and moment on the body may be broken down into two components: one due to static pressure at the surface, which creates a force normal to the surface; and one due to shear stress, which creates a force tangential to the surface. As surface pressure measurements are available, consideration is given to integrating them over the surface in order to estimate the force and moments due to the surface pressure. If the surface pressure curve of the spheroid or ellipsoid at $\alpha = 0°$ is examined its influence on the form drag may be divided into four segments:

- over the front ($\approx 10\%$) of the model C_p is positive, and the normal to the surface has a significant component opposite to the direction of the freestream flow. This section of the body results in a positive contribution to the form drag.

- over the remaining front half of the model where C_p is negative, the normal to the surface gradually rotates from having a significant component opposite to that of the freestream flow to being perpendicular to it. This results in a negative contribution to the form drag.

- from $x_{bc} = 0.5$ to where C_p is no longer negative (≈ 0.85), the normal to the surface rotates from being perpendicular to the freestream flow to having a significant component in its direction. This results in a positive contribution to the form drag.

- the remainder of the body where C_p positive, and the surface normal is predominantly in the direction of the freestream flow. This section of the body results in a decrease in form drag. Flow separation over this region of results in a reduced pressure recovery and thus a greater drag.

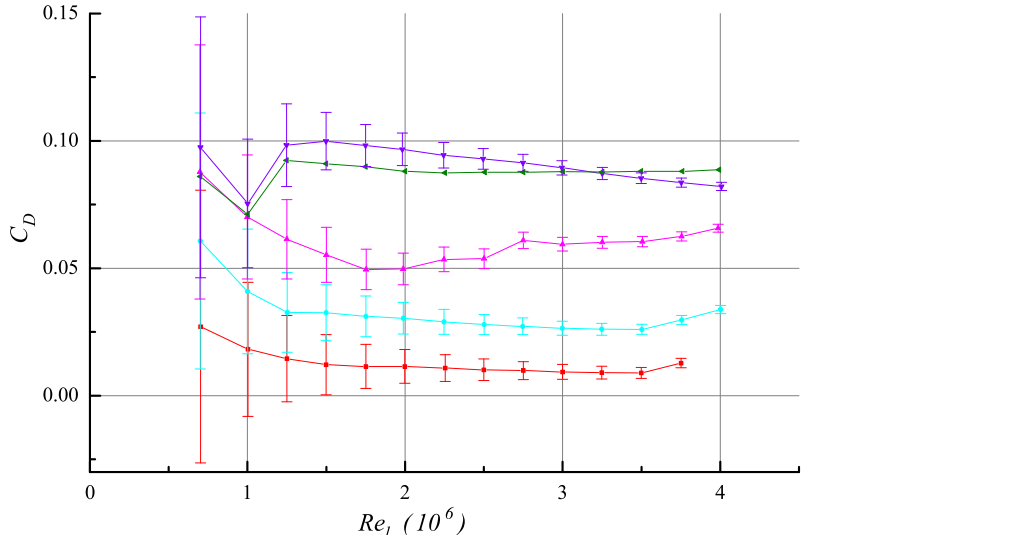

(a) Drag

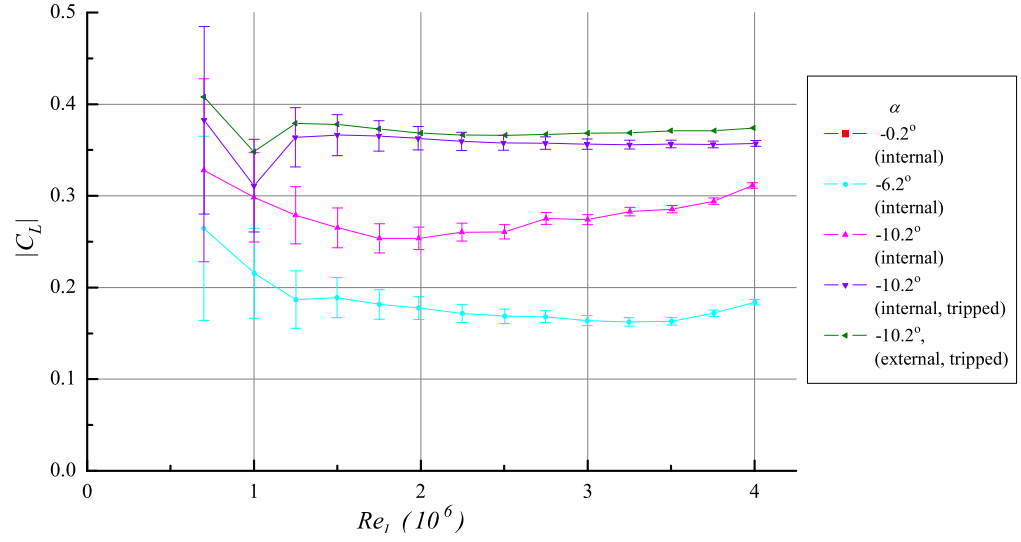

(b) Lift

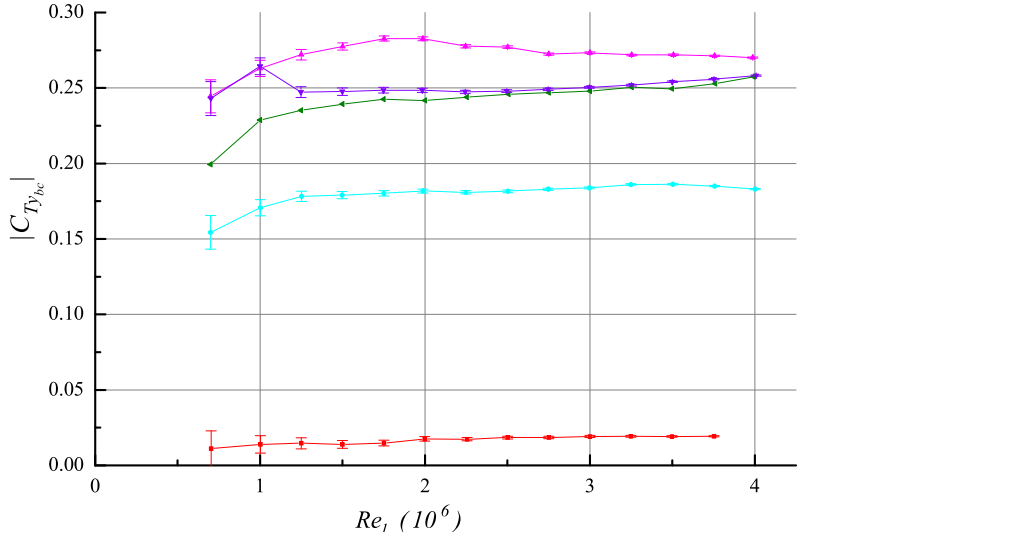

(c) Pitching moment

Figure 6.9: Force and moment measurements against Reynolds number for the 4.2-2-1 ellipsoid.

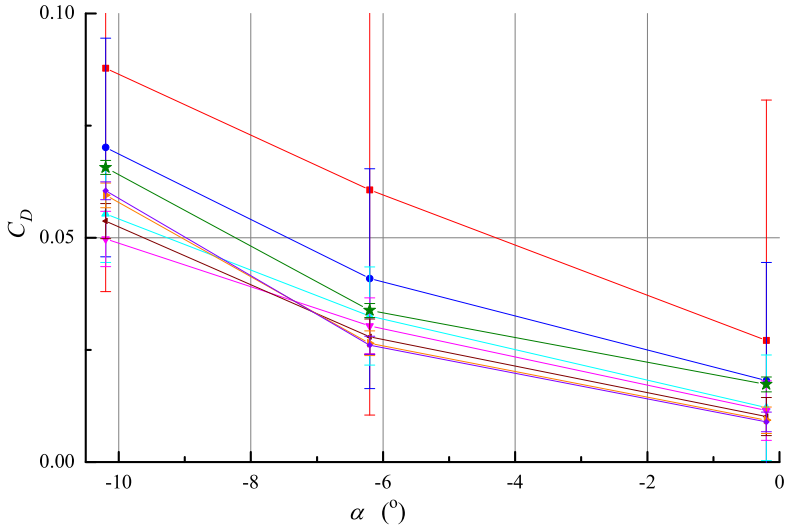

(a) Drag

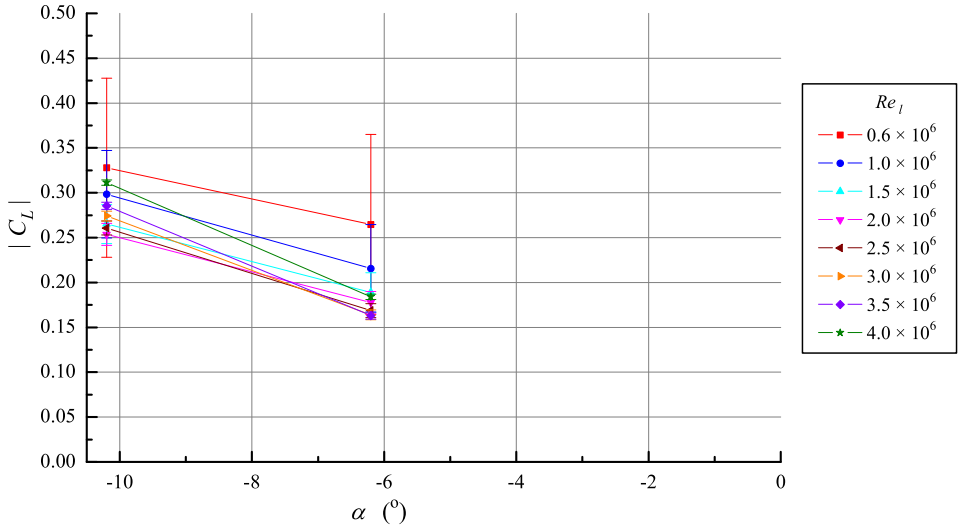

(b) Lift

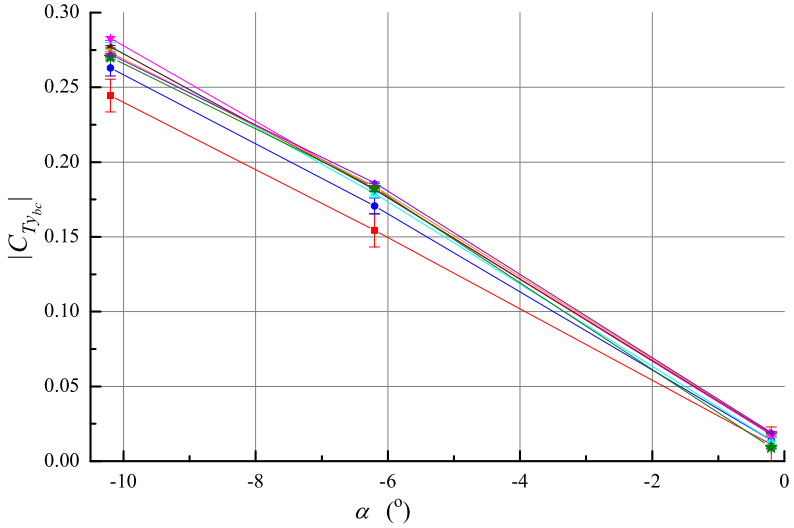

(c) Pitching moment

Figure 6.10: Force and moment measurements against incidence for the 4.2-2-1 ellipsoid.

The high rate of change in surface pressure at the front and rear where the largest contribution to form drag occurs, combined with relatively low number of measurement points in this region, suggest any attempt to estimate form drag from the measured surface pressure distribution will be unsuccessful. A similar process can be applied to estimating force in the z_{bc} direction due to surface static pressure. For this direction there are a relatively large number of tappings over the surface regions that generate the majority of force in this direction. The rate of change in static pressure over surfaces where the surface normal is predominantly parallel to the z_{bc} direction tends to be much less than is the case at the front and rear of the model. As CFD results later show, the surface shear stress plays a minimal direct role in the net force in the z_{bc} direction. Thus if suitable resolution of tappings is available the integration of pressure should provide a reasonable estimate of $F_{z_{bc}}$ (and the lift).

Applying these considerations to calculation of the pitching moment, $T_{z_{bc}}$, results in the following observations: if $F_{x_{bc}}$ has a significant role in the pitching moment the estimate will be inaccurate, the calculations of $F_{z_{bc}}$ at the front and rear of the model where the rate of change in the surface pressure is greatest will have a large influence on the estimate as the moment arm is longest in these regions. These observations indicate that the estimate of the pitching moment from the surface pressure will be less accurate than for $F_{z_{bc}}$. Fig. 6.11 provides a comparison of the force coefficient $C_{Fz_{bc}}$ and the contribution of this force to $C_{Ty_{bc}}$ to that measured by the internal transducer. This figure shows that the estimates calculated from the pressure for these components display many of the trends seen in the measurements obtained from the transducer.

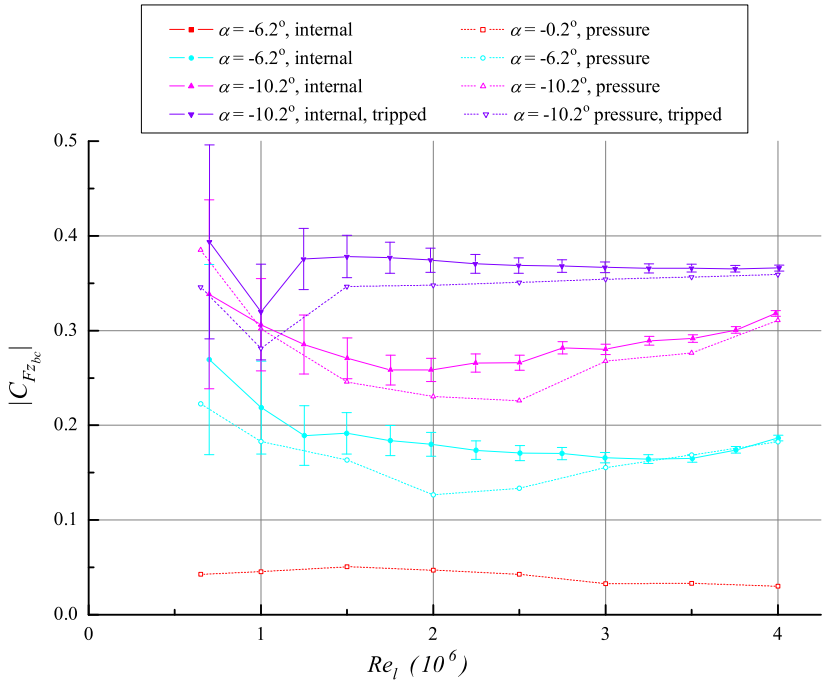

(a) Body normal force coefficient

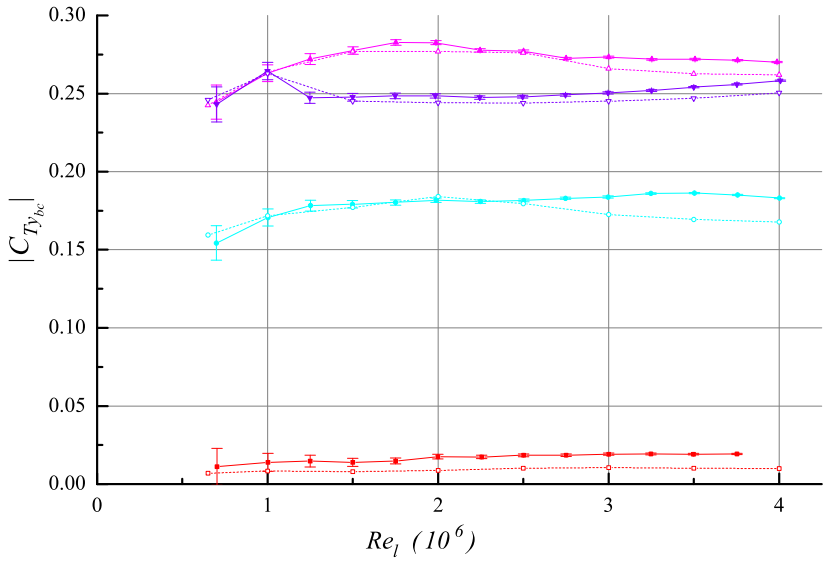

(b) Pitching Moment Coefficient, $C_{Ty_{bc}}$ - solid line; component of $C_{Ty_{bc}}$ due to pressure estimate of $C_{Fz_{bc}}$ - dotted line

Figure 6.11: Comparison of force and moment estimates from surface pressure with measured force and moment for 4.2-2-1 ellipsoid.